International Scientific-Technical and Production Journal

The Paton WELDING JOURNAL

July 2005 # 7

English translation of the monthly «Avtomaticheskaya Svarka» (Automatic Welding) journal published in Russian since 1948

Founders: *E.O. Paton Electric Welding Institute of the NAS of Ukraine*
International Association «Welding»

Publisher: *International Association «Welding»*

Address:
E.O. Paton Electric Welding Institute,
International Association «Welding»,
11, Bozhenko str., 03680, Kyiv, Ukraine
Tel.: (38044) 287 67 57
Fax: (38044) 528 04 86
E-mail: journal@paton.kiev.ua
http://www.nas.gov.ua/pwj

State Registration Certificate
KV 4790 of 09.01.2001

Subscriptions:
$324, 12 issues per year,
postage and packaging included.
Back issues available.

CONTENTS

CONTRACTION OF THE TUNGSTEN CATHODE WELDING ARC IN INERT GAS MIXTURES

P.V. PORITSKY, V.P. PRILUTSKY and V.N. ZAMKOV
E.O. Paton Electric Welding Institute, NASU, Kiev, Ukraine

Effect of physical characteristics of mixtures of inert gases on contraction of the positive arc column was studied. It is shown that variation in the concentration of mixture components has a substantial impact on their thermal-physical properties and general characteristics of electron-atom collisions, which determine electrophysical parameters of the arc under its specific burning conditions. In this connection, contraction of the welding arc burning at tungsten cathode in inert gas mixtures greatly depends upon the proportion of the mixture components. Contraction of the arc discharge in a specific gas mixture was found to be most significant with a gas thermal conductivity dominating in the heat removal process.

Keywords: *TIG welding, Ramsauer effect, welding arc, tungsten cathode, inert gas mixture, thermal contraction, gas thermal conductivity*

The efficiency of TIG welding depends upon the depth of penetration of base metal, other conditions being equal, and is directly related to the concentration of energy (current density) in the arc. Several methods are used in TIG welding to increase the concentration of energy in the arc column, one of them being the use of a mixture of inert gases. For example, immersed-arc welding is performed, as a rule, in a mixture of argon and helium, which provides the defect-free welds with an increased penetration depth.

The purpose of this study was to investigate the effect of physical characteristics of inert gas mixtures on contraction of the positive arc column.

Arc discharges are characterised by a contraction phenomenon occurring with decrease in a region occupied by the discharge plasma. Studies [1, 2] consider different mechanisms of contraction of the arc in inert gases. However, the results of these studies are inapplicable to a case of utilisation of inert gas mixtures, as properties of the gas mixtures and multi-component discharge plasma in such mixtures are non-additive to properties of individual components [3–6]. The welding arc is characterised by thermal contraction, the formation of which is caused by the processes of heat transfer [7, 8]. Below we will analyse processes that lead to thermal contraction, assuming that electron and gas temperatures, T_e and T, respectively, are different in the arc column plasma.

Two-temperature thermal-plasma. Study of characteristics of the arc discharge is based on the equation of heat transfer (Elenbaas–Heller equation [7–9]). Solution of this equation depends upon the values of the transfer coefficients (transport coefficients), which are the functions of temperature and concentration of charged particles in the arc plasma. In turn, the concentration of the charged particles in plasma depends upon the temperature, the type of this dependence being substantially different for different plasma states. Consider first the state of the arc discharge plasma.

As stated in [2], local thermodynamic and ionisation equilibrium characterised by specific gas and electron temperatures, T and T_e, respectively, takes place in the welding arc plasma consisting of an inert gas. For a case of DC welding, the relationship between them can be written down in the following form [8–10]:

$$T_e - T = \left(\frac{E}{n_a}\right)^2 g(T_e), \qquad (1)$$

where $g(T_e) = \frac{m_a}{3k}\left(\frac{e}{m_e}\right)^2 \frac{\langle u^2/k_{ea}\rangle}{\langle u^2 k_{ea}\rangle}$; m_a and m_e are the masses of atom and electron, respectively; u is the electron velocity; $k_{ea} = v/n_a = u\sigma^*_{ed}(u)$ is the constant of the electron-atom collision velocity; n_a is the atom density; and σ^*_{ea} is the transport (diffusion) cross-section of the electron-atom collisions. Function $g(T_e)$ is a universal characteristic of difference of the electron temperature from the gas one, and for a given gas type it depends neither upon electric field intensity E nor upon atom density n_a.

The criterion of applicability of formula (1), which also meets the possibility of adding the T_e and T temperatures to describe the low-temperature plasma, has the following form [10, 11]:

$$n_e\sigma_{ee} > \frac{m_e}{m_a} n_a\sigma_{ea}, \qquad (2)$$

where n_e is the density of electrons; and σ_{ee} and σ_{ea} are the characteristic cross-sections of electron–electron and electron–atom collisions, respectively.

As it holds usually for the arc discharge plasma that $\sigma_{ee} >> \sigma_{ea}$, this criterion can be violated only in the case of a low degree of ionisation of gas. The density of electrons, as a rule, is an exponential function of the electron temperature. Therefore, violation of criterion (2) takes place at low (for the arc plasma conditions) values of T_e.

Consider the state of gas at low ionisation, when

$$kT_e \ll E_I, \quad (3)$$

where E_I is the effective energy of ionisation of gas environment.

If this environment is a mixture of gases, E_I can be calculated using the energy of ionisation of the mixture components:

$$E_I = -kT_e \ln\left[\frac{1}{(g_i/g_a)_{eff}} \sum_j x_j \frac{g_{ij}}{g_{aj}} \exp\left(-\frac{E_{I,j}}{kT_e}\right)\right],$$

where g_i and g_a are the statistical weights of the main states of ion and atom, respectively; $(g_i/g_a)_{eff} = \sum_j (g_{ij}/g_{aj})x_j$ is the effective relationship of the statistical weights; $E_{I,j}$ is the energy of ionisation of a component; x_j is the molar fraction of the component; and index j shows an attribute of the j-th component of the mixture. With this definition of E_I, in a case of an extremely low content of additional components the values of this parameter coincide with the energy of ionisation of a single-component gas.

Proceeding from condition (3), note that the density of excited atoms in plasma is low, compared with their density in the basic state.

Expression (1) can also be used with some alterations to calculate the gas-mixture thermal plasma. Thus, generalisation of spherical harmonics for the kinetic Boltzmann equation in the case of gas mixtures yields that the difference of the electron temperature can be calculated as follows:

$$T_e - T = \frac{\mu_a}{3k}\left(\frac{eE}{m_e}\right)^2 \frac{\langle u^2/\nu_{ea}\rangle}{\langle u^2\nu^*_{ea}\rangle}, \quad (4)$$

where μ_a is the effective mass of a mixture atom; ν_{ea} and ν^*_{ea} are the total and effective frequencies of collisions of electrons with atoms of the mixture, respectively, which can be determined as follows:

$$\frac{1}{\mu_a} = \sum_j \frac{x_j}{m_{aj}}; \quad \nu_{ea} = \sum_j \nu_{ea,j}; \quad \nu^*_{ea} = \sum_j \frac{m_{aj}}{\mu_a}\nu_{ea,j},$$

where m_{aj} is the mass of atom in a mixture component; and $\nu_{ea,j}$ is the frequency of collisions with atoms of a given component.

As ionisation frequency $\alpha = n_e/N$ (where N is the density of heavy particles) grows to $1\cdot10^{-4}$–$1\cdot10^{-3}$, collisions of electrons with ions become significant. To allow for the Coulomb collisions in a slightly ionised plasma, it is necessary to replace the electron–atom collision frequency in the used formulae by the total frequency of electron-heavy particle collisions, $\nu_e = n_{ea} + \nu_{ei}$; $\nu^*_e = \nu^*_{ea} + \nu^*_{ei}$, where ν_{ei} and ν^*_{ei} are the total and effective frequencies of electron–ion collisions, respectively, which are expressed in terms of the transport cross-section of the Coulomb collisions [2] and determined in a way similar to the above frequency of electron–atom collisions.

In addition, increase in the concentration of the charged particles intensifies the effects caused by non-ideality of the low-temperature plasma, and decrease in the plasma pressure and energy of ionisation of atom in the plasma in particular. The said effects are allowed for using the most common method of the Debye correction or «Griem correction» [12]:

$$\Delta p = \frac{n_e e^2}{12\pi\varepsilon_0 r_D}; \quad \Delta E_I = \frac{e^2}{4\pi\varepsilon_0 r_D},$$

where Δ_p is the decrease in pressure; e is the electron charge; ε_0 is the dielectric coefficient of vacuum; r_D is the Debye radius; and ΔE_I is the decrease in the energy of ionisation of the gas environment.

Relationship between the electron and gas temperature, as well as values of the concentration of the charged particles being known, it is possible to calculate transport coefficients in the arc discharge plasma in a mixture of inert gases.

Transport coefficients of gas-mixture thermal plasma. The state-of-the-art in the theory of gas mixtures, as well as a multi-component plasma, is characterised by the absence of a unified approach to description of the transfer processes. The cause is a very complicated character of the dependence of properties of gas mixtures and plasma upon the properties of pure gases and the concentration of components. Detailed analysis of modern theoretical notions in this field is given in [3–6].

To calculate transport coefficients, the authors of the present study used the methods recommended in [4, 5], which are suitable for mixtures of inert gases and a multi-component arc plasma.

Thermal conductivity of gases is known to be almost independent of pressure (except for the case of low pressure), and the coefficient of thermal conductivity of inert gases can be approximately described using the formula of study [13]:

$$\kappa = \kappa_{273}(T/T_{273})^\gamma,$$

where $T_{273} = 273.16$ K; $\kappa_{273} = \kappa(T_{273})$; $0.70 < \gamma < 0.95$.

Thermal conductivity of gas mixtures features non-additivity of this characteristic to thermal conductivity of each component of a mixture. Gas thermal conductivity of a mixture of two inert gases was calculated using the known Vasilieva's formula [3, 4]:

$$\kappa = \frac{\kappa_1}{1 + A_{12}\dfrac{x_2}{x_1}} + \frac{\kappa_2}{1 + A_{21}\dfrac{x_1}{x_2}},$$

where coefficients A_{lj} ($l, j = \{1, 2\}$; $l \neq j$) were calculated according to the approximate Mason–Saxen method [3, 4]:

$$A_{lj} = \frac{0.85}{2\sqrt{2}}\left(1 + \frac{m_{al}}{m_{aj}}\right)^{-1}\left(1 + \left(\frac{k_l}{k_j}\right)^{1/2}\left(\frac{m_{al}}{m_{aj}}\right)^{1/4}\right)^2,$$

where k_l and k_j are the coefficients of thermal conductivity of individual components; m_{al} and m_{aj} are the masses of atoms; and indices l and j stand for the type of particles in a gas mixture.

The coefficient of thermal conductivity in a case of the ionisation–recombination processes, κ_{rec}, according to [10], was determined as follows:

$$\kappa_{rec} = \frac{D_{amb}\, n_e}{2}\left(\frac{E_I}{kT_e}\right)^2,$$

where D_{amb} is the coefficient of ambipolar diffusion.

This value may substantially contribute to the total thermal conductivity due to a high value of $(E_I/kT_e)^2$.

The coefficient of ambipolar diffusion can be expressed in terms of the coefficient of diffusion of ions, D_{ion}, according to [8, 10]:

$$D_{amb} = D_{ion}\left(1 + \frac{T_e}{T}\right). \quad (5)$$

The coefficient of diffusion of ions can be calculated as follows [8, 14]:

$$D_{ion}N = d_{i0}\sqrt{T/T_{i0}}, \quad (6)$$

where d_{i0} is the constant for a given type of ion and buffer gas at $T_{i0} = 1000$ K.

The calculations were made using the data on diffusion of ions taken from studies [14, 15]. It should be noted that in diffusion of ion in a gas the diffusion coefficient is determined mostly by the process of resonance recharging.

In the case of a gas mixture, the coefficient of ambipolar diffusion is determined as follows [5], instead of (5):

$$D_{amb} = \sum_i \frac{n_i}{n_e} D_i\left(1 + \frac{T_e}{T}\right),$$

where the sum is taken for all kinds of ions; D_i is the coefficient of diffusion of the i-th kind in a given mixture, which can be calculated as follows:

$$D_i = 1\Big/\left(\sum_l \frac{x_l}{D_{il}}\right),$$

where x_l is the molar fraction of the l-th component of the mixture; D_{il} is the coefficient of mutual diffusion of ion in the l-th component of the mixture determined from (6).

Electrical conductivity of plasma and electronic thermal conductivity are found from the following expressions [5, 16]:

$$\sigma = \frac{n_e e^2 \langle u^2\rangle}{m_e \langle u^2 \nu_{ea}\rangle}; \quad k_e = \frac{5}{2}\frac{n_e k^2 T_e \langle u^2\rangle}{m_e \langle u^2 \nu_{ea}\rangle}.$$

As noted above, with increase in the degree of ionisation it is necessary to select frequency ν_e determined from the total cross-section of collisions of electrons with heavy particles, instead of collision frequency ν_{ea}. The transport cross-sections were selected from the tabulated data [17] to calculate the arc discharge parameters.

According to the above dependencies, thermal conductivity of thermal plasma in the two-temperature model is characterised by several coefficients reflecting different thermal conductivity mechanisms. On the one hand, these coefficients depend upon the electron or gas temperature. And on the other hand, the interrelationship exists between the electron and gas temperatures, which is determined from expression (4). So, the transport coefficients required to solve the equation of heat transfer, as well as the relationship between the ion and gas temperatures were thus found.

Arc discharge model. Consider plasma of the positive column of the welding arc, providing that it has a cylindrical shape and is characterised by local thermodynamic and ionisation equilibrium, as well as by a constant pressure across the section of the discharge. Assuming that the intensity of heat release is proportional to the local current density, write down the equation of heat transfer in the following form:

$$\frac{1}{r}\frac{d}{dr}\left\{r\left[\kappa(T)\frac{dT}{dr} + (\kappa_e(T_e) + \kappa_{rec}(T_e))\frac{dT_e}{dr}\right]\right\} + q(r) = 0, \quad (7)$$

where r is the distance from the discharge axis; $\kappa(T)$, $\kappa_e(T_e)$ and $\kappa_{rec}(T_e)$ are the coefficients of gas and electronic thermal conductivity, and thermal conductivity caused by the ionisation–recombination process, respectively; $q(r) = j(r)E$ is the intensity of heat release per unit volume; and $j(r) = \sigma E$ is the electric current density.

Equation (7) describes the heat transfer across the section of the discharge allowing for the gas and electronic thermal conductivity. Determine the temperature field in the arc plasma from this equation. Like in study [2], we select the following boundary conditions: temperature at the arc centre is $T(0) = T_0$; and temperature of the discharge chamber wall, T_R, is assumed (without any loss of generality of the consideration) to be equal to a specific constant value (e.g. 300 K).

Following the procedure described in study [2], we use the following system of algebraic equations to calculate parameters of the arc discharge:

$$T_e - T_0 = \left(\frac{E}{N}\right)^2 g(T_e); \quad (8a)$$

$$IE = \frac{\pi k T_e^2}{E_I}\left[16k\zeta_T\left(\frac{1}{1 + (r_g/R)^2}\right) + 5(k_e + k_p)\right]; \quad (8b)$$

$$S = 0.215 q_0 r_0^2 \ln(R/r_0); \quad (8c)$$

$$p + \Delta p = NkT_0 + n_e k T_e; \quad (8d)$$

$$\frac{n_e^2}{n_a} = \frac{2g_i}{g_a}\left(\frac{2\pi m_e k T_e}{h^2}\right)^{3/2}\exp\left(-\frac{E_I}{kT_e}\right); \quad (8e)$$

$$I = \sigma E \pi r_0^2. \quad (8f)$$

Here I is the arc current; R is the radius of the discharge chamber wall; S is the thermal function; $q_0 = \sigma E^2$; $\zeta_T = \frac{dT_0}{dT_e} = \left(1 - (T_e - T_0)\frac{d\ln g(T_e)}{dT_e}\right)\left(\frac{2T_e}{T_0} - 1\right)^{-1}$; r_0

is the characteristic radius of plasma (contraction radius) determined from relationship $r_0^2 \approx 1.32r_g^2 + r_J^2$, where r_g and r_J are the characteristic radii of contraction with a dominant gas or electronic thermal conductivity, respectively, in the heat transfer process. These radii can be calculated from the following relationships:

$$r_g^2 = \frac{16kT_e^2\kappa\zeta_T}{q_0E_I}, \quad r_J^2 = \frac{11.6kT_e^2(\kappa_e + \kappa_{rec})}{q_0E_I}.$$

Note that the physical meaning of the contraction radius in the given model is that the current density at such a distance from the discharge axis decreases approximately by a factor of 15 to 20.

Additional conditions for the system of equations (8a) to (8f) are the plasma quasi-neutrality $n_e = n_i$, constancy of the electric field intensity E = const and external pressure p = const.

The system of equations (8a) to (8f) differs from the similar system used in study [2] in that it allows for ions and Coulomb collisions present in the arc plasma, effects of non-ideality of the low-temperature plasma, and influence of the geometrical factor on heat transfer (8b).

Thermal function S is determined as follows:

$$S = \int_0^{T_e} (\kappa_e(T_e') + \kappa_{rec}(T_e'))dT_e' + \int_0^{T_0} \kappa(T')dT'.$$

For individual inert gases at $k(T) \infty T^{\gamma}$ and at values of the gas and electron temperatures assumed to be equal to their values at the discharge axis, it holds that

$$S = (\kappa_e(T_e) + \kappa_{rec}(T_e))\frac{2\kappa T_e^2}{E_I} + k(T_0)\frac{T_0}{1+\gamma}.$$

In a case of inert gas mixtures, allowing for a small difference between exponents γ, the following simple approximate expression can be derived for the thermal function:

$$S = (\kappa_e(T_e) + \kappa_{rec}(T_e))\frac{2kT_e^2}{E_I} + k^*(T_0)T_0,$$

where $\kappa^*(T_0)$ is determined for a mixture of two inert gases as

$$\kappa^*(T_0) = \frac{\kappa_1}{\left(1 + A_{12}\frac{x_2}{x_1}\right)(1+\gamma_1)} + \frac{\kappa_2}{\left(1 + A_{21}\frac{x_1}{x_2}\right)(1+\gamma_2)}.$$

Therefore, the system of equations (8a) to (8f) makes it possible to calculate E, T_e, T_0, n_e, n_a, N and r_0 at the set values of arc current I and pressure p.

Results and discussion. The resulting system of equations is a model of the arc discharge on a condition that heat released in the plasma channel is transferred due to thermal conductivity to the walls of the discharge chamber, where a specific temperature is maintained. Naturally, the tungsten cathode welding arc has no stabilising wall. The role of this wall is played by external factors, such as flows of a shielding gas caused by the external blow, convection [1, 18, 19] or evaporation of the anode surface [1, 18]. Note that it is recommended to take the discharge glow radius as the wall radius for an open arc [19].

This model describes the welding «long arc», where the heat flow is directed to the walls [18, 20], whereas in the «short arc» it is directed mostly to electrodes. However, based on the results of study [21], it is appropriate to use the «long arc» model to describe the tungsten cathode welding arc.

Reportedly, characteristics of the arc, where the heat transfer due to radiation is negligibly small, are described by curves with variables r/R (reduced radius), ER (reduced voltage) and I/R (reduced current) [22]. Figure 1 shows the calculated generalised volt-ampere characteristics with variables $ER - I/R$, and Figure 2 shows the calculated and experimental curves for dependence of the electron temperature upon reduced current I/R [19, 23]. Comparing them allows a conclusion that, if the current density in the arc is $j_0 < 1$ kA/cm^2, the difference between the calculated and experimental results is no more than 30 %. At a higher current density the calculated data are too high, as in this case no allowance is made for the radiation both in heat transfer and in ionisation balance of plasma [24]. Note that for the argon arc the said range of the current density corresponds to a temperature below 11,000 K, at which the radiation is usually neglected [23].

Results of the calculation of parameters of the arcs at the set values of I are given in the Table and shown in Figure 3. The data obtained with allowance for those given in study [2] result in the following description of contraction of the arc in inert gases and their mixtures, the radiation being neglected (Figure 4). The most significant contraction of the arc discharge takes place in a case where the heat transfer occurs due to the gas thermal conductivity. This corresponds to conditions of the welding arc with a relatively low electron temperature and, hence, low currents. As the current and electron temperature are

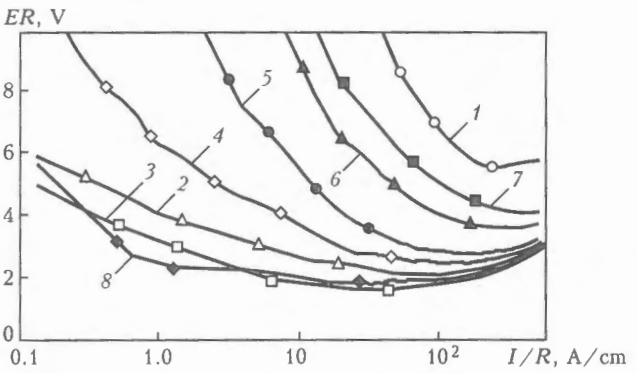

Figure 1. Calculated volt-ampere characteristics ($ER - I/R$) for the atmospheric-pressure arc discharges: *1* — helium; *2* — argon; *3* — xenon; *4* — helium + argon mixture (10 + 90 vol.%); *5* — same (20 + 80 vol.%); *6* — same (50 + 50 vol.%); *7* — same (70 + + 30 vol.%); *8* — argon + xenon mixture (50 + 50 vol.%)

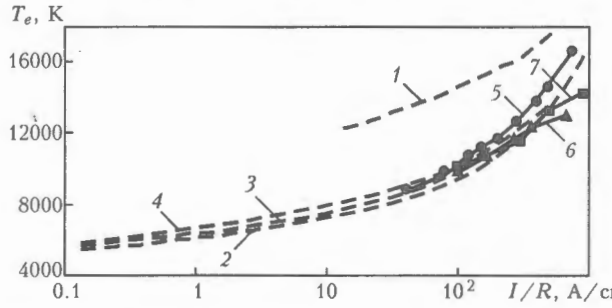

Figure 2. Dependence of electron temperature T_e in the atmospheric-pressure arc upon reduced current I/R: *1* — helium; *2* — argon; *3* — helium + argon mixture (30 + 70 vol.%); *4* — same (70 + 30 vol.%); *5–7* — argon; *5* — generalisation of experimental results [21]; *6, 7* — experimental results at R = 3 and 2 mm, respectively [24]

increased, the region occupied by plasma grows. Moreover, in a gas, for which the Ramsauer effect takes place, this growth is much more intensive than in a gas where this effect is absent (see Figure 4, *a* and *b*, region *A*).

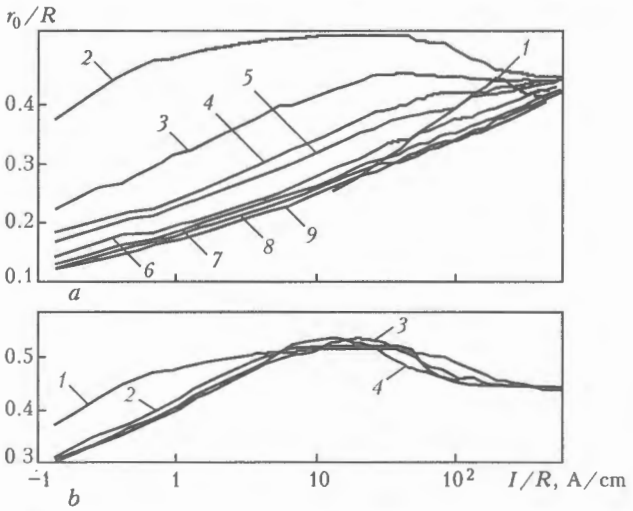

Figure 3. Dependence of the reduced arc contraction radius r_0/R upon reduced current I/R in argon + helium (*a*) and argon + xenon (*b*) mixtures: *1* — helium; *2* — argon; *3, 4* — helium + argon (10 + 90 and 20 + 80 vol.%, respectively); *a*: *5, 6* — helium + + argon (30 + 70 and 50 + 50 vol.%, respectively); *7–9* — helium + + argon (70 + 30, 80 + 20 and 90 + 10 vol.%, respectively); *b*: *1* — argon; *2* — xenon; *3, 4* — argon + xenon (10 + 90 and 20 + + 80 vol.%, respectively)

As the current is further increased, the arc transfers to a condition where the electronic thermal conductivity becomes dominant and the contraction radius value is stabilised (see Figure 4, region *B*). Besides, electrons transfer their energy primary at collisions with neutral atoms. In this case $r_0/R \approx$ const and, hence, $r_0 \infty R$ [25].

If the arc current continues growing, this leads to increase in the electron temperature and degree of ionisation of the gas environment. The effect of collisions between electrons and ions is intensified. Therefore, the discharge region for the wall stabilised arc starts decreasing in size (compare Figures 4, *a* and 4, *b*, region *C*). Note that this effect was employed to make high-power arc light sources [26]. At a still higher current, the discharge region becomes stabilised in size (compare Figures 4, *a* and 4, *b*, region *D*). However, it should be noted that, when considering contraction of the arc with dominant electron–ion collisions, it is necessary to account for the effect of radiation both on heat transfer and on ionisation processes in plasma. The radiation effect causes substantial changes in the shape of curves in regions *C* and *D* (see Figure 4).

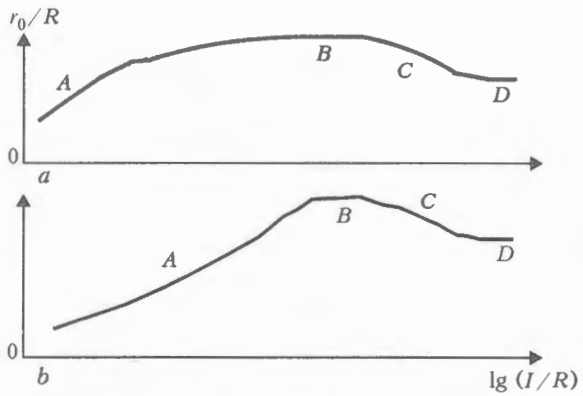

Figure 4. Dependence of the reduced arc contraction radius r_0/R upon reduced current I/R for gas with (*a*) and without (*b*) Ramsauer effect (see explanation in the text)

Parameters of arc discharges at atmospheric pressure and R = 0.75 cm

Gas	*I, A*	r_0, *mm*	*E, V/cm*	T_0, *K*	T_e, *K*	*Q, W/cm*	q_0, *W/cm*^{3}	$\alpha \cdot 10^2$	ξ	η
Helium	200	4.45	2.76	8150	10700	$1.7 \cdot 10^3$	$6.1 \cdot 10^3$	8.6	$1.3 \cdot 10^{-2}$	$1.5 \cdot 10^5$
Helium + argon (30 + 70 vol.%)	100	3.10	4.17	9500	10520	$4.2 \cdot 10^2$	$1.7 \cdot 10^3$	2.9	$4.1 \cdot 10^{-1}$	$6.2 \cdot 10^3$
Helium + argon (70 + 30 vol.%)	200	3.00	5.68	11470	12300	$1.1 \cdot 10^3$	$4.9 \cdot 10^3$	8.3	$4.3 \cdot 10^{-1}$	$5.0 \cdot 10^3$
Argon	100	3.70	2.90	8570	10200	$2.9 \cdot 10^2$	$8.1 \cdot 10^2$	2.4	$2.5 \cdot 10^{-1}$	$1.3 \cdot 10^4$
Argon + xenon (80 + 20 vol.%)	100	3.52	2.93	9200	10200	$4.4 \cdot 10^2$	$1.3 \cdot 10^5$	9.4	$1.4 \cdot 10^{-1}$	$1.2 \cdot 10^5$
Argon + xenon (20 + 80 vol.%)	100	3.45	2.63	8820	9330	$2.6 \cdot 10^2$	$7.8 \cdot 10^3$	8.8	$1.1 \cdot 10^{-1}$	$3.6 \cdot 10^5$
Xenon	100	3.44	2.54	8940	9360	$2.6 \cdot 10^2$	$7.3 \cdot 10^2$	1	$8 \cdot 10^{-2}$	$5.1 \cdot 10^5$

Note. Q — arc power; ξ — ratio of gas to electronic thermal conductivity; η — parameter of established local thermal-cycling equilibrium.

It should be emphasised that argon, krypton and xenon are gases with a pronounced Ramsauer effect, which has the quantum nature and is characterised by the presence of a minimum cross-section of electron–atom collisions for electrons with an energy a bit lower than 1 eV. This phenomenon determines «transparency» of a slightly ionised gas for such electrons and causes increase in difference of the electron temperatures from the gas one, which decreases contraction of the arc. However, the Ramsauer effect can be neutralised in gas mixtures. For example, an addition of helium, for which the said effect does not take place, to argon leads to a substantial intensification of arc contraction (see Figure 3, *a*). Besides, a marked increase in contraction takes place with an addition of 20–30 vol.% helium to argon. As the volume fraction of helium in a mixture is further increased, a relative increase in contraction goes down. Therefore, in terms of the arc contraction and increase in the penetration depth, the mixture with an addition of 20–50 vol.% helium is most efficient for TIG welding. Note also that the arc discharge in the helium + argon mixture can be contracted to a higher degree than in pure helium. This can be achieved at sufficiently high currents and at a helium content of the mixture equal to more than 50 vol.%. At the same time, compared with contraction in pure gases, no qualitative change in the character of contraction takes place in the argon + xenon mixtures (see Figure 3, *b*), as the Ramsauer effect takes place in both cases.

Therefore, contraction of the arc discharge in mixtures of inert gases strongly depends upon the proportion of the mixture components. Its change has a great effect on thermal-physical characteristics of the mixture and general characteristics of electron–atom collisions, which determine electrophysical parameters of the arc under specific conditions of the discharge.

Thus, contraction of the welding arc burning at tungsten cathode in inert gas mixtures depends to a substantial degree upon the proportion of the mixture components. This is attributable to the fact that variation in the concentration of the components has a high effect on thermal-physical properties of the mixture and general characteristics of electron–atom collisions, which determine electrophysical parameters of the arc under its specific burning conditions.

Contraction of the arc discharge in a specific gas mixture is most significant in a case where the gas thermal conductivity dominates in the heat removal process.

The fact that a gas in which the arc is burning has the Ramsauer effect increases «transparency» of the gas environment for electrons, which decreases contraction of the arc discharge in a corresponding temperature range. However, the Ramsauer effect in gas mixtures can be neutralised through a proper selection of composition of a gas mixture. Thus, addition of a specific amount of gas without the Ramsauer effect to that with the Ramsauer effect leads to a considerable decrease in «transparency» of the gas environment for electrons, which increases the arc contraction. This approach opens up the opportunities for controlling contraction of the welding arc though adjusting the working environment composition.

1. Paton, B.E., Zamkov, V.N., Prilutsky, V.P. et al. (2000) Contraction of the welding arc caused by the flux in tungsten-electrode argon-arc welding. *The Paton Welding J.*, **1**, 5–11.
2. Poritsky, P.V., Prilutsky, V.P., Zamkov, V.N. (2004) Effect of a shielding gas on a contraction of the tungsten-cathode welding arc. *Ibid.*, **6**, 2–9.
3. Shashkov, A.G., Abramenko, T.N. (1970) *Thermal conductivity of gas mixtures*. Moscow: Energiya.
4. Reed, R., Prausnits, J., Sherwood, T. (1982) *Properties of gases and liquids*. Leningrad: Khimiya.
5. Zhdanov, V.M. (1982) *Transfer phenomena in multi-component plasma*. Moscow: Energoatomizdat.
6. Buzhdan, Ya.M. (2002) On heat flow density and diffusion motive forces in multi-component ideal gas. *Teplofizika i Aeromekhanika*, 9(**11**), 133–141.
7. Sinkevich, O.A., Stakhanov, I.P. (1991) *Physics of plasma*. Moscow: Vysshaya Shkola.
8. Eletskii, A.V., Smirnov, B.M. (1996) Nonuniform gas discharge plasma. *Physics-Uspekhi*, 39(**11**), 1137–1156.
9. Smirnov, B.M. (1997) Contraction of positive column of high-pressure arc. *Teplofizika Vys. Temperatur*, 5(**1**), 14–18.
10. Eletsky, A.V., Palkina, L.A., Smirnov, B.M. (1975) *Transfer phenomena in slightly ionised plasma*. Moscow: Atomizdat.
11. Smirnov, B.M. (2002) Kinetics of electrons in gases and condensed systems. *Uspekhi Fiz. Nauk*, 172(**12**), 1411–1447.
12. Griem, H.R. (1962) High-density correction in plasma spectroscopy. *Physics Rev.*, **128**, 997–999.
13. Fastovsky, V.G., Rovinsky, A.E., Petrovsky, Yu.V. (1972) *Inert gases*. Moscow: Atomizdat.
14. Radtsig, A.A. (1981) Diffusion of charged particles in gas in the constant electric field. *Khimiya Plazmy*, **8**, 230–263.
15. Smirnov, B.M. (2000) Cluster plasma. *Physics-Uspekhi*, 43(**5**), 453–491.
16. Golant, V.E., Zhilinsky, A.P., Sakharov, I.E. (1977) *Principles of plasma physics*. Moscow: Atomizdat.
17. Hacksly, L., Crompton, R. (1977) *Diffusion and drift of electrons in gases*. Moscow: Mir.
18. Zhovtyansky, V.A., Patriyuk, V.M. (2000) Specifics of heat release from electric arc in copper vapours. *Ukr. Fizich. Zhurnal*, 45(**9**), 1059–1066.
19. Batenin, V.M., Minaev, P.V. (1969) On temperature at the electric arc axis in argon. *Teplofizika Vys. Temperatur*, 7(**2**), 208–212.
20. Zhukov, M.F., Koroteev, A.S., Uryukov, B.A. (1975) *Applied dynamics of thermal plasma*. Novosibirsk: Nauka.
21. Eroshenko, L.E., Zamkov, V.N., Prilutsky, V.P. (1997) Study of anode vapour glow in arc during tungsten-electrode argon-arc welding over a flux layer. *Avtomatich. Svarka*, **11**, 11–13.
22. Desyatkov, G.A., Engelsht, V.S. (1985) *Theory of cylindrical arc discharge*. Frunze: Ilim.
23. Asinovsky, E.I., Kirillin, A.V., Nizovsky, V.L. (1992) *Stabilised electric arcs and their application in thermal-physical experiment*. Moscow: Nauka.
24. Biberman, L.M., Vorobiov, V.S., Yakubov, I.T. (1982) *Kinetics of non-equilibrium low-temperature plasma*. Moscow: Nauka.
25. Rakhimov, A.T., Ulinich, F.R. (1969) Contraction of cylindrical gas discharge. *Doklady AN SSSR*, 187(**1**), 72–74.
26. Vasserman, A.L. (1989) *Xenon tubular lamps and their application*. Moscow: Energoatomizdat.

FE-MODELLING OF THE THERMOMETALLURGY AND STRESS-DISTORTION BEHAVIOUR DURING PTA HARDFACING

U. SEMMLER, K. ALALUSS and K.-J. MATTHES
Institute of Manufacturing and Welding Technology, University of Technology, Chemnitz, Germany

The paper deals with the process of plasma transferred arc (PTA) deposition of thick hardfacing layers (vanadium-based alloys V12 and V18) on the base material (structural steel S355J0). The differences in the thermo-mechanical properties, local thermo-plastic deformations and phase transformations may cause high residual stress and distortion. The transient thermo-elastic-plastic behaviour of the PTA material deposition is investigated by means of the 3D Finite Element Method (FEM). All thermo-mechanical parameters are dependent on the temperature. The simulated results are compared with measurements of temperature distribution and distortions in order to increase the quality of the numerical models. Using the verified and improved FE-models one can study the influence of welding parameters on the deformations and residual stresses with the aim to optimize the weldments. For thick deposit layers the austenite-martensite transformations have a significant influence on the residual stresses and distortions. Technical applications are shown.

Because of its high-temperature strength Stellite can be applied in hardfacing of forming tools working in the temperature range beyond 600 °C. In [1] the authors presented the modeling and FE-simulation of the PTA welding process applied to such forming tools. The paper considered in detail the FE-models, results of the numerical simulations and comparison with experiments.

Other excellent and very hard deposit materials are iron-based alloys with a high percentage of vanadium (materials V12 and V18 with 12–18 % V). As these materials do not have high-temperature strength they can be used essentially under cold or moderate warm conditions. Examples are technical blades for cutting of paper, waste (electronic and other), or bones. These blades may have lengths of more then 4 m. Figure 1 shows a typical cross-section of the blank. The blade edges are subject to high wear. That is why the groove of 30 mm breadth is filled with one layer V12/V18 of 4 mm depth using PTA powder deposit welding. The process was investigated experimentally and by means of numerical simulation.

In these investigations we were interested in residual stresses leading to significant distortions both «about the thickness» (V_t) and «about the high edge», i.e. about the breadth (V_b) (Figure 2). For very long blades the remaining distortion V_b can exceed 30 mm. In such cases, re-machining eliminates the hardfacing completely, i.e. produces a scrap component.

To obtain built-up welds with low distortion and low residual stresses, knowledge is necessary about the weld pool size, as well as about the thermal-metallurgical and mechanical behaviour during the process of welding, heat treatment, and end machining. A possibility to consider these questions in combination with their mutual dependencies, as well as to investigate the processes with temperature-dependent material properties is the numerical modelling and simulation by means of the FEM. First, there is the necessity to know the essential mechanical and thermo-physical processes during build-up welding. Secondly, one should to be able to model these processes including the important physical interactions and to omit the irrelevant ones. Finally, methods are required for the solution of the models and calculation of the significant values of the processes.

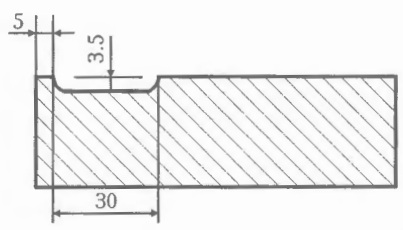

Figure 1. Typical groove cross-section of technical blades

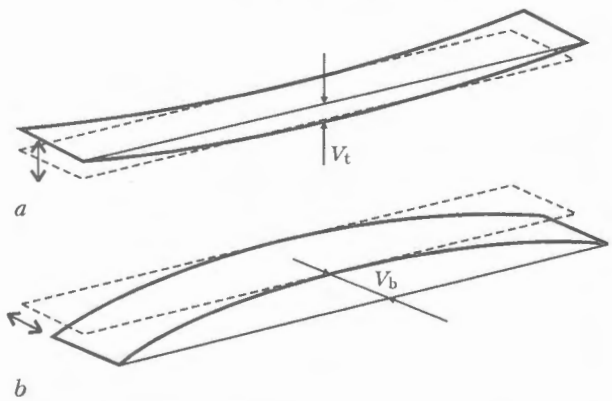

Figure 2. Distortions about the thickness V_t (*a*) and about the breadth V_b (*b*) of blades

*This article was presented at the 2nd International Conference on Mathematical Modelling and Information Technologies in Welding and Related Processes (Katsiveli, Crimea, September 13–17, 2004). — Kiev: PWI.

The paper presents the FE-models used to calculate the distortions and residual stresses resulting from build-up welding. These calculations are compared with the results of experimental investigations. Some experiments were used to adjust unknown or insufficient known model parameters.

FE-modelling of the welding process. *Thermo-mechanical model*. The temperature distribution is described by the following non-stationary and non-linear equation of heat conduction and convection:

$$c_p\rho \frac{\partial T}{\partial t} = \nabla(\lambda\nabla T) - \nabla(c\rho \vec{v}T) + q_{vol}. \quad (1)$$

For long cutting blades, and if not considered the weld pool convection (expressed by the convective term in the equation) and if the thermal source moves with the constant and linear welding velocity v_s, the heat conduction and convection equation can be written in a moving co-ordinate system:

$$c_p\rho v_s \frac{\partial T}{\partial x} = \nabla(\lambda\nabla T) + q_{vol}. \quad (2)$$

The equation (2) is used to adjust the thermal boundary conditions [1], and can also reduce the computational costs in the FE-models. But the calculation of temperature distribution using (2) requires that also the mechanical problem has to be solved in the moving co-ordinate system which causes some problems in calculating realistic distortions. That is why all thermo-mechanical simulations are carried out using equation (1) in a body-fixed co-ordinate system omitting the convective terms (the weld pool convection is approximately modelled by an artificially increased thermal conductivity).

The different materials are considered to be homogenous and isotropic with depending on the temperature thermo-physical parameters λ and ρc. The thermal boundary conditions read:

• The plasma arc is modelled by a moving elliptic source with Gaussian energy distribution (Goldak's heat source [2]). Because of the thick layer deposit welding a volumetric Goldak's heat source fits the real process better than a surface source (the low welding velocity implies equal values of heat distribution for the forward and the rear part of the moving heat source):

$$q_{vol} = q(x, y, z) = \frac{6\sqrt{3}Q}{abc\pi\sqrt{\pi}} e^{\frac{-3x^2}{a^2}} e^{\frac{-3y^2}{b^2}} e^{\frac{-3z^2}{c^2}}. \quad (3)$$

Using weave-bead welding the torch moves with a welding speed v_s of approximately 1 mm·s^{-1} in the welding direction (y-axis) and with a maximal velocity v_w = 7 mm·s^{-1} and a width W = 28 mm in the transversal direction. The periodic weave movement is $x_W(t)$. As the heat source oscillates with a high velocity v_w in comparison with the welding speed v_s the heat source can be considered to be stationary in a moving co-ordinate system by means of averaging the sources about one pendulum period 1/f:

$$q_{vol} = q(x, y, z) = \int_0^{1/f} q_{lin}(x + x_W(t, y, z)\partial t. \quad (4)$$

As shown in Figure 3, on both sides of the seam the heat source density has a maximum because the pendulum movement changes its direction at these points and, additionally, a delay in time is chosen in these positions.

• On all sides of the target the thermal transfer is defined by radiation and convection to the surrounding media:

$$-\lambda \frac{\partial T}{\partial n} = \alpha(T - T_0) + \varepsilon C_0(T - T_0)^4, \quad (5)$$

whereby the radiation is essential only on the upper target surface. Therefore, the emissivity ε is set to be equal to zero on the other boundaries.

The total heat flux Q is defined by means of the experimentally measured values of welding current, voltage and velocity with thermal efficiency in consideration. The temperature-dependent material parameters are taken from [3, 4] or are given by the manufacturers of the materials. The base material is structural steel S355J0, for its chemical composition and for the composition of the filler materials V12 and V18 see Tables 1 and 2.

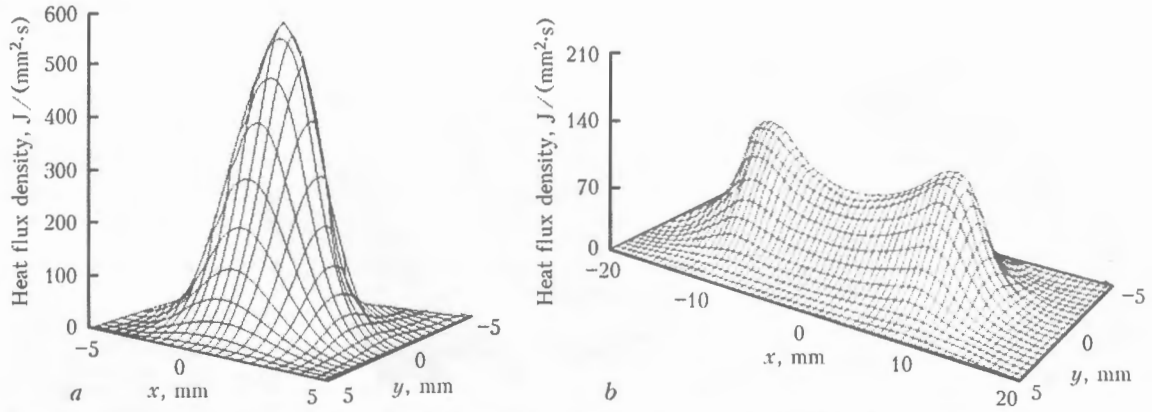

Figure 3. Heat density distribution for linear (*a*) and weave (*b*) welding at weave width of 28 mm, weave velocity of 7 mm·s^{-1} and delay time of 0.6 s

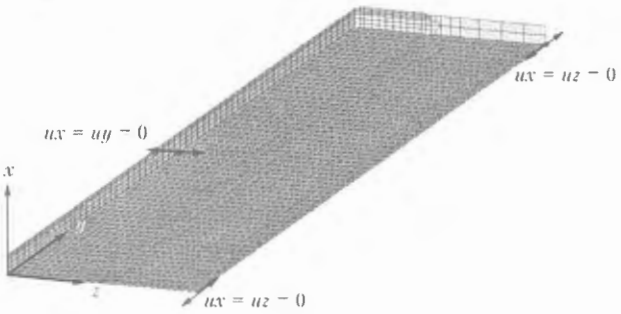

Figure 4. Mechanical boundary conditions for rigid body movement exclusion

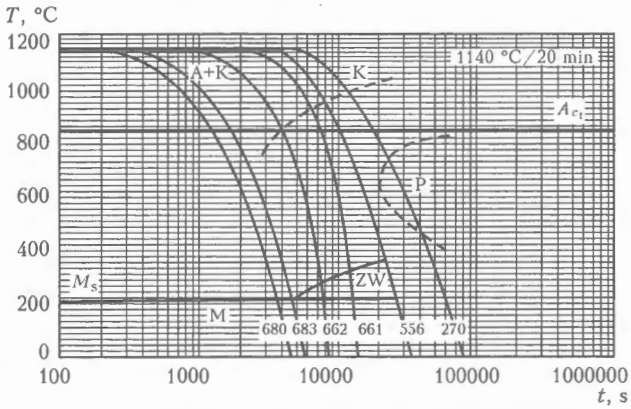

Figure 5. Measured CCT diagram of the filler material V12

The temperature distribution in the specimens strongly depends on the thermal transfer coefficient between the target and the welding equipment desk. Because of incomplete contact between these two surfaces it is impossible to find the parameter in the literature. Measurement is difficult and not accurate. That is why temperature measurements were carried out using thermocouples, a simple stationary FE-model was developed and the parameters Q and α have been adjusted with measured temperature values [1].

Using the calculated temperatures and metal phases at all time steps of the thermal cycle the temporal development of the thermo-elastic-plastic strains is computed over the same time interval. Because in the welding experiments the clamping of the parts was incomplete, only such mechanical boundary conditions were chosen which assure the stability of the mechanical model (exclusion of rigid body movements in the numerical models) (Figure 4).

The total strains consist of elastic, plastic, thermal and transformation induced strains

$$d\varepsilon_{ij}^{\text{sum}} = d\varepsilon_{ij}^{\text{el}} + d\varepsilon_{ij}^{\text{pl}} + d\varepsilon_{ij}^{\text{th}} + d\varepsilon_{ij}^{\text{tr}}. \quad (6)$$

Table 1. Chemical composition of base material

Material	Chemical composition, %					
	C	Fe	Mn	N	P	S
S355J0	≤ 0.2	Bal.	1.24	–	0.012	0.007

To calculate the plastic strains the theory of incremental plasticity is applied using isotropic multilinear, depending on temperature yield curves for the considered materials. Steel and filler materials which underlie austenite-ferrite transformations cause volumetric changes during the transformation. These changes lead to additional strains, resulting in additional residual stresses. To take into consideration the effects of metallurgical transformation, CCT diagrams have to be included into the numerical simulation. Whereas for the steel S355J0 the welding CCT diagram is known [5], for the filler V12 it was measured (Figure 5). For any cooling rate the martensite transformation starts at temperature M_s = 200 °C. At the ambient temperature the remaining austenite portion is approximately 30 %.

For high temperature close to the fusion temperature it is difficult to find realistic thermo-physical materials parameters in literature or to measure them. The thermo-physical and mechanical parameters can be different for several material phases. For temperatures above the fusion temperature the yield stress had been chosen very small.

FE-model and numerical realisation. The mesh of the hole cutting blade blank including the built-up layer consists of approximately 7900 8-node brick elements (Figure 6). The modelling and the calculations are carried out with the FE Code SYSWELD™ [6].

The model is used to investigate and to optimize the influence of torch energy distribution, welding speed, clamping conditions and thermal regime on the residual distortions V_t and V_b of technical blades. The work focused on investigating how the geometry of the blades (cross-section and length) affects the distortions. For that reason the basic cross-section 100 × 10 mm was scaled both in depth (10, 15, 20 and 30 mm) and in breadth (60, 100 and 160 mm). Figure 7 shows the basic, minimal and maximal cross-sections. The number of elements in the cross-section did not change. Prolongation from 500 to 1000 and 2000 mm was done by copying the mesh along the axis increasing the number of elements by factors 2 and 4.

In the first stage of the numerical process the whole non-stationary thermal-metallurgical cycle (from the

Table 2. Chemical composition of filler materials

Material	Chemical composition, %								Hardness HRC
	C	Co	Cr	Mo	Ni	Si	V	Fe	
V12	2.8	–	4.5	1.3	0.4	0.9	12.0	Bal.	62
V18	4.0	–	4.5	1.3	0.4	0.9	18.0	Same	64

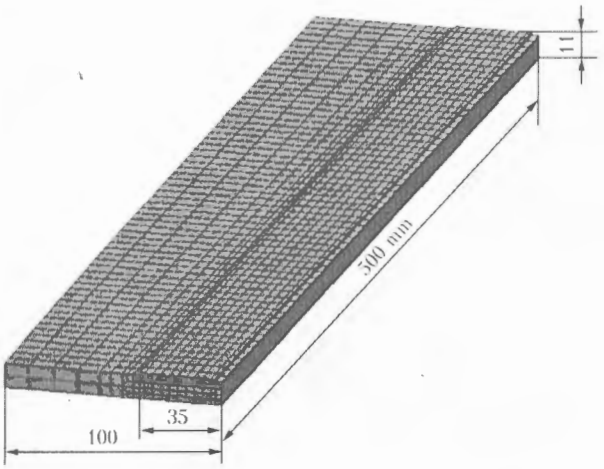

Figure 6. FE-mesh of a technical cutting blade of 500 × 100 × × 10 mm basic geometry

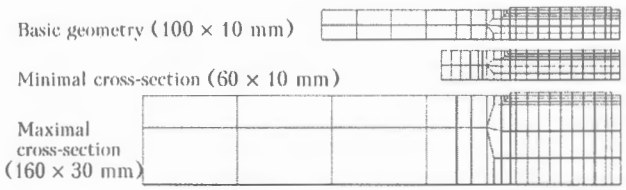

Figure 7. Basic and scaled cross sections of the FE-model

beginning of welding to the end of cooling) was considered, and, hereafter, on the base of calculated non-stationary temperature and phase distribution the thermo-elastic-plastic stress and deformation development. The appearance of new deposit material in the built-up layers was modelled in SYSWELD by means of the element activation during the computational process (using so-called birth and death elements). The calculations took into consideration the metallurgical transformations (CCT diagrams) and the dependencies of the thermo-mechanical properties from the material phases.

Results of the numerical simulation. After its solidification the deposit material tends to shrink. This shrinking generates tensile stresses and leads to a concave shape in thickness direction (distortion V_t), as well as perpendicular to it (distortion V_b). In contrast to Cr- and Ni-based superalloys (for example, Stellite and Ni625), the V-based filler materials perform martensite transformations at the temperature 200 °C

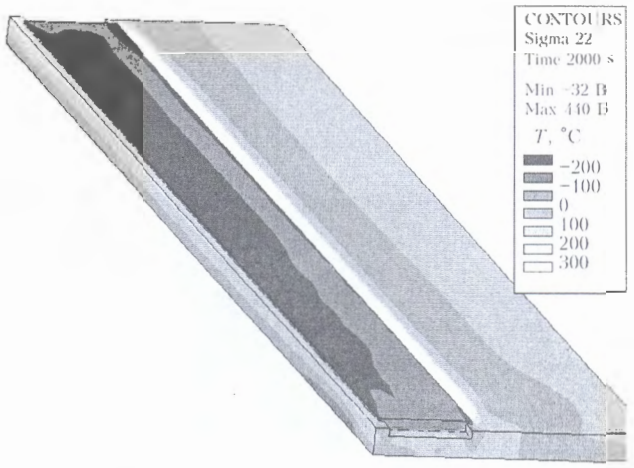

Figure 9. Residual longitudinal stress distribution after complete cooling

(see Figure 5) with a volumetric expansion of about 1 %. The models and numerical simulations include the transformation kinetics. This transformation induces expansion during cooling and leads to compressive stresses in the build-up bead. For blades of 10 mm (and partially for 15 mm) thickness these compressive stresses reverse the shape into a convex contour when the workpiece cools down under the martensite start temperature. Figure 8 shows the temperature distribution and deformation process (magnification factor 20) after 150, 400 and 500 s (end of welding) and 2000 s (almost complete cooling to ambient temperature).

The resulting longitudinal stresses range between maximal compressive stress of 328 MPa in the seam and maximal tensile stress of 440 MPa in the HAZ (Figure 9).

It is relatively easy to eliminate the distortions V_t about the thickness by clamping and straightening but the removal of the distortions V_b about the breadth is incomparably more difficult. The calculated by FEM distortions V_b compared with measured values for workpiece 500 mm length are shown in Figure 10. Two different PTA welding methods are used: with constant and with pulsed welding current. The impulse method needs less energy to melt a fixed amount of deposit material. This leads to less distortion. The heat source in the FE-model was adjusted for the

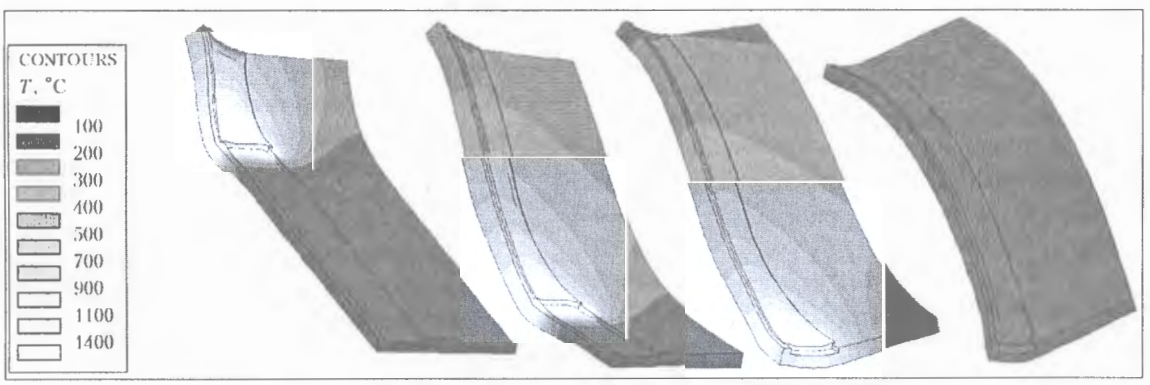

Figure 8. Temperature distribution and deformation behaviour of PTA hardfaced blade of geometry 100 × 10 × 500 mm at welding velocity 1 mm·s^{-1}

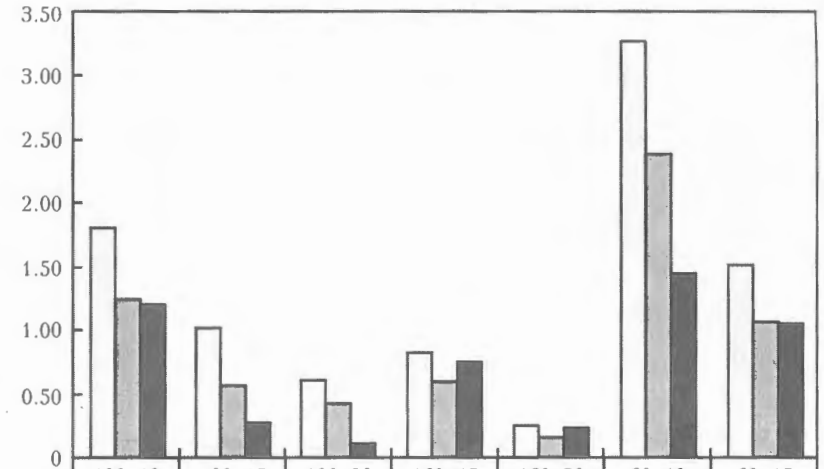

	100×10	100×15	100×20	160×15	160×30	60×10	60×15
Permanent	1.80	1.02	0.61	0.83	0.25	3.26	1.51
Impuls	1.24	0.58	0.42	0.59	0.16	2.37	1.07
FEM	1.21	0.28	0.11	0.75	0.23	1.46	1.04

Figure 10. Measured and calculated distortions (mm) about the breadth for different cross-sections

impulse regime. The simulation results agree qualitatively with the measured values but the quantitative deviations require further investigations.

Because of possible distortions of more than 30 mm, the end-working of the blades can lead to the complete disappearance of the weld seam and therefore to scrap parts. It is very important to determine in advance the expected distortions V_b. Knowing the values the compensation of the distortion can be achieved by rough-bending of the blank or by forming a curved weld seam against the expected distortions.

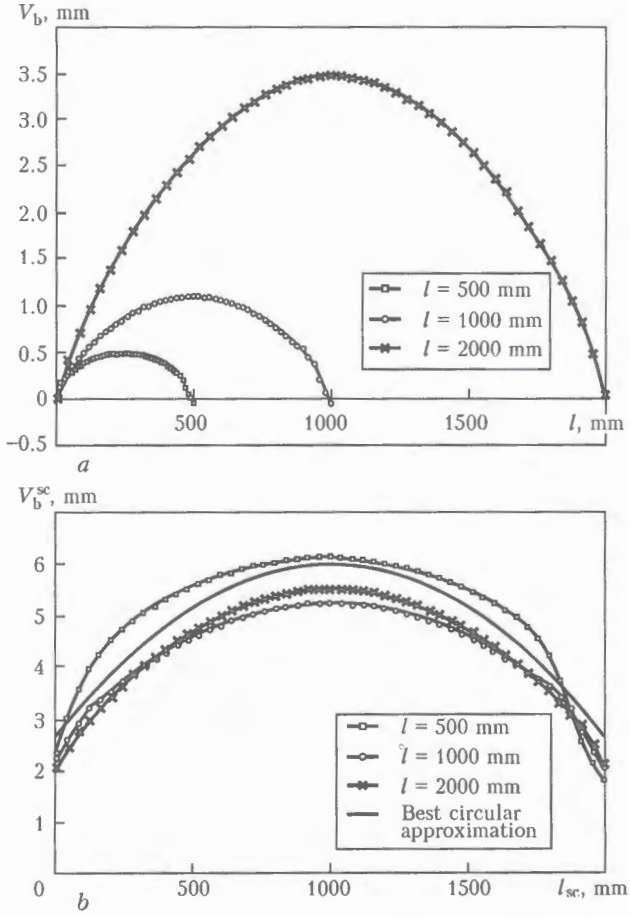

Figure 11. Comparison of calculated distortions V_b of 100 × 10 mm cross-section for different lengths: *a* — real; *b* — scaled distortions

The computation time on a PC with a 1 GHz processor is approximately 5 h for the basic model (blade length of 500 mm, i.e. 7900 elements), up to 3 days for the length of 2000 mm, and unacceptable for longer ones. Using the experimental or numerical results of short targets (for instance of the length l_0 = 500 mm) it is possible to predict the distortions of long targets ($l >> l_0$) by multiplying with a factor f. In Figure 11, *a* the distortions V_b of blades with basic cross-section are compared for different lengths. The scaling of the lengths with $f_l = l/l_0$ and of the distortions with $f = (l/l_0)^{3/2}$ gives a sufficient good approximation of the expected distortions (Figure 11, *b*).

Practical examples and concluding remarks. The first practical example, built-up welding of transverse-rolling mills, is shown in [1]. In the second practical example, the hardfacing of narrow but long technical cutting blades (Figure 12), the simulated distortions coincide in quality with the measured ones. The simulations give the possibility to investigate the effect of geometrical parameters and of various welding conditions on the workpiece distortions and to estimate the distortions of long parts having reliable results for short blades. For long blades the knowledge of expected distortions about the breadth allow forming a curved seam in order to achieve a straight seam after cooling down to ambient temperature and to reduce re-machining.

The cause of remaining quantitative deviations in the distortions is the insufficient knowledge about the real materials data, in particular the phase transformation kinetics, the dependence of the parameters on the phases and on temperature (especially close to and above the fusion point). The reduction of these deviations will be the content of further investigations.

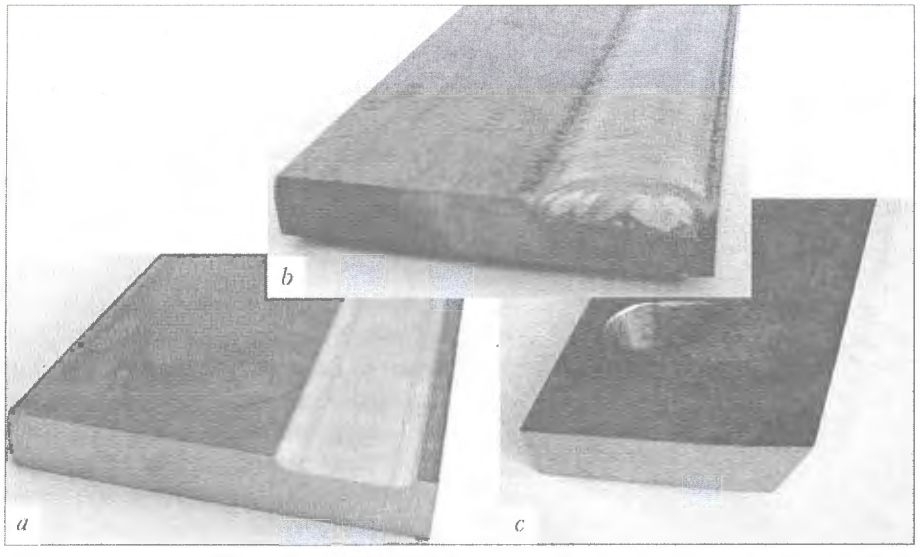

Figure 12. Hardfaced technical blades: *a* — blank part; *b* — workpiece after welding; *c* — after end machining

Other examples for applying FE-simulations on PTA build-up welding are dies for spin extrusion and hardfaced valves of big diesel engines.

Acknowledgement. *The presented theoretical and experimental investigations were promoted and supported by the German Federal Ministry of Economics and Labour (AiF project No. 12793 BR) and by the German Research Society in the context of the Special Research Section 283: Process Chains in Bulk Forming.*

1. Semmler, U., Alaluss, K., Matthes, K.-J. (2002) Finite element analysis of the PTA welding with applications to hardfacing. In: *Proc. of 1st Int. Conf. on Mathematical Modelling and Information Technologies in Welding and Related Processes* (Katsiveli, Ukraine, 2002). Kiev: PWI.
2. Goldak, J., Chakravarti, A., Bibby, M. (1984) A new finite element model for welding heat sources. *Metallurg. Transact. B*, **15**, 299–305.
3. Richter, F. (1983) Die wichtigsten physikalischen Eigenschaften von Stählen und ihre Temperaturabhängigkeit. *Stahleisen Sonderberichte*, 14(**10**).
4. Touloukian, Y.S. (1979) In: *Thermophysical properties of mater*. Vol. 14. New York.
5. Seyffarth, P., Meyer, B., Scharff, A. (1992) *Groβer Atlas der Schweiβ-ZTU-Schaubilder*. Düsseldorf: DVS.
6. (2000–2004) *SYSWELD™ Manuals*. http://www.esi-group.com)

MECHANISMS OF JOINT BOUNDARY SHAPING IN EXPLOSION WELDING

Yu.I. FADEENKO, L.D. DOBRUSHIN and **S.Yu. ILLARIONOV**
E.O. Paton Electric Welding Institute, NASU, Kiev, Ukraine

New classification is proposed for explosion welding conditions and corresponding shapes of joint boundaries, based on the ratio of inertia forces to strength forces within the welded joint formation zone. This ratio can be used to allow for dynamic characteristics of strength of the metal pairs being welded, in optimization of the explosion welding conditions and shapes of the resulting joint boundaries.

Keywords: *explosion welding, weldability region, joint formation zone, forces of inertia, strength forces, joint boundaries*

Explosion welding (EW) is performed at slanting collision of metallic bodies at low angles at the velocity of hundreds of meters per second. It was experimentally established that the main parameters determining the welding conditions, are the angle of collision, γ, and velocity of contact point displacement, v_c. The region of possible EW performance, so-called weldability window (WW) is defined in the plane of γ–v_c parameters (Figure 1).

Metal flow, which develops in the zone of joint formation in EW, belongs to the same class as the flow with formation of cumulative jets. In γ–v_c plane, the WW region is adjacent to the cumulative region. Similar to cumulation, in EW a concentration of flowing metal kinetic energy is found near the contact point of the colliding surfaces, although the values of the coefficients of energy concentration are not so high. Direct experimental measurements confirm that the main part of the flyer plate kinetic energy evolves in the joint formation zone [1]. A strong welded joint

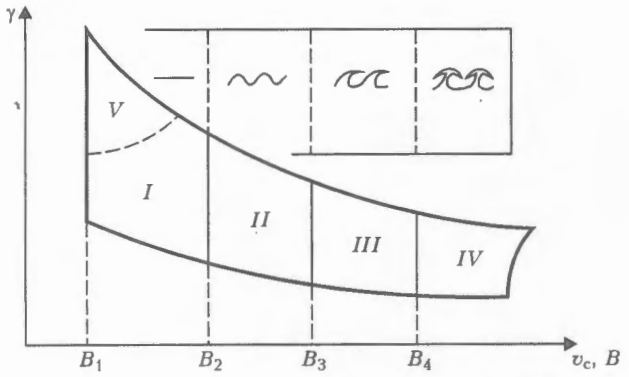

Figure 1. Regions of different dissipative structures in WW (shapes of contact surfaces corresponding to regions *I–IV* are shown on top)

can form, if excess kinetic energy is removed from the joint formation zone through its dissipation as heat due to the work consumed by plastic deformation of the metal or by some other method.

The purpose of this study is analysis and physical substantiation of the classification of dissipative processes running in the joint formation zone, based on the ratio of inertia forces to strength forces.

Density of metal flow kinetic energy in the joint formation zone can be characterized as value $\rho v_c^2/2$. Bulk density of the evolved thermal energy is given by a product of dynamic yield point, σ, by the average value of plastic deformation, ε, of the metal in the joint formation zone.

Dimensionless value

$$B = \rho v_c^2/2\sigma\varepsilon, \qquad (1)$$

which is the ratio of kinetic energy bulk density and work of plastic deformations, characterizes the ability of plastic deformation mechanisms to scatter the kinetic energy of the flyer plate. For each fixed γ value a change of v_c is accompanied by a certain change of $\sigma\varepsilon$ and B. Therefore, the WW is divided into regions *I–IV* (Figure 1) with different efficiency of absorption of shock energy due to plastic deformation of the joint formation zone.

On WW left flange velocity values v_c are small, so that $B < 1$. In this WW region the thickness of the joint formation zone is minimum, and it is determined by the same dependence as the cumulative jet thickness [2, 3]. In particular, at a symmetrical collision of the two plates the thickness of the cumulative jet and the joint formation zone are equal

$$\delta_{c.j} = 2\delta[1 - \cos(\gamma/2)], \qquad (2)$$

where δ are the thicknesses of each of the colliding plates. For small collision angles usually used in EW this expression can be replaced by a simplified

$$\delta_{c.j} = \delta\gamma^2/4. \qquad (3)$$

At small v_c, the thickness of plates (2) and (3) turns out to be quite sufficient for kinetic energy dissipation. A gradual increase of the kinetic energy density at v_c rise is compensated for by an increase of the average value of plastic deformation in the joint formation zone. In this range of v_c values (Figure 1, region *I*) a joint with a smooth (waveless) boundary forms. However, the capability of joint formation zone of the thickness determined by (2) and (3) for kinetic energy dissipation is limited by that as deformation ε increases, the metal is heated, and its deformation resistance decreases. On the right boundary of region *I* joints with very large ε values (up to hundreds of percent) can be made, which correspond to heating practically up to the melting temperature, deformation resistance dropping to zero and formation of a smooth «immersed jet» [4], following the contact point. Reference [5] puts forward an assumption of the loss of stability of a uniform field of deformation velocity in EW in region *I* and formation of a considerably deformed band similar to that of an adiabatic shift. This band forms at certain critical velocity v_c, depending on grain size. Its presence is regarded as a condition to produce a strong joint.

Beyond the right boundary of region *I* the thickness of the joint formation zone determined by (2) and (3) is insufficient for a complete dissipation of the kinetic energy. Excess kinetic energy is consumed in formation of periodic wave disturbances of the joint boundary, its surface becoming wavy. As a result, the thickness of the joint formation zone increases by a value equal to a double wave amplitude $2a$. In the range of wavy joint surfaces of WW region *II* increase of v_c and the concurrent increase of kinetic energy density is compensated for by a increase, and together with it also of the thickness of joint formation zone and average deformation ε. Similar to the previous case, increase of the values of ε and metal heating temperature leads to qualitative changes. The mode of linear increase of regular wave disturbances of the boundary (region *II*) is replaced by the mode of non-linear wave disturbances with formation of «white caps» and turbulence on the wave crests and, finally, melt section in region *III* (Figure 2, *a*).

At further increase of v_c, the capabilities for increasing the intensity of kinetic energy dissipation due to the strength forces are exhausted ($B >> 1$). In WW region *IV* the excess kinetic energy is imparted to short sections of cumulative jets, alternatively emitted by one of the surfaces and hitting the opposite surface of the joint (Figure 2, *b*). Features of the mode of joint formation in region *IV* are described in [6]. Angle φ of flow rotation in the sections of cumulative jets in this mode (Figure 2, *b*) reaches 120° (180° would correspond to ideal cumulation). The velocity, at which the head of the jet section collides with the opposite surface of the joint, is higher than v_c, and may reach 4 to 5 km/s. Excitation of shock waves at high-velocity collisions becomes the main mechanism of energy dissipation in region *IV*; velocity of energy removal from the joint formation zone by the shock waves exceeds the velocities of motion of the jet sections and sound in the metal. This mode is characterized by the following parameters of the dis-

sipation zone: thickness of the layer of initial energy release of 20 to 100 μm; normal and tangential components of the collision velocity of up to 3 to 4 km/s; pressure of up to 100 GPa (1 Mbar); temperature up to melting temperature; cooling rate of more than $1 \cdot 10^8$ °C/s. Nature of plastic deformation in this zone is similar to shear under pressure in Bridgeman anvils. However, unlike static Bridgeman anvils the deformation rate in EW is very high. Characteristic features of microscopic dissipative structures, developing at the subgrain level (cellular structures) correspond to these conditions [7–9].

The issue of the values of dynamic yield point of the metal achieved in the joint formation zones is a subject for a separate discussion. It is known that the metal yield point increases with deformation rate $\dot{\varepsilon}$. Dependence $\sigma = \sigma(\dot{\varepsilon})$ is usually interpreted as a manifestation of viscous forces

$$\sigma = \sigma_0 + \mu_{ef}\dot{\varepsilon}, \qquad (4)$$

where σ_0 is the stress of quasistatic deformation; μ_{ef} is the effective viscosity of the metal.

The nature of $\mu_{ef} = f(\dot{\varepsilon})$ dependence in the case of a high deformation rate was experimentally studied, right up to $\dot{\varepsilon} \cong 1 \cdot 10^4 - 1 \cdot 10^5$ s^{-1}. In the works of G.V. Stepanov and his associates [10, 11] a dependence of μ_{ef} on the deformation rate in steels and aluminium alloys was established. Three characteristic ranges of velocity were found. At $\dot{\varepsilon} < 30$ s^{-1} the viscosity contribution to deformation resistance almost does not depend on deformation and is quite small. At $\dot{\varepsilon} = 30$ and $3 \cdot 10^5$ s^{-1} viscosity rises jump-like, which is followed by its gradual decrease (second jump is related to transition from the subbarrier mode of dislocation sliding to overbarrier mode). At $\dot{\varepsilon} = 1 \cdot 10^4 - 1 \cdot 10^5$ s^{-1} the contribution of viscous forces prevails. In this velocity range the dynamic yield point of some metals can be several times higher than the static one [12]. According to the data of [11], at $\dot{\varepsilon} = 1 \cdot 10^2 - 1 \cdot 10^5$ s^{-1} μ_{ef} values for steels of different strength decrease approximately from 30000 to 1500 Pa·s. In view of the absence of experimental data, extrapolation to still higher $\dot{\varepsilon}$ values is unreliable. However, there is no doubt that the deformation resistance continues rising, right up to the proof stress σ_{pr}, above which the deformation resistance remains constant. This may be interpreted as absence of viscosity (if viscosity is defined by differential ratio $\mu_{dif} = d\sigma/d\dot{\varepsilon}$, then in the flow region at the proof stress $\mu_{dif} = 0$).

In typical technological modes of EW the velocity head pressure $\rho v_c^2/2$ has the same order of magnitude as σ_{pr} near the boundaries of WW regions *I* and *II*. For steels, for instance, the boundary of regions *I* and *II* corresponds to $v_c \cong 2.5$ km/s. Velocity head pressure $\rho v_c^2/ \cong 25$ GPa here is of the same order of magnitude, as σ_{pr} for iron crystalline lattice. If in this case the deformation resistance stresses turn out to be capable of neutralizing the inertia forces, they, therefore, have the same order of magnitude.

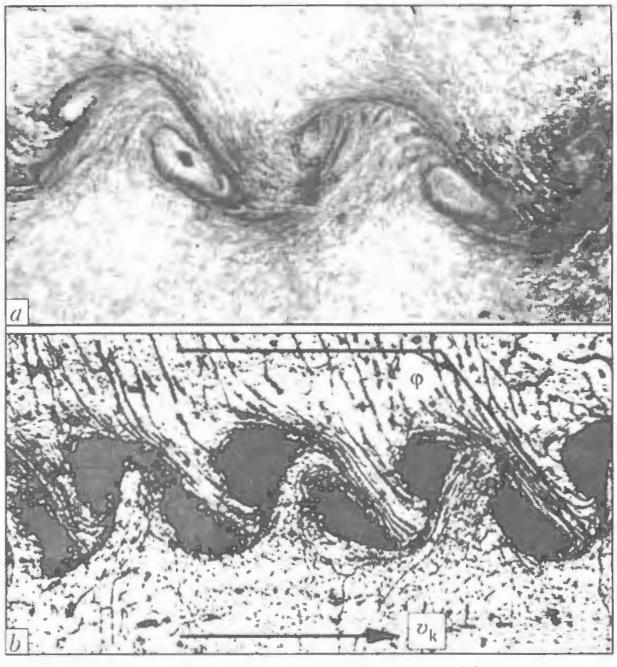

Figure 2. Dissipative structures formed on the welded joint surface at $B > 1$: *a* — region *III* (×70); *b* — *IV* (×200) (see Figure 1)

A rather high deformation rate is achieved in the joint formation zone — approximately $\dot{\varepsilon} = v_c/\delta_{c.j}$ (region *I*) and $\dot{\varepsilon} = v_c/(\delta_{c.j} + 2a)$ (region *II*). In the typical EW technological modes $\dot{\varepsilon}$ values may be higher than $1 \cdot 10^8$ s^{-1}. At such a deformation rate $\dot{\varepsilon}$ viscous resistance μ_{ef} reaches the proof stress already at the values of about a hundred pascals per second, which is by an order of magnitude lower than those measured in [11] at $\dot{\varepsilon} = 1 \cdot 10^5$ s^{-1}.

Thus, metal flow in the joint formation zone regions *I* and *II* occurs at stresses tending to σ_{pr} and low values of effective viscosity μ_{ef}. Dissipative structures implemented in regions *III* and *IV* are visually similar to the flow of an ideal non-viscous liquid [13]. It is probable that in the above regions deformation of the joint formation zone proceeds at limit stresses σ_{pr}, as well as at $\mu_{ef} \to 0$ and $\mu_{dif} = 0$. (A more definite statement cannot be made, as in the region of considerable deformations the hydrodynamic nature of the flow can be due to heating up to high temperatures.)

The above reasoning provides the simplest physical substantiation for classification of dissipative structures, developing in the joint formation zone, by the value of just one dimensionless parameter *B*. The actual diversity of the observed dissipative structures [14] is somewhat more complicated than the one considered in this paper. This means that the process of dissipative structure formation depends not only on *B* parameter. Existence of a certain dependence on other parameters is also probable, which can make more complicated the simplified presentation of the boundaries of WW regions in Figure 1 by straight lines B_i = const. This is further confirmed by detection

of a special region of «anomalous waves» V in the upper part of region I [14]. (V region falls out of the above consideration, as the condition of smallness of angles γ is not satisfied in it, and consideration of the processes in the joint formation zone separate from the plate bulk is not justified.) Therefore, the proposed division of WW should be regarded as the first approximation to a physically sunstantiated classification of dissipative structures in EW.

CONCLSUIONS

1. Removal of kinetic energy from the joint formation zone required for formation of a strong welded joint can proceed either by dissipation into heat through a stationary plastic deformation of the surface layers of the metal, or by formation of periodical dissipative structures. Development of the latter leads to intensification of plastic deformation of the joint formation zone or generation of shock waves, removing the energy beyond the joint formation zone.

2. A sequence of dissipative structures exists within the weldability region, which cover up the gap between the region of non-elastic oblique collision of solids and region of hydrodynamic cumulation. Each of the dissipative structures corresponds to one of the variants of welded joint boundary shape, well-known to technologists, namely rectilinear, wavy, wavy with partial melting, sections of cumulative jets.

1. Kobelev, A.G., Lysak, V.I., Chernyshev, V.N. et al. (2002) *Manufacturing of metallic laminated composite materials.* Moscow: Intermet Engineering.
2. Deribas, A.A. (1980) *Physics of explosion strengthening and welding.* Novosibirsk: Nauka.
3. Kudinov, V.M., Koroteev, A.Ya. (1978) *Explosion welding in metallurgy.* Moscow: Metallurgiya.
4. Surov, V.S. (1988) Oblique collision of metal plates. *Fizika Goreniya i Vzryva*, 24(**6**), 115–120.
5. Bondar, M.P. (1995) Type of localisation of plastic deformation on contacts, which defines the strong joint formation. *Ibid.*, **5**, 122–128.
6. Dobrushin, L.D., Fadeenko, Yu.I., Petushkov, V.G. (2002) Special conditions for joint formation in metal welding by a shock wave. *The Paton Welding J.*, **2**, 28–32.
7. Bondar, M.P. (1998) Peculiarities of structure formation at significant high-rate deformations. *Fizich. Mezomekhanika*, 1(**1**), 37–55.
8. Bondar, M.P. (2000) Structure formation and properties of materials made by high-rate methods. *Ibid.*, 3(**6**), 75–87.
9. Bondar, M.P. (2002) Evolution of microstructure in dynamic loading of metals. *Ibid.*, 38(**2**), 125–134.
10. Stepanov, G.V. (1991) *Elastic-plastic deformation and fracture of materials at pulse loading.* Kiev: Naukova Dumka.
11. Zubov, V.I., Stepanov, G.V., Shirokov, A.V. (2003) Influence of deformation rate on yield strength of steels of different strength. *Problemy Prochnosti*, **5**, 113–121.
12. Petushkov, V.G., Kudinov, V.M., Fadeenko, Yu.I. (1993) *Explosion treatment of metal structure welded joints.* Moscow: Metallurgiya.
13. Voropaev, S.I., Smirnov, S.L., Filippov, I.A. et al. (2002) Stratified traces after «spot» pulse sources. *Izvestiya Ros. AN. Fizika Atmosfery i Okeana*, 38(**3**), 402–410.
14. Kuzmin, S.V., Lysak, V.I., Chugunov, E.A. et al. (2000) Welded joint formation in explosion welding of metals. *The Paton Welding J.*, **11**, 26–30.

PECULIARITIES OF HEAT EXCHANGE BETWEEN IONISED GAS AND EVAPORATING PARTICLE IN PLASMA SPRAYING

Yu.S. BORISOV, A.S. ZATSERKOVNY and **I.V. KRIVTSUN**
E.O. Paton Electric Welding Institute, NASU, Kiev, Ukraine

Procedure is suggested for calculation of plasma ion and electron energy flows onto the surface of a dispersed material particle in the atmospheric-pressure inert-gas plasma, as well as energy losses for evaporation of the particle material.

Keywords: *plasma spraying, particle, plasma, heat flow, Knudsen layer, evaporation*

Many procedures and models are available now for calculation of heat flow about a particle from plasma, allowing for different mechanisms of heat exchange taking place in a system under consideration. The key mechanisms of energy exchange occurring between a flow of the atmospheric-pressure isothermal plasma and a dispersed material particle under plasma spraying conditions are described in [1]. This study also suggests an expression for determination of energy balance on the surface of a spherical particle located in a flow of the atomic gas plasma:

$$-\left(\chi_m \frac{\partial T_m}{\partial r}\right)\Big|_{r=a} = Q_c + Q_r + Q_i + Q_e - Q_v, \qquad (1)$$

where χ_m is the coefficient of thermal conductivity of the particle material; a is the particle radius; $T_m(r)$ is the temperature field in the particle; Q_c is the convective-conductive heat flow from plasma into the particle; Q_r is the resultant flow of the heat radiation energy; Q_i and Q_e are the flows of the energy transferred to the particle surface by plasma ions and electrons, respectively; e is the electron charge; and Q_v is the flow of the evaporation energy carried away from the particle surface by an expanding gas jet. Study [1] gives a detailed analysis of the convective-conductive and radiation components of heat exchange

in the system considered. It shows, in particular, that for an aluminium particle flown about by the atmospheric-pressure argon plasma at a temperature of the non-disturbed plasma flow equal to $T_p > 8000$ K, the value of Q_r makes a more substantial contribution to energy balance of the particle surface than its convective-conductive component Q_c.

The present study is dedicated to investigation of the rest of the components of energy balance (1) in a case of a particle in the inert gas plasma flow, assuming that radius of the particle is much larger than the characteristic length of free path $\bar{\lambda}$ of the surrounding plasma particles. Along with a radiation heat exchange at a high temperature and, therefore, high degree of ionisation of the plasma flow, also electron and ion components of the plasma may play an important role in energy balance on the particle surface. This is associated with the fact that, in addition to the energy of thermal motion that is allowed for in the calculation of Q_c, electrons reaching the particle surface transfer to it the energy of their directed motion, while ions transfer both kinetic energy they acquire in the electric field formed near the particle surface and internal energy released in their surface recombination [2]. It should be emphasised here that, due to evaporation of the particle material at the values of its surface temperature T_{ms} close to boiling point T_b, the sub-surface plasma may become a multi-component one, containing atoms and ions of the evaporated material, in addition to the plasma gas particles.

To describe these processes and analyse heat flows Q_i and Q_e, we will use a method set out in detail in study [3]. According to this method, plasma that surrounds a particle is conditionally subdivided into several zones (Figure 1). The first zone that immediately adjoins the particle surface is the space charge zone. The condition of plasma quasi-neutrality is violated and the major drop of potential between plasma and particle takes place in this zone. This layer can be regarded as the no-collision one, as under conditions considered in this study its thickness, commensurable with Debye radius $r_D \leq 1 \cdot 10^{-1}$ μm [3], is much smaller than the characteristic length of free path of the plasma particles, i.e. $\bar{\lambda} \leq 10$ μm (estimates are given for the atmospheric-pressure argon plasma at a temperature of 10,000 K).

The second zone is the ionisation zone of the non-isothermal quasi-neutral plasma, or pre-layer, where the charged particles are generated due to ionisation of gas atoms desorbed from the particle surface and evaporating atoms of the particle material by plasma electrons. Ions formed here are accelerated towards the particle surface by the electric field formed by more mobile electrons, and are recombined near the said surface. Therefore, conditions of local ionisation equilibrium of plasma are violated within this zone. In addition, here we can see a considerable change in plasma potential, which may be commensurable with the potential drop in the space charge layer [3].

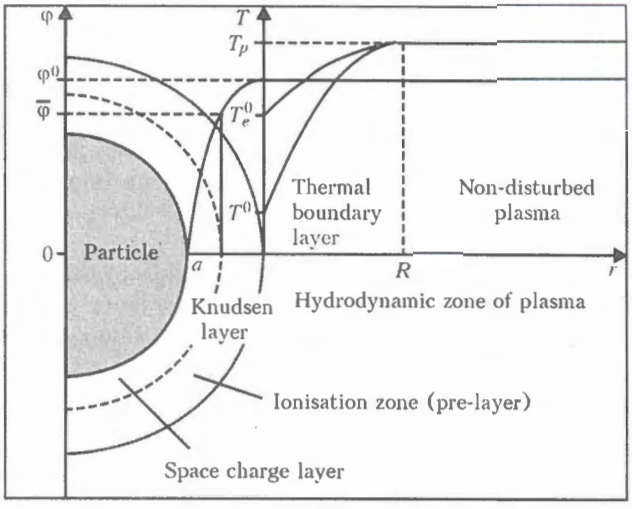

Figure 1. Structure of sub-surface plasma, distribution of potential and temperature of plasma electrons and heavy particles (see designations in the text)

Boundary of the Knudsen layer lies at a distance from the particle surface equal to several lengths of the free path of the plasma particles (see Figure 1). The hydrodynamic flow region, where the local thermodynamic equilibrium is set both at the translational and internal degrees of freedom of the plasma particles, begins behind this boundary. As it is assumed that thickness of the Knudsen layer is smaller than radius of a sprayed particle, further on we will consider this layer, and particularly the space charge layer, to be flat.

With the procedure described, plasma consists actually of two basic regions, i.e. non-equilibrium (Knudsen layer) and equilibrium (hydrodynamic flow region), for which the first region acts as a discontinuity surface [3]. It should be noted that the hydrodynamic region of plasma, as well as the Knudsen layer, can be conditionally subdivided into two zones (see Figure 1), i.e. thermal boundary layer, within which we see levelling of the temperature of electrons, T_e, and heavy particles, T, with the temperature of the non-disturbed plasma flow, T_p, and zone of the non-disturbed plasma.

To calculate the values of Q_e and Q_i that are components of energy balance (1), it is necessary to determine the electron and ion energy flows onto the particle surface, provided that the total electric current density between the plasma and this surface is equal to zero, as a particle has the «floating» potential. Supposing that the current in the Knudsen layer is transferred only by electrons and ions coming to the particle surface from plasma (it is assumed that all ions that get to the surface are recombined there and come back to plasma in the form of atoms, and that there are no flows of electrons emitted by the particle material, or electrons reflected from the particle surface), this condition can be written down as follows:

$$j_e - \sum_{\alpha = g,\, m} j_{i\alpha} = 0, \qquad (2)$$

where j_e is the density of the current of plasma electrons reaching the particle surface; $j_{i\alpha} = e\bar{n}_{i\alpha}\bar{V}_{i\alpha}$ is the density of the current of the grade α ions ($\alpha = g$ corresponds to plasma gas ions, and $\alpha = m$ corresponds to particle material ions); and $\bar{n}_{i\alpha}$ and $\bar{V}_{i\alpha}$ are the concentration and velocity of ions at the boundary between the pre-layer and no-collision layer of the space charge, respectively.

For the given conditions, distribution of the concentration of electrons in the Knudsen layer can be considered to be the Boltzmann one with temperature T_e^0, which is constant through the layer thickness [3]. In addition, as the potential of plasma is higher than that of the particle surface, electrons are decelerated by the electric field near the said surface. In this case the density of the current of electrons reaching the particle surface can be calculated using the following known relationship:

$$j_e = \frac{1}{4} en_e^0 v_{T_e}^0 \exp\left(-\frac{e\varphi^0}{kT_e^0}\right), \quad (3)$$

where n_e^0 and $v_{T_e}^0 = \sqrt{8kT_e^0/\pi m_e}$ are the concentration and thermal velocity of electrons at the external boundary of the Knudsen layer, respectively; k is the Boltzmann constant; $\varphi^0 > 0$ is the potential of plasma with respect to the particle surface (see Figure 1); and m_e is the mass of an electron.

To calculate values of the ion currents flowing onto the particle surface, it is necessary to study processes occurring in the ionisation region. For this purpose, we will use an approach suggested in study [4]. This approach is based on an assumption that ions in the plasma pre-layer are intensively maxwellised and acquire a common velocity of a directed motion, the value of which at the boundary between the ionisation region and space charge region can be determined using the following expression [3]:

$$\bar{V}_{i\alpha} = \bar{V}_i = \sqrt{kT_e^0 \frac{\sum\limits_{\alpha=g,m}(1 + T^0/T_e^0)n_{i\alpha}^0}{\sum\limits_{\alpha=g,m} M_\alpha n_{i\alpha}^0}}. \quad (4)$$

Here $n_{i\alpha}^0$ is the concentration of plasma ions at the external boundary of the Knudsen layer (for all grades of ions); M_α is the mass of a corresponding ion (atom); and T^0 is the temperature of heavy plasma particles, which is assumed to be constant within the pre-layer. With this approach, the concentration of the charged particles at the external boundary of the space charge layer (allowing for quasi-neutrality of plasma in the ionisation region) can be determined as follows [3]:

$$\bar{n}_e = n_e^0 \exp\left(-\frac{1}{2}\right); \quad \bar{n}_{i\alpha} = n_{i\alpha}^0 \exp\left(-\frac{1}{2}\right); \quad \alpha = g, m. \quad (5)$$

Then, using (4) and (5), we can write down expressions for densities of the ion currents on the particle surface in the following form:

$$j_{i\alpha} = en_{i\alpha}^0 \exp\left(-\frac{1}{2}\right)\bar{V}_i, \quad \alpha = g, m. \quad (6)$$

The expressions derived for $j_{i\alpha}$ differ from those used in study [2] in that they allow an account for a decrease in the concentration of ions within the pre-layer, as well as for a circumstance that the velocity of ions at its internal boundary must also satisfy the criterion of formation of the space charge layer, i.e. Bohm's criterion [5].

The electron and ion components of the electric current flowing from plasma onto the particle surface being determined, we can find the potential of plasma relative to this surface. Substituting (3) and (6) to (2) and allowing for the quasi-neutrality of plasma at the external boundary of the Knudsen layer yield:

$$\varphi^0 = \bar{\varphi} + \frac{1}{2}\frac{kT_e^0}{e},$$

where

$$\bar{\varphi} = \frac{kT_e^0}{e} \ln \sqrt{\frac{\sum\limits_{\alpha=g,m} M_\alpha n_{i\alpha}^0}{2\pi m_e \sum\limits_{\alpha=g,m}(1 + T^0/T_e^0)n_{i\alpha}^0}}$$

is the value of the potential at a boundary between the ionisation region and space charge layer (see Figure 1).

To calculate the values of j_e and $j_{i\alpha}$, it is necessary to know temperatures T_e^0 and T^0, as well as concentrations n_e^0 and $n_{i\alpha}^0$, for the charged particles of plasma at a boundary between the Knudsen layer and thermal boundary layer. As it is assumed that plasma in the hydrodynamic region is the ionisation-equilibrium one and may contain particles of an evaporated material, in addition to the plasma gas atoms and ions, the composition of such a multi-component plasma can be determined using the following system of equations [3]:

Saha equation

$$\frac{n_e^0 n_{i\alpha}^0}{n_{n\alpha}^0} = \left(\frac{m_e kT_e^0}{2\pi\hbar^2}\right)^{3/2} \frac{2\theta_{i\alpha}}{\theta_{n\alpha}} \exp\left[-\frac{e(U_\alpha - \Delta U)}{kT_e^0}\right], \quad \alpha = g, m, \quad (7)$$

where $n_{n\alpha}^0$ is the concentration of the grade α atoms; $\theta_{n\alpha}$ and $\theta_{i\alpha}$ are the statistical sums of the grade α atoms and ions; U_α is the corresponding value of the ionisation potentials; and $\Delta U = 2e/r_D$ is the decrease in the ionisation potentials caused by interaction of the charged particles in plasma;

plasma quasi-neutrality condition:

$$n_e^0 = \sum_{\alpha=g,m} n_{i\alpha}^0; \quad (8)$$

and Dalton law:

$$p = n_e^0 kT_e^0 + \sum_{\alpha = g,\ m} (n_{n\alpha}^0 + n_{i\alpha}^0) kT^0, \qquad (9)$$

where p is the gas-static plasma pressure (allowing for the electron pressure). In a diffusion mode of evaporation of the particle material, this value can be assumed to be equal to external (atmospheric) pressure p^0. To close the system of equations (7)–(9), it is necessary to have one more condition that determines the concentration of vapour particles present in the sub-surface plasma. Assuming that vapour has a low diffusion rate, i.e. the state of the vapour is close to saturation, equality of the partial pressure of heavy particles of the evaporated material at the external boundary of the Knudsen layer to pressure of the saturated vapour, p_s, over the particle surface with temperature T_{ms} can be taken as such a condition:

$$(n_{nm}^0 + n_{im}^0) kT^0 = p_s \equiv p^0 \left(\frac{T_b}{T_{ms}}\right)^{1/2} \times \exp\left[\frac{\lambda_v}{k}\left(\frac{1}{T_b} - \frac{1}{T_{ms}}\right)\right], \qquad (10)$$

where λ_v is the work function of atom of the particle material, assuming that $T^0 = T_{ms}$.

The value of electron temperature T_e^0 at the Knudsen layer boundary can be found by simultaneously solving the equation of energy balance of the electron component of plasma in the thermal boundary layer:

$$\frac{1}{r^2}\frac{\partial}{\partial r}\left(r^2 \chi_e \frac{\partial T_e}{\partial r}\right) - \beta(T_e - T) = 0 \qquad (11)$$

and the respective equation for temperature of heavy particles

$$\frac{1}{r^2}\frac{\partial}{\partial r}\left(r^2 \overline{\chi} \frac{\partial T}{\partial r}\right) + \beta(T_e - T) = 0. \qquad (12)$$

Here χ_e is the coefficient of electronic thermal conductivity; $\overline{\chi}$ is the coefficient of thermal conductivity of heavy particles (atoms and ions); and β is the coefficient of energy exchange between electrons and a heavy component of plasma [6], in the calculation of which it is assumed that the ratio of the concentration of vapour particles to the total concentration of all heavy particles of plasma within the thermal boundary layer is approximately constant and equal to its value at the boundary of the Knudsen layer, i.e. $\delta_m^0 = (n_{nm}^0 + n_{im}^0) / \sum_{\alpha = g,\ m} (n_{n\alpha}^0 + n_{i\alpha}^0)$. Another approximation used when writing down equations (11) and (12) is ignoring of the convective energy transfer, which, as evidenced by further numerical analysis, is acceptable for the velocity of the incident plasma flow relative to a particle equal to $u < 250$ m/s.

Allowing for the earlier assumption that thickness of the Knudsen layer is small compared with radius of a sprayed particle, we will solve the above equations for a region of $\alpha \le r \le R$, where R is the external radius of the thermal boundary layer (see Figure 1). The edge conditions at the boundary of the said layer with the Knudsen layer can be set as follows:

$$\left(\chi_e \frac{\partial T_e}{\partial r}\right)\Big|_{r=a} = j_e\left(\varphi^0 + \frac{2kT_e^0}{e}\right) + \sum_{\alpha = g,\ m} j_{i\alpha}\left(\frac{2kT_e^0}{2e} + U_\alpha\right); \quad T\big|_{r=a} = T_{ms}. \qquad (13)$$

The first condition (13) is an energy balance in the ionisation region of plasma. The term in the left part of this condition describes the energy transferred into this region by plasma electrons. The first term in the right part describes the energy transferred by electrons to the particle surface, and the second term describes the energy consumed for ionisation and acceleration of ions within the ionisation region.

Conditions of equality of the temperature of electrons and heavy particles to that of the non-disturbed flow are taken as boundary conditions at $r = R$:

$$T_e\big|_{r=R} = T\big|_{r=R} = T_p, \qquad (14)$$

while the value of R is selected to meet conditions of smooth conjugation:

$$\frac{\partial T_e}{\partial r}\Big|_{r=R};\ \frac{\partial T}{\partial r}\Big|_{r=R} < \varepsilon,$$

where ε is some low value. The calculations show that these conditions are well met at $R \ge 250$ μm over the entire range of the T_p and T_{ms} values considered for a particle with radius $a = 30$ μm present in the atmospheric-pressure argon plasma.

Figure 2 shows the distributions of temperatures T_e and T through thickness of the thermal boundary layer surrounding an aluminium particle with a radius of 30 μm (T_{ms} = 1800 K) placed in the argon plasma (T_p = 12,000 K), which were obtained from numerical solutions of boundary value problems (11)–(14) (the required temperature dependencies of χ_e, $\overline{\chi}$ and β were calculated using the procedure described in [7]).

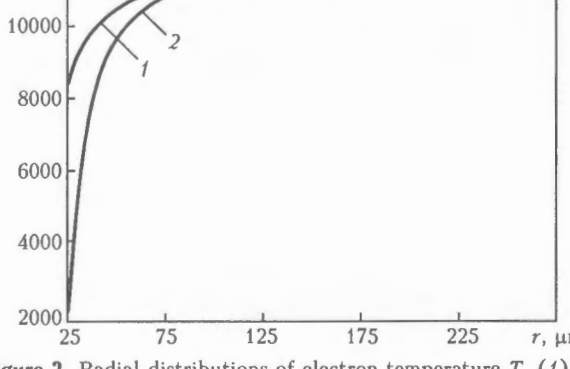

Figure 2. Radial distributions of electron temperature T_e (*1*) and temperature of the heavy component of plasma T (*2*) within the thermal boundary layer

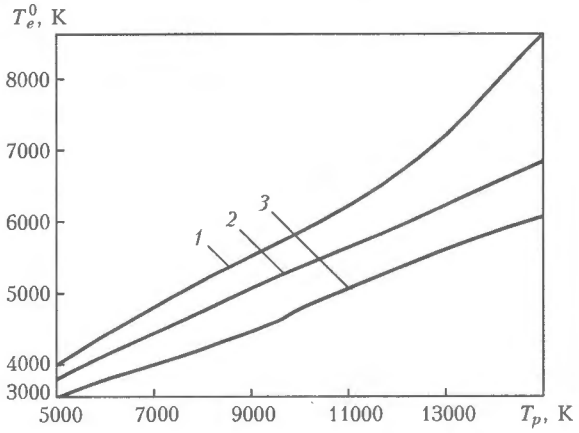

Figure 3. Dependence of electron temperature at the external boundary of the Knudsen layer upon the temperature of the non-disturbed argon plasma at different values of temperature of the surface of an aluminium particle with a radius of 30 μm: *1* — T_{ms} = = 2000 K (δ_m^0 = 0.009); *2* — 2200 K (0.047); *3* — 2500 K (0.325)

As follows from the data shown in the Figure, the temperature of electrons at the external boundary of the Knudsen layer, T_e^0, is much lower than the temperature of the non-disturbed plasma, and amounts to approximately 8000 K at the selected values of the parameters. At the given value of T_{ms}, plasma near the surface contains almost no particle material atoms or ions ($\delta_m^0 \cong 0.001$), i.e. in fact it is a single-component plasma.

Figure 3 shows dependence of the calculated values of T_e^0 upon T_p at different values of the particle surface temperature. The calculation results are indicative of a substantial effect of the multi-component nature of the sub-surface plasma, which is associated with the presence in it of the metal vapour atoms characterised by an easier ionisation (the ionisation potential of argon and aluminium is 15.76 and 5.98 eV, respectively) on the electron temperature and degree of ionisation of such a plasma. For example, increase in particle surface temperature T_{ms} and a corresponding increase, according to (10), in the concentration of vapour particles in the surrounding plasma are accompanied by an increasingly pronounced decrease in the electron temperature at the Knudsen layer boundary, compared with the corresponding value of T_p (see Figure 3), whereas the value of n_e^0, on the contrary, grows. In addition, increase in δ_m^0 leads to some decrease in plasma potential φ^0 relative to the plasma surface from 2.79 (at T_{ms} = 2000 K) to 2.21 V (at T_{ms} = 2500 K). In both cases T_p = 12,000 K.

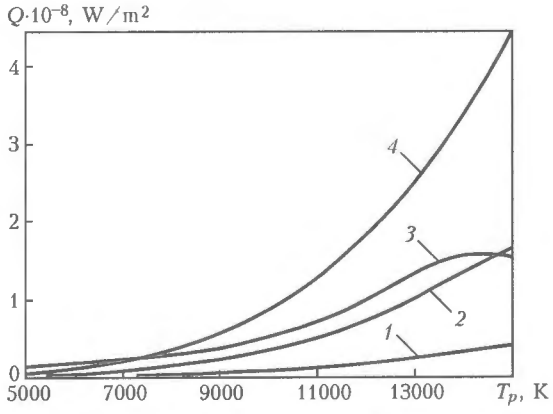

Figure 4. Dependence of components Q of the plasma flow onto the particle surface upon the non-disturbed argon plasma temperature T_p: *1* — Q_e; 2 — Q_i; *3* — Q_c (at u = 100 m/s); *4* — Q_r

Parameters of plasma at the external boundary of the Knudsen layer required to calculate the electron and ion currents onto the particle surface being thus determined, it is possible to find the corresponding energy flows Q_e and Q_i. In particular, the flow of the energy transferred by plasma electrons that are capable of overcoming a potential barrier of φ^0 can be described as $j_e(\varphi^0 + 2kT_e^0/e)$ (this expression differs from that used in [2] in the presence of term $j_e\varphi^0$, which can substantially contribute to the heat flow). As the energy of the thermal (chaotic) motion was taken into account in the calculation of Q_c, the expression for Q_e can be written down as follows:

$$Q_e = j_e(\varphi^0 + \varphi_m), \tag{15}$$

where φ_m is the work function of electrons for a given particle material. It is assumed in (15) that all the electrons that reached the particle surface are absorbed by the particle material (releasing the work function), and that the coefficient of accommodation of the kinetic energy of electrons by this surface is equal to one.

Then, taking into account the energy of a directed motion of ions they acquire in the space charge layer, the following can be written down for Q_i:

$$Q_i = \sum_{\alpha = g,\, m} j_{i\alpha}(\overline{\varphi} + U_\alpha - \varphi_m). \tag{16}$$

It is assumed in equation (16) that the coefficient of accommodation of the energy of ions by the particle surface is also equal to one.

Figure 4 shows dependence of heat energy flows Q_i and Q_e onto the surface of an aluminium particle (a = 30 μm and T_{ms} = 2000 K) upon the temperature of the non-disturbed plasma (atmospheric-pressure argon plasma) flow. To compare, the Figure also shows the curves for Q_c calculated using the criterial formula [8] that yields the best agreement with the experimental data for a case of the argon plasma flowing about a particle, as well as the curves for Q_r calculated using the procedure described in [1]. As seen from the calculation curves shown in Figure 4, at high values of the plasma temperature (T_p > 10,000 K) the ion and electron components of the heat flow may substantially contribute to the total heat flow from plasma to the particle surface.

The effect of the multi-component nature of the sub-surface plasma caused by the evaporated material atoms and ions present in it on the considered components of the heat flow is shown in Figure 5. The Figure also shows the curves for $Q_i(T_p)$ and $Q_e(T_p)$ at different values of the particle surface temperature. Curves *2* and *4* in this Figure correspond to the ion and electron heat flows calculated at T_{ms} = 1800 K.

In this case the sub-surface plasma contains a negligibly small ($\delta_m^0 \cong 0.001$) quantity of metal (aluminium) particles, and the said flows are formed mostly due to the charged particles of plasma gas (argon). At T_{ms} = 2400 K the vapour content of the sub-surface plasma is much higher ($\delta_m^0 = 0.180$), i.e. the plasma becomes a much more multi-component, which at $T_p > 10{,}000$ K leads to the higher values of heat flows Q_i and Q_e (compare curves *1–4* in Figure 5). This is associated with the fact that, despite a corresponding decrease in T_e^0 relative to T_p (see Figures 2 and 3), increase in the content of easily ionised metal atoms in plasma with growth of T_{ms} leads to increase in the concentration of the charged particles, which determine, according to (3), (6), (15) and (16), the said heat flows.

If temperature of the particle surface is higher than the boiling point of the particle material (pressure of the saturated vapour becomes higher than the atmospheric one), the vapour starts expanding to press out the external gas plasma, and the diffusion mode of evaporation changes into the convective one. As a result, the sub-surface plasma again becomes the single-component one, although in this case it contains only the evaporated material particles. Composition of this plasma can be calculated using equations (7)–(9), assuming in them that $n_{ng} = n_{ig} = 0$ and supplementing this system of equations with the relationships that determine the concentration and temperature of heavy particles of the expanding vapour near the particle surface. For the convective mode of evaporation, we will use expressions derived in study [9] to find $n_{nm}^0 + n_{im}^0$ and T^0 for a case of surface evaporation into a medium with the back pressure:

$$\frac{n_{nm}^0 + n_{im}^0}{n_{ms}} = \left\{\left(\gamma_m^2 + \frac{1}{2}\right)\exp(\gamma_m^2)[1 - \Phi(\gamma_m)] - \frac{\gamma_m}{\sqrt{\pi}}\right\} \times$$

$$\times \sqrt{\frac{T_{ms}}{T^0}} + \frac{1}{2}\left\{1 - \gamma_m\sqrt{\pi}\exp(\gamma_m^2)\,[1 - \Phi(\gamma_m)]\right\}\frac{T_{ms}}{T^0}; \quad (17)$$

$$\frac{T^0}{T_{ms}} = 1 + \frac{\gamma_m^2\pi}{32}\left(1 - \sqrt{1 + \frac{64}{\gamma_m^2\pi}}\right).$$

Here $n_{ms} = p_s/kT_{ms}$ is the concentration of the saturated vapour corresponding to a given temperature of the particle surface:

$$\gamma_m = v^0\left(\frac{M_m}{2kT^0}\right)^{1/2},$$

where v^0 is the velocity of scatter of the ionised vapour at the external boundary of the Knudsen layer; M_m is the mass of a metal atom; and $\Phi(x) = \frac{2}{\sqrt{\pi}}\int_0^x \exp(-\xi^2)d\xi$ is the probability integral. It should be noted that v^0 is an external parameter, and it is determined by the conditions of vapour expansion in the hydrodynamic region. In addition, according to [9], this value should satisfy the condition of M ≤ ≤ 1, where M = v^0/s^0 is the Mach number and $s^0 = \sqrt{5kT^0/3M_m}$ is the local velocity of sound. For numerical estimation of v^0, we will consider approximately that in a case of a low value of the Mach number the ionised vapour expansion occurs under the conditions where the pressure at a boundary between the Knudsen layer and thermal boundary layer is constant and equal to the external pressure, i.e. at $n_e^0 kT_e^0 + (n_{nm}^0 + n_{im}^0)kT^0 = p^0$, where dependence of the $n_{nm}^0 + n_{im}^0$ and T^0 values upon dimensionless velocity γ^m is determined by relationships (17).

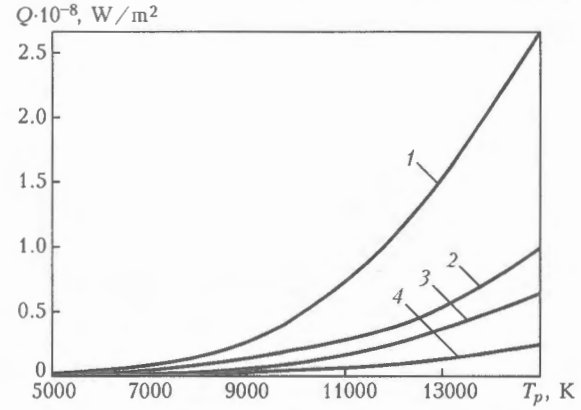

Figure 5. Dependence of energy flows of ions (*1*, *2*) and electrons (*3*, *4*) onto the surface of an aluminium particle with a radius of 30 μm upon the non-disturbed plasma temperature T_p: *1*, *3* — T_{ms} = = 2400 K ($\delta_m^0 = 0.180$); *2*, *4* — 1800 K ($\delta_m^0 = 0.001$)

The temperature of electrons in (7) and (9) can be determined by solving the equations of energy balance between electrons and a heavy component of plasma within the thermal boundary layer, allowing for convective cooling of the sub-surface plasma by a vapour flow:

$$\frac{1}{r^2}\frac{\partial}{\partial r}\left(r^2 n_e\left[\frac{5}{2}kT_e + eU_m\right]v\right) = \frac{1}{r^2}\frac{\partial}{\partial r}\left(r^2\chi_e\frac{\partial T_e}{\partial r}\right) - \beta(T_e - T);$$

$$\frac{5}{2}k\,(n_{nm} + n_{im})\,v\,\frac{\partial T}{\partial r} = \frac{1}{r^2}\frac{\partial}{\partial r}\left(r^2\overline{\chi}\,\frac{\partial T}{\partial r}\right) + \beta(T_e - T), \quad (18)$$

where the velocity of scatter and total concentration of heavy particles of the vapour are related through the continuity equation, which yields $(n_{nm} + n_{im})v = \frac{(n_{nm}^0 + n_{im}^0)v^0a^2}{r^2}$. The edge conditions for equations (18) at the external boundary of the thermal boundary layer (at $r = R$) persist in the form of (14), whereas those at a boundary between this layer and Knudsen layer change to some extent compared with (13):

$$\left(\chi_e\frac{\partial T_e}{\partial r}\right)\Big|_{r=a} = j_e\left(\varphi^0 + \frac{2kT_e^0}{e}\right) + j_{im}\left(\frac{2kT_e^0}{e} + U_m\right) +$$

$$+ n_e^0\left(\frac{5}{2}kT_e^0 + eU_m\right)v^0; \quad T\big|_{r=a} = T^0.$$

Here the first condition describing the energy balance in the ionisation region of plasma allows for the energy transferred from this region by the electron component of the ionised vapour during its expansion.

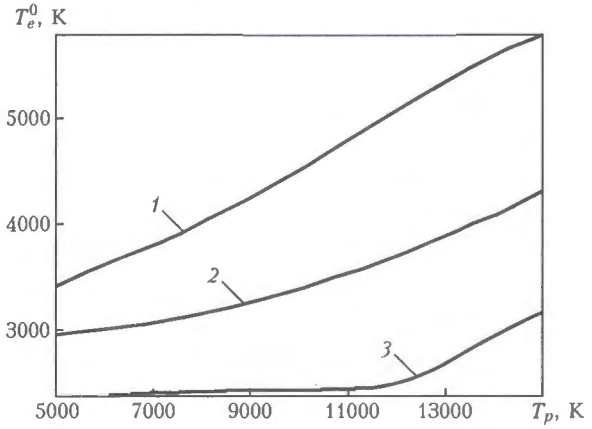

Figure 6. Dependence of electron temperature at the external boundary of the Knudsen layer upon the temperature of the non-disturbed argon plasma at different values of the surface temperature of an aluminium particle with a radius of 30 μm: *1* — T_{ms} = = 2700 K (diffusion mode of evaporation of the particle material); *2* — 2750 K (M = 0.09); *3* — 2800 K (M = 0.26)

Numerical solution of equations (18) for an aluminium particle in the argon plasma jet shows that the resultant values of the electron temperature at a boundary of the Knudsen layer in the convective mode of evaporation of the particle material are much lower than in the diffusion mode (compare curves *1–3* in Figure 6), which is attributable to cooling of plasma by the flow of the expanding vapour. As a result, ionisation of the sub-surface plasma decreases to such an extent that heat flows Q_i and Q_e, which are proportional to the concentration of the charged particles at the Knudsen layer boundary, become negligibly small. Besides, in the convective mode of evaporation (due to an intensive transfer of the heat energy of plasma from the boundary layer by the vapour flow), convective-conductive heat flow Q_c must also decrease. Instead, it is an evaporative cooling of the particle surface that starts playing a substantial role in energy balance of the particle. The concentration of heavy particles of the vapour and velocity of its scatter at the external boundary of the Knudsen layer being known, it is possible to calculate the energy transferred from a unit surface of the particle by the vapour flow. Ignoring the thermal energy of the vapour particles, compared with the evaporation energy, the following expression [10] can be used to calculate the value of Q_v:

$$Q_v = (n_{nm}^0 + n_{im}^0)v^0\lambda_v. \qquad (19)$$

It should be noted here that, as the concentrations of ions at the external boundary of the Knudsen layer are negligibly low in the vapour expansion mode, the value of n_{im}^0 in expression (19) can be assumed to be equal to zero.

Figure 7 shows the results of the calculations of heat flow Q_v for an aluminium particle with a radius of 30 μm, located in a flow of the atmospheric-pressure argon plasma and having a surface temperature of T_{ms} = 2800 K (T_b = 2720 K) (as the said heat flow describes the energy loss of a particle, it was taken with a minus sign). The Figure also shows the corresponding curves for $Q_r(T_p)$ and curve for the resultant heat flow through the particle surface. As follows from the Figure, T_p has almost no effect on the value of Q_v (curve *2* in Figure 7), which, as noted above, is associated with a substantial decrease in the degree of ionisation of the sub-surface plasma due to its cooling by a flow of the expanding vapour. On the contrary, the value of Q_r markedly grows with increase in T_p (curve *1*), which leads to a change in sign of the resultant heat flow (curve *3*). As a result, the given particle is cooled at T_p < 12,500 K and heated at higher values of the surrounding plasma temperature.

Figure 8 shows the calculated dependence of all components and total heat flow onto the surface of an aluminium particle in argon plasma upon T_{ms}. The data shown in this Figure allow analysis of the contribution of each component of heat exchange for the system under consideration to the total energy balance on the surface of a particle having a temperature close to the boiling point of its material. In addition, they are indicative of a decisive role of evaporation cooling of the particle at $T_{ms} > T_b$.

In general, the developed mathematical model allows numerical analysis of both individual components of heat balance of the surface of a sprayed particle and resultant thermal effect of the plasma jet on the dispersed material particle over a wide range of values

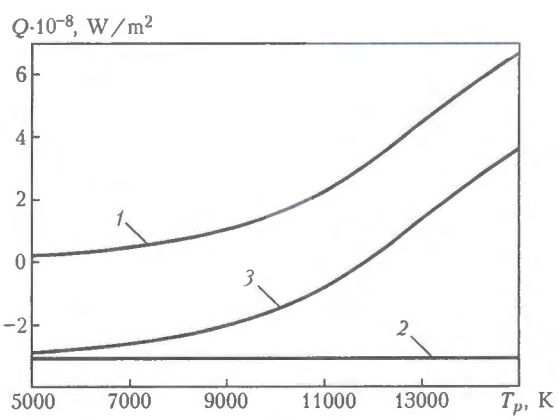

Figure 7. Resultant heat flow (*3*) and its components Q_r (*1*) and Q_v (*2*) in the convective mode of evaporation of particle material

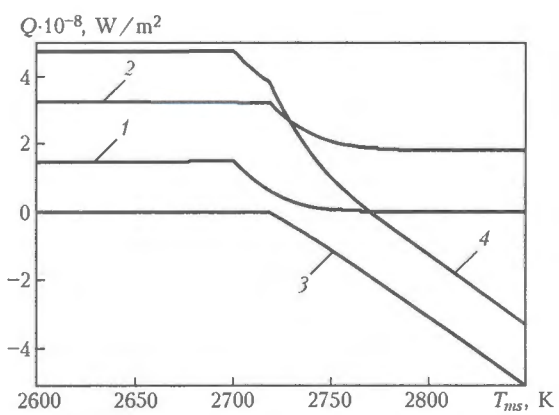

Figure 8. Dependence of the total heat flow through the surface of an aluminium particle (a = 30 μm) in argon plasma flow (T_p = = 12,000 K, u = 300 m/s) and its components upon T_{ms}: *1* — Q_i + + Q_e; *2* — $Q_c + Q_r$; *3* — Q_v; *4* — resultant heat flow

of temperature of plasma and surface of the particle, as well as their relative velocities characteristic of the conditions of sub-sonic plasma spraying.

CONCLUSIONS

1. Allowance for the multi-component nature of the sub-surface plasma caused by the evaporated particle material atoms and ions present in it, decrease in the electron temperature at the Knudsen layer boundary relative to the temperature of the non-disturbed plasma, as well as other factors determining the said heat flows, makes it possible to conduct an in-depth analysis of heating of the particle moving in a low-temperature plasma jet in a case of evaporation of the particle material.

2. As shown by the conducted numerical analysis, at high temperatures of the plasma jet the energy flows of the electron and ion components of plasma may play a marked role in the total energy balance of the sprayed particle. For example, when an aluminium particle is flown about by the atmospheric-pressure argon plasma having a temperature higher than 10,000 K, the above flows constitute 20–50 % of the corresponding value of the convective-conductive heat flow onto the particle surface, and they should be taken into account in analysis of heating of particles under the conditions considered.

3. The energy flows of plasma ions and electrons onto the particle surface greatly depend upon the temperature of this surface, which is attributable to the multi-component nature of the sub-surface plasma caused by the evaporated particle material atoms and ions. In particular, at temperature of the surface of an aluminium particle equal to 2500 K these flows are almost twice as high as the corresponding values for the particle having a surface temperature of 1800 K.

4. If temperature of the surface of a sprayed particle is higher than the boiling point of its material, the decisive factor in energy balance of the particle is evaporation cooling associated with carrying away of the evaporation energy of its material atoms by a flow of the expanding vapour. For example, as shown by the calculations, in a case of an aluminium particle placed in the argon plasma having a temperature of 12,000 K, the resultant heat flow onto the particle surface becomes equal to zero at a temperature of its surface equal to 2770 K, and heating of the particle changes into cooling with further increase of this temperature.

1. Borisov, Yu.S., Zatserkovny, A.S., Krivtsun, I.V. (2005) Convective-conductive and radiation heat exchange of plasma flow with disperse material particles under plasma spraying conditions. *The Paton Welding J.*, **6**, 6–10.
2. Shimanovich, V.D., Smyaglikov, I.P., Zolotovsky, A.I. (2003) An effect of near-cathode region plasma of an argon arc on metal particles. In: *Progress in Plasma Processing of Materials: Proc. of 7th European Conf. on Thermal Plasma Processes* (France, Strasbourg, June 18–21, 2003). New York: Begell Hause Inc.
3. Krivtsun, I.V. (2001) Model of evaporation of metal in arc, laser and laser-arc welding. *The Paton Welding J.*, **3**, 2–9.
4. Baksht, F.G., Dyuzhev, G.A., Mitrofanov, N.K. et al. (1973) Probe measurements in low-temperature dense plasma at high degrees of ionization. *Zhurnal Tekhnich. Fiziki*, 43(**12**), 2574–2583.
5. Bohm, D. (1949) *The characteristics of electrical discharges in magnetic fields*. Ed. by A. Guthrie, R.K. Wakerling. New York: McGraw-Hill.
6. Zhdanov, V.M. (1982) *Phenomena of transfer in multi-component plasma*. Moscow: Energoizdat.
7. Gvozdetsky, V.S., Demchenko, V.F., Krivtsun, I.V. et al. (1990) Modelling of transfer processes in a multi-component column of the welding arc. In: *Problems of welding and special electrometallurgy*. Kiev: Naukova Dumka.
8. Dresvin, S.V., Donskoj, A.V., Goldfarb, V.M. et al. (1972) *Physics and technique of low-temperature plasma*. Moscow: Atomizdat.
9. Knight, Ch.J. (1979) Theoretical modelling of rapid surface vaporization with back pressure. *AIAA J.*, 17(**5**), 519–523.
10. Arutyunyan, R.V., Baranov, V.Yu., Bolshov, L.A. et al. (1989) *Effect of laser radiation on materials*. Moscow: Nauka.

ON CONCEPT OF PORE INITIATION IN WELDED JOINTS UNDER LOW-TEMPERATURE CREEP

V.V. DMITRIK[1] and A.I. KONYK[2]
[1]Ukrainian Engineering-Pedagogical Academy, Kharkov, Ukraine
[2]Open Joint Stock Company «Zavod Elektromekhanicheskikh Izdelij», Kharkov, Ukraine

It has been found that initiation of pores in welded joints of heat-resistant pearlitic steels and their initial evolution under conditions of low-temperature service creep is mostly of a diffusion character, while their further development is of a dislocation character.

Keywords: *thermostable steels, welded joints, pore initiation, carbides, creep, failure, service life*

Failure of thermostable pearlite steels employed in heat power plants under conditions of low-temperature creep ($T_{op} \le 0.5T_{melt}$) is known to proceed by the mechanism of pore initiation. It is advisable to order regularities of pore initiation and development in welded joints of these steels for optimization of the resistance to the pore initiation.

To our opinion, the problem of increasing resistance to failure proceeding by the mechanism of pore formation with regard to the works [1–15] should be solved by solution of two conjugate problems:

- establishment of the dependence of pore initiation on size of the grains, their shape, orientation, the presence of carbide precipitation, stability and distribution, as well as stability of α-phase, purity by nonmetallic inclusions, physical conditions of operation and others;

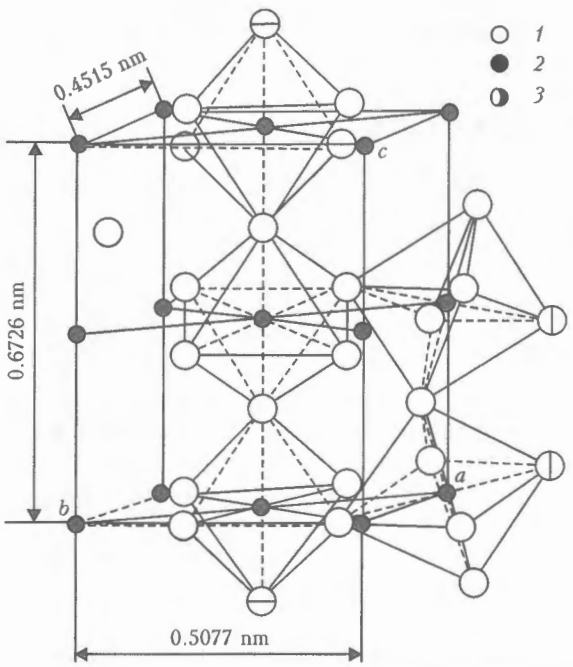

Figure 1. Elementary cell M_3C (truncated). Here and in Figure 2: *1* — iron; *2* — carbon; *3* — chromium

- optimization of regularity of increasing resistance to pore initiation and development regarding the structural factor.

It is known that micropores under creep are initially formed on the grain boundaries located perpendicular to the tensile stresses [4]. Practically confirmed statement that the reason of micropore initiation on the grain boundaries is a decrease of the energy of the boundaries themselves due to the disappearance of a part of their surface [5] requires further elaboration. Widespread assumption [4, 9] that pore formation due to condensation of vacancies is mainly specified by a plastic deformation as applied to physical conditions of operation of the studied welded joints requires, to our opinion, a clarification.

Pipes of thermostable Cr–Mo–V pearlite steels produced by centrifugal cast method may have not only segregation of elements but also local segregation in the α-phase of chromium, molybdenum, manganese and partially vanadium [8, 15, 16]. It is established that chromium content in the sites of local segregation in the α-phase may about 3–5 times exceed the average value. Grain sites enriched with chromium atoms form the Guinier–Preston type zones in the α-phase [17] that play a significant role in aging of pearlite steel, especially welded joints of steel 15Kh1M1F. Correlation of atom radii of iron (0.126 nm) and chromium (0.127 nm) affects the shape of the forming zones. It is established that intensity of carbide reactions $M_3C \rightarrow M_7C_3 \rightarrow M_{23}C_6$ depends on segregation of chromium atoms related to the availability of such zones. Carbide of cementite type $(Fe, Cr)_3C$ has orthorhombic cell (Figure 1) [18–20] where peripheral peaks may be partially filled with chromium atoms (steel 15Kh1M1F) with a higher level of energy than iron atoms.

It is appropriate to establish a correlation between structure of the carbides M_3C and $M_{23}C_6$ (Figure 2) [19]. As applied to steel 15Kh1M1F only 8 out of 92 chromium atoms located in the center of every eighth cube of the elementary cell of complex carbide $M_{23}C_6$ may be substituted by molybdenum atoms.

Due to larger sizes of the chromium atoms as compared to iron atoms a free site in the center of every eighth cell $M_{23}C_6$ will increase depending on the re-

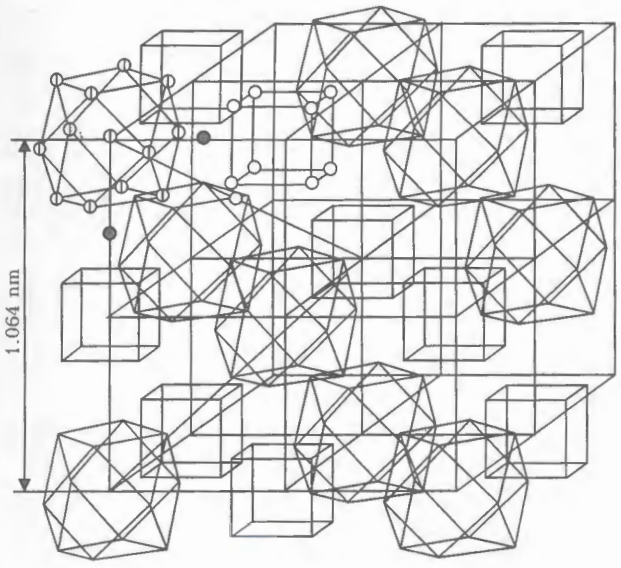

Figure 2. Elementary cell $M_{23}C_6$

placement of chromium atoms with iron atoms, which is related to a simultaneous decrease of the stability of the cell itself. The presence of molybdenum atoms (atomic radius is 0.139 nm) [21] located in the center of every eighth cube in $M_{23}C_6$ promotes a more intensive displacement of the chromium atoms with iron atoms, i.e. instable carbides $(Fe, Mo, Cr)_{23}C_6$ are formed, whose coagulation kinetics under conditions of creep requires investigation. As against $M_{23}C_6$ carbides Mo_2C and VC in the structure of welded joints of steel 15Kh1M1F are relatively stable up to about 300,000 h of operation. Carbides $M_{23}C_6$ (about 5–8 %) appear in the weld metal after tempering of these steels and facilitate disperse strengthening. Tempering of welded joints (730–750 °C, 3 h) leads also to some additional increase of $M_{23}C_6$ precipitates [10], about 7–9 % in the overheating site of the HAZ of the welded joints of steel 15Kh1M1F. Heating of the parent metal in welding in the temperature range A_{c_1}–A_{c_3} (site of incomplete recrystallization of the HAZ) promotes a noticeable increase of carbides $M_{23}C_6$ (10–15 %).

Under conditions of operational aging the carbide precipitates $M_{23}C_6$ coagulate not only as a result of $M_7C_3 \rightarrow M_{23}C_6$ reaction and coalescence but also as a result of «drawing» of molybdenum atoms from the alloyed α-phase. Coagulation facilitates decrease of coherence (convergence) of their crystalline cells and α-phase cells.

Condensation of vacancies including their coalescence provides formation of microdiscontinuities 0.1–0.3 μm (first stage of pore formation) while depletion of the α-phase sites with chromium and molybdenum atoms manifesting itself after 150,000 h of operation leads to a local increase of its plasticity, which is confirmed by a division of grains into subgrains with corresponding values of microhardness. It is established that after 186,000 h of operation not only boundary sites partially disappear in the α-phase but also a tendency to polygonization is observed (Figure 3), its highest intensity being observed in the

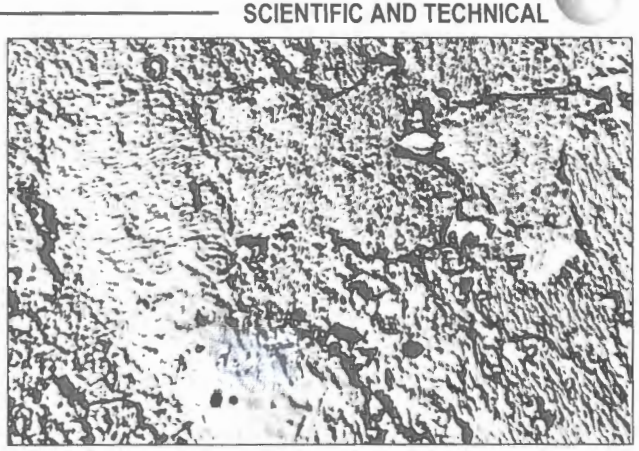

Figure 3. Polygonal structure of site of incomplete recrystallization of the HAZ (×6000)

structures of site of the incomplete phase recrystallization of the HAZ.

At the second stage of pore formation polygonal sites on the sites with the boundaries of α-phase with precipitates of $M_{23}C_6$ form more intensively than in other sites, which is typical for dislocation (mainly) mechanism of pore formation. In the work [4] it is proposed to explain the mechanisms of formation of microdiscontinuities on the basis of correlation of the inner-grain slide and slip on the grain boundaries. Slide causes appearance of the step on the grain boundary. However, the presence of carbide precipitates on the grain boundary and their role in formation of steps are not provided here.

Slip on the grain boundaries, which is facilitated by a decrease of chromium and molybdenum in α-phase is simultaneously retarded by both instable $M_{23}C_6$ and stable Mo_2C precipitates as well as by highly dispersed VC, which is controlled by a level of their uniform distribution. Slip on the grain boundaries also provides a decrease of coherence of coagulating $M_{23}C_6$ with α-phase, which in conditions of working stresses and temperatures leads to formation of microdiscontinuities, i.e. pore initiation.

Initiation and development of micropores in the welded joints of steel 15Kh1M1F is established to be dependent on sizes and orientation of grains (Figures 4–6) as well as on the presence of carbide precipitates on the grain boundaries [10] and structural

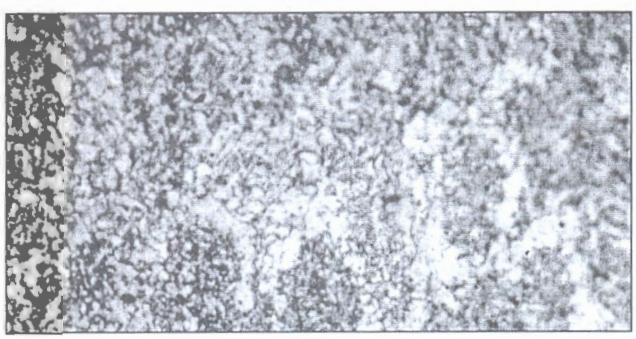

Figure 4. Microstructure of weld metal of welded joint of the live steam pipe with 25 mm wall thickness and 630 mm in diameter after 190,000 h of operating time (length of grains is L = 60–90 μm, width is h = 20–30 μm; manual arc welding under standard conditions) (×100)

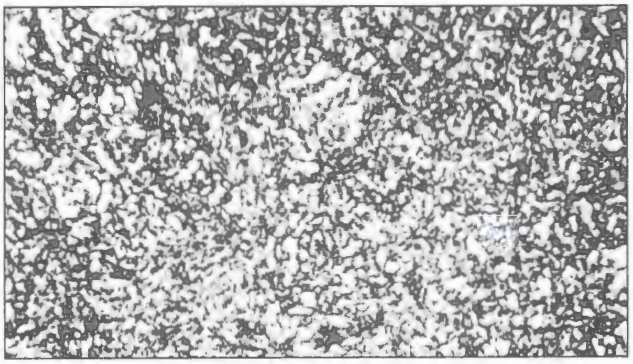

Figure 5. Microstructure of weld metal (grain index is 8–9, GOST 5639–82; average diameter is 15–20 μm; mechanized welding in CO_2 + 25 % Ar mixture under conditions indicated in [10]) (×360)

heterogeneity of welded joints themselves (Figures 7 and 8). The appearance of micropores is accompanied by an increase of plasticity of those sites of grains (subgrains), which are contiguous with their highest concentration [6, 8].

It is shown that a decrease of segregation of chromium and molybdenum atoms in the structure of α-phase of welded joints of centrifugal-cast pipes of thermostable Cr–Mo–V steels provides an increase of stability of their structure under conditions of operational aging.

For diminishing the intensity of pore formation in the welded joints of pearlite steels it is advisable to improve technology of their production as well as, when it is appropriate, to replace centrifugal-cast pipes with the pipes produced by electroslag casting, which are characterized by a decreased segregation of alloying elements including chromium both in the section of the pipes and in the body of the α-phase.

Implementation of the process of mechanized welding of such pipes in the established average conditions [6] also permits decreasing segregation of the alloying elements in the α-phase due to optimization of the welding heating, which facilitates an increase of stability of the structure under conditions of operational

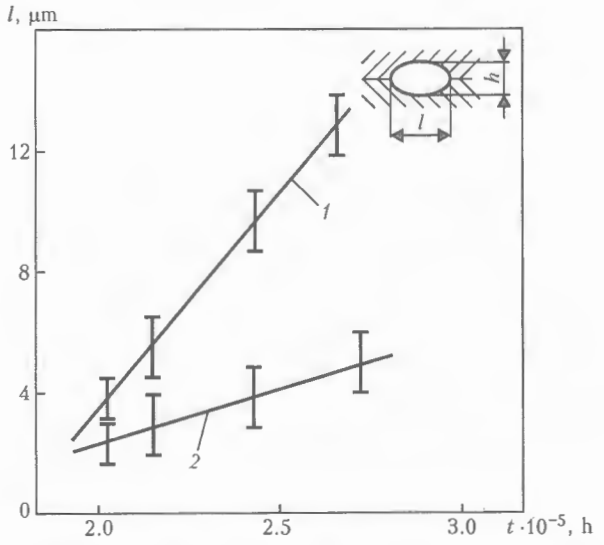

Figure 6. Sizes of pores in weld metal after operating time 190,000 h: *1* — manual arc welding; *2* — mechanized welding in CO_2 + Ar mixture

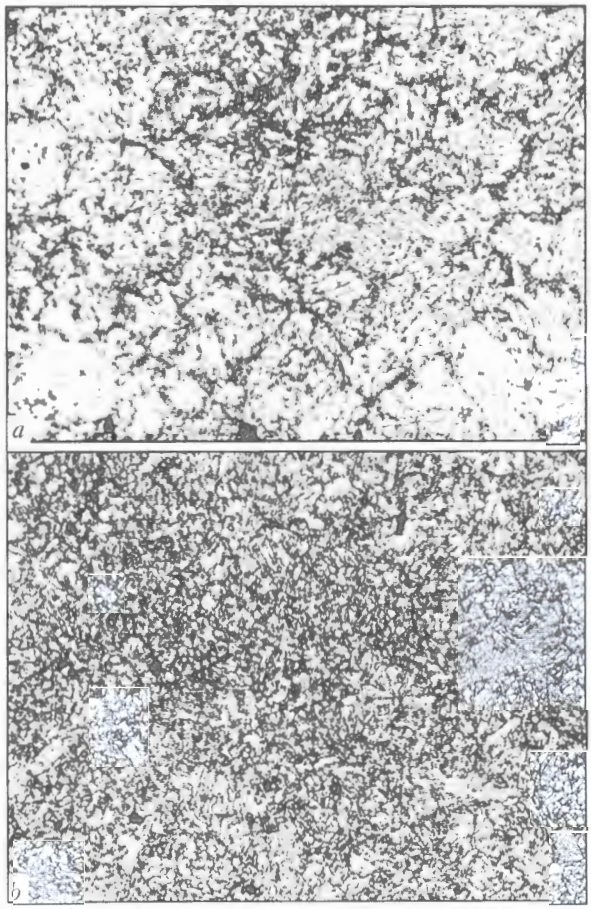

Figure 7. Microstructure of metal in the site of incomplete recrystallization of welded joint HAZ: *a* — manual arc welding; *b* — mechanized welding (new products of austenite decomposition — globulized pearlite) (×100)

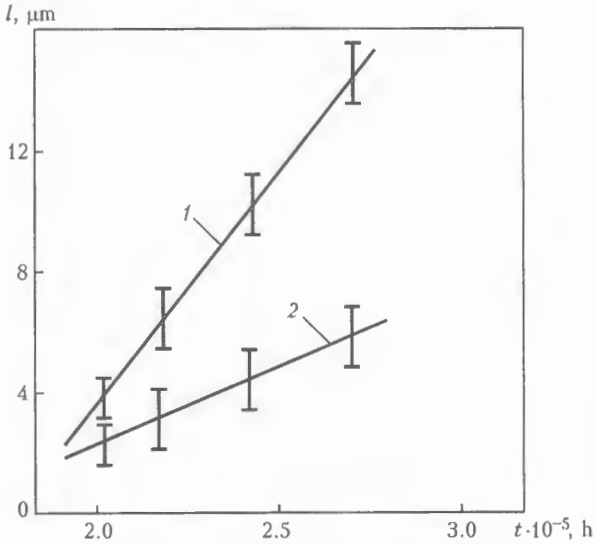

Figure 8. Sizes of pores in the site of incomplete recrystallization of welded joint after 190,000 h of operating time: *1* — manual arc welding; *2* — mechanized welding in CO_2 + Ar mixture

aging and a growth of the operating time resource of the welding joints.

CONCLUSIONS

1. It is shown that initiation and development of pores in the welded joints of Cr–Mo–V thermostable pear-

lite steels are of diffusion character under conditions of low temperature creep at the first stage and of dislocation character at the second stage.

2. It is established that for increasing resistance to pore formation in the initial structure of the indicated welded joints it is necessary to decrease the initial segregation of the alloying elements in the α-phase.

1. Paton, B.E. (2003) Current trends of research and development in the field of welding and strength of structures. *The Paton Welding J.*, **10/11**, 5–11.
2. Makhnenko, V.I. (2003) Improvement of methods for estimation of residual life of welded joints in durable structures. *Ibid.*, **10/11**, 107–116.
3. Mirkin, I.L. (1958) On atomic mechanism of ageing of complex adding alloys. *Transact. of Seminar of AS Ukr. SSR on Heat-Resistant Materials*, **3**, 3–26.
4. Rozenberg, V.M. (1967) *Creep of metal*. Moscow: Metallurgiya.
5. Geguzin, Ya.E. (1962) *Macrodefects in metals*. Moscow: Metallurgizdat.
6. Dmitrik, V.V. (2000) Structure of welded joints from low-alloyed heat-resistant Cr–Mo–V pearlitic steels. *The Paton Welding J.*, **4**, 26–29.
7. Antikajn, P.A. (1984) Safety control of boilers, vessels and pipelines after termination of designed service life. *Teploenergetika*, **2**, 74–75.
8. Khromchenko, F.A. (2002) *Life of welded joints of steam supply lines*. Moscow: Mashinostroenie.
9. Borggreen, K., Huntley, P. (1984) Correction to the constant stress augmented temperature extrapolation method due to oxidation of the subsize creep specimens. In: *Proc. of 2nd Int. Conf. on Creep and Fracture of Engineering Materials and Structures* (Swansea, April 1–6, 1984). Swansea.
10. Dmitrik, V.V., Pashchenko, A.N. (2003) Decrease in structural heterogeneity of incomplete refining region of the HAZ of welded joints in pearlitic steels. *The Paton Welding J.*, **7**, 14–18.
11. Zemzin, V.N., Shron, R.Z. (1978) *Heat treatment and properties of welded joints*. Leningrad: Mashinostroenie.
12. Anokhov, A.E., Alekhova, I.A. (1982) Damage accumulation in welded joints of 12Kh1MF steel steam supply line in creep process. *Svarochn. Proizvodstvo*, **9**, 34–35.
13. Berezina, T.G. (1986) Structural method of determination of residual life of steam supply line parts being in long-term service. *Teploenergetika*, **3**, 53–56.
14. Kumanin, V.I., Kovalyova, L.A., Alekseev, S.V. (1988) *Life of metal in creep conditions*. Moscow: Metallurgiya.
15. Berezina, T.G., Shklyarov, M.I., Shtromberg, Yu.Yu. (1992) Evaluation of life of power equipment parts in creep conditions taking into account the structural factor. *Teploenergetika*, **2**, 2–5.
16. Zlepko, V.F., Perevezentseva, T.V., Novikov, S.V. (1991) Some specifics of structural state of metal of centrifugal-cast steam supply line pipes of 15Kh1M1F steel. *Elektrich. Stantsii*, **3**, 40–43.
17. Barret, Ch.S., Massalsky, T.B. (1984) *Structure of metals*. Moscow: Metallurgiya.
18. Gulyaev, A.P. (1978) *Metals science*. Moscow: Metallurgiya.
19. (1972) *Metallography of iron*. Vol. 1: Principles of metallography. Ed. by F.N. Tavadze. Moscow: Metallurgiya.
20. Pigrova, G.D. (2003) Effect of long-term service on carbide phases in Cr–Mo–V steels. *Metallovedenie i Term. Obrab. Metallov*, **3**, 6–9.
21. (1976) *Tables of physical magnitudes*. Refer. Book. Ed. by I.K. Kikoin. Moscow: Atomizdat.

OPTIMIZATION OF A TRANSFORMER WITH DEVELOPED YOKE MAGNETIC STRAY FLUXES

S.V. RYMAR

E.O. Paton Electric Welding Institute, NASU, Kiev, Ukraine

A procedure is described for optimization of a single-phase transformer with developed magnetic stray fluxes, which uses an upgraded method of stray inductance calculation.

Keywords: *transformer, yoke magnetic stray fluxes, optimization, stray inductance, parameters, welding equipment*

Single-phase transformers with developed yoke magnetic stray fluxes (DYMSF) are widely applied in welding equipment, in particular, in power sources for stick electrode welding.

Fundamentals of the theory of calculation of a transformer with DYMSF and its stray inductance were established by Prof. V.K. Lebedev at the E.O. Paton Electric Welding Institute [1–4], and are widely used by welding equipment designers [5]. However, the publications do not give any information on the procedure of optimization of the considered transformer.

The aim of this study is description of the procedure developed at the E.O. Paton Electric Welding Institute for optimization of a single-phase transformer with DYMSF, based on an upgraded procedure of stray inductance calculation, and providing a high accuracy of calculations.

A higher value of stray inductance in a transformer with DYMSF is due to winding the turns of the primary and secondary windings on different magnet cores with formation of uncompensated winding turns. This reduces the electromagnetic coupling of winding turns and increases the stray flows, running from yoke to yoke in the magnet core [1–4]. Figure 1 is a schematic of such a transformer, where a and b are the thickness and width of the magnet core and yoke, respectively; h_{op} and l_{op} are the height and width of magnet core opening; h_{co1l}, C_{co1l}, and h_{co2r}, C_{co2r} are the height and thickness of coils with the primary and secondary winding on the left and right magnet core; $d_{1l.un}$ and $d_{2r.un}$ are the specified distances between the rods of the magnet core and primary and secondary windings with uncompensated turns; l_{co} is the specified distance between the coil side surfaces in the magnet core open-

ing; Δh is the specified height of magnet core parts protruding from the coils.

Let us consider a two-winding transformer without any additional sections, ensuring discrete regulation of the stray inductance. Transformer is powered by industrial mains with sinusoidal voltage. We will neglect the effect of current ousting to the winding conductor surface. At optimization we will consider only active materials of the transformer, namely electric steel of the magnet core, copper or aluminium of its winding conductors.

Let us formulate equations, connecting the electromagnetic and geometrical parameters of the transformer.

Let us calculate the active cross-section of the magnet core and its yoke [6]:

$$S_{core} = \sqrt{2}U_1/(\omega w_1 B_{mag}), \quad (1)$$

where U_1 is the assigned active value of phase voltage on the transformer primary winding; ω is the angular frequency of the mains voltage calculated by the assigned value of mains frequency f_m equal to $2\pi f_m$; w_1 is the number of primary winding turns; B_{mag} is the specified amplitude value of magnetic inductance in the magnet core.

Thickness of the magnet core and its yoke is equal to [6]

$$a = S_{core}/(k_{core}b), \quad (2)$$

where k_{core} is the specified coefficient of magnet core filling by electric steel plates.

We will find cross-sections of active material of the primary and secondary winding in the magnet core opening from the formula from [7]:

$$S_{w1} = w_1 I_{1l\text{-}t}/J_{1l\text{-}t}; \quad S_{w2} = w_1 I_{2l\text{-}t}/(k_{tr}J_{2l\text{-}t}), \quad (3)$$

where $I_{1l\text{-}t}$, $I_{2l\text{-}t}$ and $J_{1l\text{-}t}$, $J_{2l\text{-}t}$ are the long-term values of current and assigned current density in the primary and secondary windings of the transformer; k_{tr} is the coefficient of transformation ($k_{tr} \approx U_1/U_2$); U_2 is the assigned active value of voltage in the secondary winding in open-circuit mode. Long-term active values of currents in the transformer primary and secondary windings are equal to

$$I_{1l\text{-}t} = I_1\sqrt{X/100\ \%}; \quad I_{2l\text{-}t} = I_2\sqrt{X/100\ \%}, \quad (4)$$

where I_1 and I_2 are the active values of current in the transformer primary and secondary windings; X is the assigned duration of transformer switching on, %.

Active value of current in the transformer primary winding I_1 is determined with a certain excess from expression $I_1 \approx I_2/k_{tr} + I_{o.\text{-}c}$, where $I_{o.\text{-}c}$ is the active value of the transformer open-circuit voltage, which is more precisely determined at the optimization stage. Value of current $I_{o.\text{-}c}$ can be calculated by the procedures from [8, 9], and it may be neglected for approximate calculations. For welding transformers the active value of current in the secondary winding is assigned, and for other transformer types it is calculated by a formula from [6]: $I_2 = S_2/U_{2r}$, where S_2 is the set power of the transformer; U_{2r} is the rated active value of voltage in the secondary winding.

Let us assume that the height of coils with the primary and secondary winding is the same:

$$h_{co1l} = h_{co2r} = (S_{w1}/k_{w1} + S_{w2}/k_{w2})/C_{co\Sigma}, \quad (5)$$

where k_{w1} and k_{w1} are the coefficients of winding filling with the conductor material (values are in the range of 0.50 to 0.95); $C_{co\Sigma}$ is the total width of the coils with windings $C_{co\Sigma} = C_{co1l} + C_{co1r}$.

Thickness of coils with primary and secondary windings is as follows:

$$C_{co1l} = S_{w1}/(k_{w1}h_{co1l}); \quad C_{co2r} = S_{w2}/(k_{w2}h_{co2r}). \quad (6)$$

Width of magnet core opening is determined from the following expression:

$$l_{op} = d_{1l.un} + C_{co1l} + l_{co} + C_{co2r} + d_{2r.un}, \quad (7),$$

and the height of magnet core opening from the following equation:

$$h_{op} = 2\Delta h + h_{co1l}. \quad (8)$$

Average length of turns of the primary and secondary winding is equal to

$$l_{av.t1} = 2(a + b) + 2\pi(d_{1r.un} + C_{co1l}/2);$$
$$l_{av.t2} = 2(a + b) + 2\pi(d_{2r.un} + C_{co2r}/2). \quad (9)$$

Average length of the magnetic force line in the magnet core is as follows:

$$l_{core} = 2(h_{op} + l_{op}) + k_y b. \quad (10)$$

Here k_y is the coefficient allowing for the magnet core type equal to 4 and π in the laminated and wound magnet cores, respectively.

Volume, weight and cost of active materials of the magnet core and windings are as follows:

$$V_{core} = l_{core}S_{core}; \ M_{core} = \gamma_{core}V_{core}; \ C_{core} = c_{core}M_{core}; \quad (11)$$

$$V_w = l_{av.t1}S_{w1} + l_{av.t2}S_{w2}; \ M_w = \gamma_w V_w; \ C_w = c_w M_w, \quad (12)$$

where γ_{core} and γ_w are the active material density of the magnet core and windings, respectively; c_{core} and c_w is the cost of 1 kg of active materials of the magnet core and windings, respectively.

Volume, weight and cost of the transformer active materials are as follows:

$$V = V_{core} + V_w; \ M = M_{core} + M_w; \ C = C_{core} + C_w. \quad (13)$$

Optimization function of the transformer has the following form [7]:

$$F = M_{core} + k_g M_w, \quad (14)$$

where k_g is the generalized weighting coefficient, giving the ratio of the weights of active material of the magnet core and windings, respectively.

Analysis of the transformer optimization model (1)–(4) leads to the conclusion that the independent

variables in it are values w_1, b and $C_{co\Sigma}$, all the others being assigned or dependent. Independent variables are determined through optimization of function F. Minimum values of the optimization function can be found using numerical optimization methods, for instance Gauss–Zeidel method (coordinatewise descent) [10], at the specified initial values of independent variables w_1, b and $C_{co\Sigma}$. Optimization of F function results in determination of optimum values of variables w_1, b, $C_{co\Sigma}$ and other values included into the optimization model.

At $k_g = 1$ transformer design is performed for a minimum of active material weight, in the case of $k_g = \gamma_{core}/\gamma_w$ for a minimum of volume, and at $k_g = c_w/c_{core}$ for a minimum of the active material cost. In the general case k_g can also take other values [7].

After calculation of the optimum geometrical dimensions, the transformer should ensure the assigned level of stray inductance, achieved by redistribution of winding turns. If stray inductance is greater than the assigned one, then part of the primary winding turns in the transformer should be wound with the secondary winding, and the same part of secondary winding turns reduced to the primary winding should be wound with the primary winding. This, however, is not always readily adaptable to fabrication. As a rule, just part of the primary winding turns is transferred (this is connected to the convenience of winding the wires of a smaller cross-section), thus obtaining a quasioptimum transformer, which is only slightly different from the optimum one. Primary winding turns and the same number of reduced turns of the secondary winding on different bars will be uncompensated, and those on one bar will be compensated, because of a stronger or weaker electromagnetic coupling between the turns. If the stray inductance is smaller than the assigned value, an additional choke winding is wound radially around the yoke. This additional winding is connected in series and in aiding connection with one of the windings (usually, the primary winding).

As is seen from Figure 2, primary winding with w_1 turns has w_{1l} turns on the left bar. The right bar carries the secondary winding with $w'_{2r} = w_1$ turns reduced to the primary winding (actually $w_{2r} = w_1/k_{tr}$). Part of primary winding with w_{1r} turns is wound on the secondary winding. Turn number in primary winding w_{1r} on the right bar compensates the same amount of reduced turns of secondary winding. In Figure 2 regions with compensated turns are marked by letter C. Remaining parts of winding turns on the bars are uncompensated and marked by letter H. The following relationships are valid for the transformer:

$$w_1 = w_{1l} + w_{1r}; \quad w'_2 = w'_{2r}.$$

In Figure 2 h_{co1r} and C_{co1r} are the height and thickness of coils with parts of primary winding on the right magnet core; $d_{1l.un}$ and $d_{2r.un}$ are the distances between the cores and parts of windings with uncompensated turns. Other designations coincide with Figure 1.

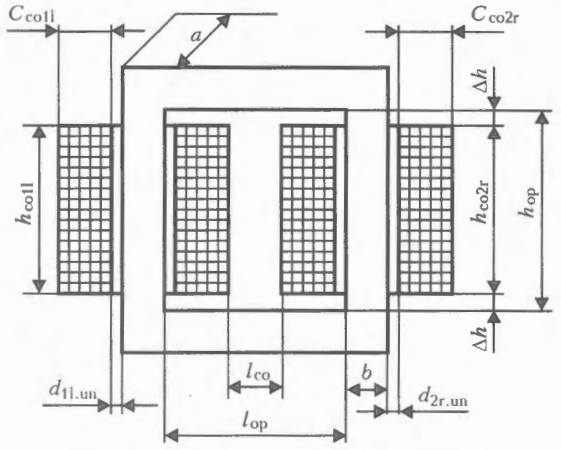

Figure 1. Schematic of a single-phase transformer with DYMSF

Stray inductance L_{co} of the considered transformer can be conditionally divided into three components [11]: $L_{s.op}$ is the stray inductance created by stray fluxes from compensated winding turns in the magnet core opening; $L_{s.c.t}$ is the stray inductance due to stray fluxes from compensated winding turns beyond the magnet core opening; $L_{s.y-f}$ is the stray inductance due to stray fluxes of all the yoke faces and front parts of windings:

$$L_{co} = L_{s.op} + L_{s.c.t} + L_{s.y-f}.$$

Stray inductance in magnet core opening [11, 12]:

$$L_{s.op} = \mu_0 k_R \frac{a + 2d_{av}}{h_{co}} \left(k_L l_{co} + \frac{C_{co1l} + C_{co1r} + C_{co2r}}{3} \right) w_1^2,$$

where k_R is Rogowsky factor [12] equal to

$$k_R = 1 - \sigma[1 - \exp(-1/\sigma)], \qquad (15)$$

coefficient $\sigma = (C_{co1l} + C_{co1r} + l_{co} + C_{co1r})/(\pi h_{co})$; $d_{av} = (d_{1l.un} + d_{2r.un})/2$ is the averaged distance be-

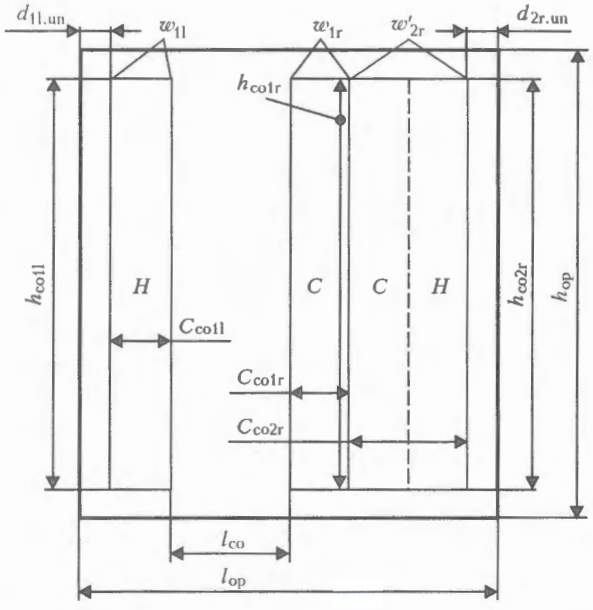

Figure 2. Schematic of winding in the transformer magnet core opening

tween magnet cores and windings with uncompensated turns; $h_{co} = (h_{co1l} + h_{co2r})/2$ is the averaged height of coils with primary and secondary windings, considering that coil heights are $h_{co1r} \approx h_{co1l} \approx h_{co2r}$; $k_L = (w_{1l}/w_1)^2$ is the coefficient.

Stray inductance of part of windings with compensated turns beyond the magnet core opening [12] is as follows:

$$L_{s.c.t} = \mu_0 k_R \frac{a + 2[b - d_{2r.un} + \pi(C_{co2r} + d_{2r.un})]}{h_{co}} \frac{2C_{co1r}}{3} w_{1r}^2.$$

Here Rogowsky factor k_R for winding parts with compensated turns is calculated by the following formula (15) at $\sigma = 2C_{co1r}/(\pi h_{co})$.

Stray inductance between yokes allowing for stray flux between the transformer winding front parts is found from the following expression [11]:

$$L_{s.y-f} = k_f \mu_0 g w_{1l}^2,$$

where k_f is the coefficient allowing for the inductance of the winding front parts, calculated by empirical formula $k_f = 1.1937[\exp(-k) - 0.05]$; k is the coefficient equal to $(C_{co1l} + C_{co2r} - C_{co1r} + 2d_{av})/(5a + 0.2h_{co})$; $g = g_{face}(a, l_y) + 2[g_{face}(b, l_y) + g_{face}(a, b)]$ is the geometrical conductivity between five pairs of symmetrically located faces of magnet core yokes [11]; $g_{face}(a, l_y)$ is the geometrical conductivity between the upper and lower faces of yokes; $l_y = l_{op} + 2b$ is the yoke length; $g_{face}(b, l_y)$ is the geometrical conductivity between the upper and lower front faces of yokes; $g_{face}(a, b)$ is the geometrical conductivity between the upper and lower side faces of the yokes. Geometrical conductivity g_{face} in the form of a function of the dimensions of rectangular plate sides x and y is determined from approximation formula [11]:

$$g_{face}(x, y) = \frac{\sqrt{xy}}{4}\left[2.4 + 1.14\left(\frac{x + y}{\sqrt{xy}}\right)^{0.858}\right].$$

Compared to experimental data the error of calculation of stray inductances L_{co} is not greater than 10 % [11].

If stray inductance after optimization calculation turned out to be greater than the set $L_{co.s}$, the initial number of turns in primary windings on the bars can be determined by the following formula:

$$w_{1l} \approx w_1\sqrt{L_{co.s}/L_{co}}; \quad w_{1r} = w_1 - w_{1l}.$$

If stray inductance turned out to be smaller than the set value, initial number of turns in the additional choke on magnet core yoke connected in series and aiding connection with the primary winding will as follows:

$$w_{1ch} \approx w_1(\sqrt{L_{co.s}/(\mu_0 g w_{1l}^2)} - 1)/k_{mag},$$

where $k_{mag} = 0.75$–0.85 is the coefficient of magne coupling of the choke with yoke stray fluxes of t transformer.

After the initial numbers of the turns have be determined, by further redistributing the prima winding turns it is necessary to achieve the transform stray inductance value as close as possible to the spec fied level.

Developed design procedure was used to desig transformers of a number of power sources develope at the E.O. Paton Electric Welding Institute and suc cessfully operating in Ukraine, Russian Federatio and Lithuania.

Thus, the developed procedure of design of a sin gle-phase transformer with DYMSF enables designing transformers of optimum volume, weight and cost, as well as achieving an error of stray inductance calculation not higher than 10 %, compared to experimental data.

1. Paton, B.E., Lebedev, V.K. (1953) *Elements of calculation of AC circuits and apparatuses for arc welding*. Kiev: AN Ukr. SSR.
2. Paton, B.E., Lebedev, V.K. (1966) *Electric equipment for arc and slag welding*. Moscow: Mashinostroenie.
3. Lebedev, V.K. (1958) Calculation of short-circuit resistance of the welding transformer with yoke dissipation. *Avto matich. Svarka*, **4**, 37–43.
4. Lebedev, V.K., Troitsky, V.A., Bely, N.G. (1968) Transformer with yoke dissipation controlled by welding cable. *Ibid.*, **6**, 61–65.
5. Kobozev, V.A., Kovalenko, V.V. (1998) *Welding transformers*. Stavropol.
6. Tikhomirov, P.M. (1986) *Transformer design*. Moscow: Energoatomizdat.
7. Pentegov, I.V., Rymar, S.V., Stemkovsky, E.P. (2002) Optimization mathematical model of a three-phase transformer and selection of its design in multicriterial optimization. *Tekhn. Elektrodynamika*, **1**, 22–28.
8. Pentegov, I.V., Rymar, S.V. (1995) Method of determination of losses in transformer steel oriented to CAD application. *Ibid.*, **6**, 35–40.
9. Pentegov, I.V., Rymar, S.V. (1996) Method of calculation of transformer open-circuit current oriented to CAD application. *Ibid.*, **1**, 39–45.
10. Koryachko, V.P., Kurejchik, V.M., Norenkov, I.P. (1987) *Theoretical principles of CAD*. Moscow: Energoatomizdat.
11. Pentegov, I.V., Rymar, S.V. (2004) Features of calculation of stray inductance of transformers with developed magnetic stray fluxes. *Elektrotekhnika i Elektromekhanika*, **2**, 38–45.
12. Vasyutinsky, S.B. (1970) *Problems of theory and design of transformers*. Leningrad: Energiya.

ZIRCONIUM: ALLOYS, WELDING, APPLICATION (REVIEW)

V.E. BLASHCHUK
E.O. Paton Electric Welding Institute, NASU, Kiev, Ukraine

The paper describes the advantages of zirconium and its alloys compared to other structural materials, methods of their production and application in industry, as well as welding features. Applications of zirconium and its alloys, as well as prospects for their use are mentioned.

Keywords: *welding, zirconium and its alloys, production, application*

Progress of science and engineering in many sectors (power engineering, metallurgy, machine-building, aviation and rocket production) is directly connected with application of fundamentally new materials with their previously unknown properties. So due to the development of nuclear power engineering related to a more intense application of the materials with a low section of the seizure of thermal neutrons (this property of the material is combined with sufficient strength and corrosion resistance in water and water steam at increased temperatures) the prerequisites were created for bringing production of zirconium to the commercial scale. Technologies were developed for production of zirconium and its alloys with the purity necessary for atomic industry, particularly for materials of fuel element shells in different types of nuclear reactors. Expansion of production of zirconium and its alloys as well as a certain decrease of their application in the nuclear power engineering created conditions for their application in production of chemical equipment.

Zirconium is considered a rare element. However, it is in the first third of all known elements as to its prevalence on the Earth. Hafnium is an invariable companion of zirconium. Both elements are present in one mineral – zircon (hafnium is in 50–60 times less quantities than zirconium). In Ukraine zirconium is produced from placers together with titanium minerals. From the days of old 11 complex titanium-zirconium deposits are known in Ukraine with their reserves capable to supply Ukraine, a monopolist in the CIS countries, for a long time. Production of titanium-zirconium ores in Ukraine makes up 20 % of the world production [1].

Zirconium was discovered in 1789 by M.G. Klaprot[1] in the zircon mineral. Origin of the name is explained differently: from the Arabic word «zarkun», which means mineral, or from two Persian words «tsar» (gold) and «gup», which means color, because of the golden color of jacinth, a precious variety of zirconium. Metallic zirconium was for the first time produced by J.J. Berzelius[2] by reduction of potassium fluor-zirconate with metallic sodium. Pure plastic zirconium was produced in 1925 by thermal dissociation of zirconium iodide (the so-called iodide zirconium). This method developed by the Dutch scientists A. van Arkel and I. de Bur initially gained some acceptance but a high cost of the produced zirconium essentially restricted a sphere of its application. The improved Croll method was the next stage in the development of a cheaper method. A scheme of this production provides two main stages: chlorination of zirconium dioxide and reduction of the produced zirconium four-chloride by metallic magnesium (magnesium-thermal zirconium) or by potassium (potassium-thermal zirconium) under melted metal layer. The end product was a zirconium sponge that was then melted into a compact metal by arc-vacuum melting or electron beam melting in vacuum [2–4].

Zirconium falls into a category of transition metals of IVA group of the periodic system (titanium, zirconium, hafnium). All metals of this group are polymorphous, have hexagonal lattice for low-temperature (α) modification and centered lattice for high-temperature (β) modification. They have a little difference in the values of atomic radii and are capable to form solid solutions with many elements. Continuous solid solutions are formed with metals of isomorphic structure.

Titanium, zirconium and hafnium correlating with one another form continuous solid solutions with both modifications. Triple system Ti–Zr–Hf is so far the only known system combining two types of continuous solutions of two (α- and β-) modifications. This creates good prerequisites for direct welding of zirconium with titanium even if zirconium alloy contains hafnium additions. β-Zr forms continuous solid solutions with niobium, tantalum and uranium [5].

Zirconium has increased resistance to a number of corrosive chemical media [6–9]. For this reason it is

[1]Martin Henrich Klaprot [01.12.1743, Wernigerode – 01.01.1817, Berlin] is German chemist and naturalist.
[2]Jens Jacob Berzelius [20.08.1779, Veversunda – 07.08.1848, Stockholm] is the known Swedish chemist and mineralogist.

a unique structural material for production of the units of chemical equipment contacting in turn with hot strong acids and with hot caustic alkali.

Zirconium having the smallest as against other structural materials effective cross section of the seizure of thermal neutron ($S = 0.18 \cdot 10^{-28}$ m^2) is an ideal material for nuclear power units. However, this property is typical for zirconium that does not contain even small impurities of hafnium ($S = 115 \cdot 10^{-28}$ m^2). Since many physicochemical properties of hafnium and zirconium are almost identical it proves rather difficult to obtain highly pure zirconium containing no hafnium. Industry produces two types of raw material zirconium on the commercial scale: reactor zirconium (with no hafnium) and general purpose one (containing up to 4.5 % Hf). In such quantities hafnium has almost no effect on corrosion resistance of zirconium in corrosive media while the absence of refining for removal of hafnium leads to a considerable decrease of the cost of semi-products made of zirconium. From the standpoint of the design engineer of chemical equipment, who is not involved into rocket production, any zirconium alloys are suitable material if one requires a special corrosion resistance typical for this material.

Zirconium is not practically exposed to the action of hot water and steam. However, at increased temperatures (about 380–400 °C) under the long-term action of the overheated water one can observe embrittlement of zirconium, which is explained by a gradual oxidation of metal and dissolution of hydrogen formed from water in it [10].

Inconsiderable quantities of harmful impurities (gases) sharply deteriorate properties of zirconium. Nitrogen is one of the most harmful impurities [11]. Zirconium actively correlates with nitrogen and oxygen forming compounds ZrN and ZrO_2 distinguished with refractoriness and high hardness. Increase of nitrogen content in zirconium sharply deteriorates a corrosion resistance. The more is the temperature of tests (under operation in water) the more pronounced is the nitrogen effect. Harmful effect of nitrogen may be decreased by alloying of zirconium with tin. Of all the interstitial elements in zirconium only hydrogen is considered not only like harmful impurity but also like alloying element [12]. Under oxygen content one observes strengthening, increase of creep resistance, a relatively weak effect on corrosion resistance of zirconium and some of its alloys.

Zirconium quickly absorbs hydrogen at the temperature 300–1000 °C. In this case it becomes brittle and harder, its magnetic susceptibility with hydrogen saturation becoming lower. At the temperatures higher than the temperature of eutectoid transformation the stabilizers of α-phase (tin, antimony, aluminium, thorium, cadmium, oxygen, nitrogen, rare-earth elements) increase hydrogen solubility while β-stabilizers decrease it. This effect is inconsiderable at the lower temperatures. Solubility of hydrogen in β-Zr decreases with increase of the oxygen content. Hydrogen dissolved in zirconium has a lower effect on the corrosion resistance than nitrogen but leads to failure by the mechanism of retarded hydride cracking. Harmful effect of hydride plates stops at the temperature 200 °C. Hydrogen may be removed at 1200–1300 °C under conditions of high vacuum [13, 14].

Correlation of zirconium with CO_2 results in formation of zirconium oxides and carbides while correlation with steam ($T \cong 300$ °C) leads to formation of oxides and hydrides. Carbon promotes higher corrosion in water and steam. Besides, impurities of aluminium, beryllium, potassium, cadmium, magnesium and lead also exert their effect. Impurities of iron, silicon and others increase corrosion resistance blocking the effect of harmful impurities. Not only an absolute quantities of impurities have their effect but also a change of the correlation of positively (iron, chromium, nickel) and negatively (nitrogen, hydrogen, aluminium) affecting impurities. All this determines general corrosion behavior of zirconium alloys [2–6].

Most widely zirconium and its alloys are employed in the economical nuclear power engineering as shells for fuel elements, channel pipes and other structural elements of the active zone of power reactors [8, 9, 15–17]. Table 1 presents compositions of zirconium alloys used in active zones of the reactors. Niobium is the basic alloying element both for binary and for multi-component alloys. Table 2 presents compositions of zirconium alloys by ASTM classification. Zirconium of commercial purity (Table 2) did not gain application neither in domestic (E100) nor in foreign nuclear power engineering.

Zirconium alloys of reactor purity of grades KTTs-125 (analog of E100 grade), KTTs-110 (E110) and KTTs-125 (E125) on the basis of potassium-thermal zirconium (PTZ) with additional refining are developed in Ukraine. Application of electron beam remelting allows purifying PTZ alloys from slag inclusions and impurities more volatile than zirconium [18].

Alloys E110 and E635 gained their application in the state approaching the recrystalized one. In the initial state it provides their higher plasticity. As a result of niobium alloying they absorb a considerably smaller quantity of hydrogen, which favorably differ them from Zircalloy-type alloys. The developed techniques of their process stage provide an optimal texture excluding unfavorable orientation of hydrides. Alloys E110 and E635 possess high corrosion resistance under their operation in water under pressure due to formation of thin oxide films on the surface of the article. However, E110 and E635 essentially differ for corrosion resistance in boiling water. During surface or bulk boiling one can observe on the articles of E110 alloy «nodule» corrosion, which is absent on the similar articles of alloy E635. This is related to the difference in chemical compositions of α-solid solution composing the basis of the alloy. Enrichment of α-solid solution in the alloy E635 with iron increases its corrosion resistance as a result of diffusion dissolution of

Table 1. Zirconium-based alloys employed in nuclear power engineering

Alloy grade	*Content of basic alloying elements, %*					*Type of reactor*	*Country-developer (year)*
	Nb	*Sn*	*Fe*	*O*	*Others*		
Э110	1.0	–	–	< 0.16	–	WWER, RBMK	USSR (1958)
Э125	2.5	–	–	–	–	WWER, RBMK, CANDU	USSR (1958)
Э635	1.0	1.0–1.5	0.3–0.5	–	–	WWER, RBMK, PWR, BWR, CANDU	USSR (1971)
Zry-2	–	1.2–1.8	0.07–0.20	–	≤ 0.08Ni 0.05–0.15Cr	BWR	USA (1952)
Zry-4	–	1.2–1.8	0.18–0.24	–	0.07–0.13Cr	PWR	USA (1952)
ZIRLO	1.0	1.0	0.1	–	–	PWR	USA (1990)
M4	–	0.5	0.6	0.12	0.3V	PWR	France (1997)
M5	1.0	–	–	0.12	–	PWR	France (1997)
NDA	0.1	1.0	0.27	–	0.16Cr	BWR	Japan (1990)
MDA	0.5	0.8	0.2	–	0.1Cr	PWR	Japan (1990)

Table 2. Zirconium alloys by ASTM classification

Material	*Commercial name*	*ASTM grade (UNS Number)*	*Weight content of elements, %**				
			Zr + Hf	*Sn*	*Nb*	*Fe + Cr*	$[O]_{max}$
Commercially pure zirconium	Zircadine 702	R60702**	99.2	–	–	≤ 0.2	0.16
		R60001***					
Alloys	Zircadine 704	R60704**	97.5	1.0–2.0	–	0.2–0.4	0.18
	Zircaloy-2	R60802***					
	Zircadine 705	R60705**	95.5	–	2.0–3.0	≤ 0.2	0.18
	Zircadine 706	R60706**	95.5	–	2.0–3.0	≤ 0.2	0.16
	Zr–2.5Nb	R60901***					

*Maximal content of gases: 0.0005[H], 0.025[N], 0.05[C].
**General purpose alloy (maximum 4.5Hf).
***Alloy for nuclear power engineering (maximum 0.01Hf).

intermetallide particles under the action of neutron irradiation. Its higher creep resistance is also explained by the same reason. Alloy E635 possesses high resistance to radiation growth as a result of specific dislocation structure as well as high resistance to the so-called retarded hydride cracking. Typical mechanical properties of certain zirconium alloys are presented in Table 3.

Along with the indicated alloys a series of other zirconium alloys were developed that have not yet gained practical application. A group of heat-resistant alloys (for example, alloy Zr–3.2Sn–1.1Mo–1.1Nb and others are developed but they have a low corrosion resistance [8, 9]).

The following welding methods are applied for zirconium and its alloys: electron beam welding, plasma and microplasma welding, TIG welding with local shielding and in the chambers with controlled atmosphere, resistance welding and welding in the solid phase [8, 9, 19–27].

Before welding the edges of the articles to be connected are subject to machining of two sides on each side of the butt (conditioning with emery wheel and scraper for the width of 20–30 mm from the butt with subsequent degreasing). With the aim of decreasing a possibility for saturation of the metal surface layers with hydrogen it is advisable to avoid etching of edges before welding. However, in some cases chemical cleaning of edges is allowed on condition that all requirements of the specifications are strictly observed [23].

EBW in vacuum not worse than $1.33 \cdot 10^{-3}$ Pa is one of the most promising methods of fusion welding

Table 3. Mechanical properties of zirconium and its alloys at different testing temperatures

Material	σ_t, *MPa*		$\sigma_{0.2}$, *MPa*		δ, *%*	
	20 °C	*300 °C*	*20 °C*	*300 °C*	*20 °C*	*300 °C*
Iodide zirconium of arc remelting	220	120	80	45	45	55
Zircaloy-2	480	200	310	100	22	35
E110 (H-1)	350	200	200	120	30	33
E125 (H-2.5)	450	300	280	200	25	23

of zirconium and its alloys because in this case favorable conditions for pure atmosphere are created. In this situation it is appropriate to apply pumping-out systems allowing production of high oilless vacuum. In EBW of E110 and E125 alloy plates a short-term strength of welded joints is provided at a level of at least 0.9 of the same index for the parent metal within the testing temperature range 20–300 °C. Under EBW the oxygen content in the weld metal considerably decreases as a result of vacuum extraction, which changes operational characteristics of the welded joints.

Porosity of welds detected by the X-ray control is the main problem in the EBW of zirconium and its alloys. The studies have shown that organic microimpurities of the surfaces being welded are the main reason of such porosity. It is possible to prevent porosity by a set of measures on maintaining the production culture and by maximal degassing of the butt in welding by means of technological conditions of EBW and structure of the parts in the zone of joining [24].

Non-equilibrium α′-phase of variable composition — oversaturated solid solution of niobium in α-Zr — forms in the weld metal of E110 and E125 in fusion welding. In this case along with α′-phase there is in the HAZ metal a residual high-temperature β-phase of zirconium — a solid solution of niobium in β-Zr of variable composition, which does not decompose in the process of cooling. The presence of non-equilibrium α′- and β-phases in the weld metal and HAZ decreases corrosion resistance of welded joint. Annealing in (α + β)-Nb area of the constitution diagram of Zr–Nb system provides higher corrosion resistance than annealing in (α + β)-Zr area. However, in this case a longer holding (50–100 h) is required, which is inconvenient and non-economical.

Currently TIG and MIG welding (in argon, helium and their mixtures) has gained the widest application in the chemical machine-building for joining of zirconium and its alloys [22]. The following methods for shielding the welding zone and cooling down sites of the welded joint with inert gases are used in welding of zirconium (and titanium) depending on the sizes and configuration of the articles to be welded:

• general shielding of the article to be welded in the chamber with controlled atmosphere. Application of such chambers provides a more reliable and stable shielding of the zone of welding and cooling down parts of the weld joint from the face and reverse sides. Vacuum not worse than $1.33 \cdot 10^{-2}$ Pa is created in the chamber before it is filled with inert gas. He or He + + 25 vol.% Ar mixture is used for filling the chamber in welding of zirconium. When chambers are filled with argon a tendency to pore formation increases. The gas before feeding to the chamber is exposed to additional purification and drying. Application of binary mixtures with oxygen and nitrogen in case of such welding allows alloying zirconium welds from the gas phase with the aim on increasing strength of the weld metal. In this case oxygen alloying of weld metal in the alloy E125 within the concentration range 0.05–0.15 wt.% increases strength of the welded joint after heat treatment by 20 % without noticeable decrease of plasticity and impact toughness. However, if the weld is sufficiently long it is impossible to receive a uniform content of the alloying gases;

• local shielding of the welding zone with local chambers has gained application mainly for welding of rotatory and non-rotatory butts of pipe lines;

• local jet shielding of the welding zone and cooling down parts of the welded joint by means of displacing torch nozzle with an extension for blowing cooling down sites as well as shielding of the reverse side of the welded joint by means of blowing appliances of different design.

Automatic and manual TIG welding with a jet shielding of the welding zone and cooling down parts with and without feed of filler wire is most widely used for joining of zirconium alloys.

Filler wires of different diameters of alloys E100, E110 and E125 (TS 952118–90) are applied for welding zirconium alloys in domestic practice. Abroad in compliance with AWS A5–90 the following filler wires are used: wire of grade ERZr — for zirconium of commercial purity (alloy UNS R60704), ERZr3 — for alloy Zr-1.5Sn (alloy UNS R60704) and ERZr4 — for alloy Zr-2.5Nb (alloys UNS R60705 and R60706). Wires of zirconium alloys are produced only of reactor purity, i.e. with very low hafnium content and introduction interstitial impurities.

Shielding appliances used for welding of titanium do not provide necessary quality of the shielding estimated by the temper colors. Therefore, it is necessary to enlarge their geometrical sizes with the aim of increasing the shielding zone as well as the use of different appliances (for example, equipped with water cooling) for increasing the intensity of heat removal from the welding zone. A dependence of the shielding quality on the welding speed and time of the hot sites staying in the zone of shielding with inert gas is expressed more distinctly in welding of zirconium than in welding of titanium. The use of helium as a shielding gas in welding of zirconium allows doubling (as against argon) the cooling rate of the welding zone. This restricts the development of chemical heterogeneity in the welding joint and leads to improvement of its properties. However, the use of welding in helium is limited by its high cost as compared to argon.

The pulse process of TIG welding with a wide range of regulation of the arc heat effect on the metal is used for welding of zirconium plates of small thickness. Advantages of this welding also include large clearances for edge preparation, installation of backings and fixtures as well as a decrease of distortion of the plates to be welded. These factors allow decreasing expenses for welding operations because of the reduction of time for welding and a sharp decrease of defects.

Preliminary cold-work hardening gained application for acceleration of establishing an equilibrium

state in the weld joint metal under postweld heat treatment of zirconium alloys. Cold plastic deformation as well as thermocyclic treatment for creation of preliminary cold-work hardening facilitates fast and fool decomposition of α-phase in the welded metal under PWHT. Besides, sizes of the appearing β-Nb particles (alloys of the Zr–Nb system) decrease and their distribution in the matrix becomes uniform.

Zirconium alloys are well joined by all methods of resistance welding – spot, seam, butt and fusion welding. High resistance in combination with low thermal conductivity makes this process easier. Conditions of spot welding of zirconium for current density exceed conditions for welding of titanium alloys of the same thicknesses 1.6–1.7 times. Seam welding is performed with additional argon shielding [25].

Zirconium alloys are joined by diffusion bonding in vacuum not worse than $1.33 \cdot 10^{-2}$ Pa at the temperatures 750–950 °C and welding time 20 min.

In addition to the mentioned welding methods zirconium pipelines are also joined by the magnetic pulsed welding and friction welding. Studies of the welded joints of pipes of zirconium alloys show that the strength of welded joints of pipe specimens under variable loads depends on the method of welding and structure of the welded joint. The mentioned factors do not influence the static strength. In this case endurance of the joints carried out by the magnetic pulsed welding and resistance butt welding is 2.5–3 times lower of the same index for the pipes produced by the EBW. Therefore, the mentioned welding methods gained limited application for joining pipes of zirconium alloys with all simplicity of their performance.

Friction welding of pipes of zirconium alloys is carried out in the solid state with argon feed into the butt zone. It allows producing sufficiently high welded joints in the case when in the welding process the temperature of metal forming the welding joint does not exceed the temperature of polymorphous transformation of the alloy while the butt is subject to heat treatment in (α + β) area of the constitutional diagram of the Zr–Nb system. In this case the metal heated to high temperatures at the stage of forging is squeezed into flash and then removed. The metal left in the welded joint has a fine structure with a low level of structural and chemical heterogeneity. Indices of durability of the welded joints performed by EBW and friction welding are equal in low cycle fatigue testing [26].

In fusion welding of zirconium to other metals it is very important to select correctly the method and technique of welding. In view of high cost of zirconium it often proves economically appropriate to produce combined Ti–Zr welded structures [21]. In automatic TIG welding of commercial titanium VT1-0 to alloys E110 and E125 the tungsten electrode shifts towards the weld by 1.5–2 mm for increasing the volume fraction of refractory metal (zirconium) in the weld metal. When the tungsten electrode shifts towards the butt zirconium penetration deteriorates resulting in lacks of fusion and laps. In welding of VT1-0 + E110 alloys α′-phase with hexagonal close-packed lattice forms in the weld metal while in welding of VT1-0 + E125 a low quantity of β-Zr-phase is formed. In this case heat treatment in the α-area (vacuum is not worse than $0.2 \cdot 10^{-2}$ Pa) does not lead to formation of the equilibrium β-Zr-phase in the weld metal. It preserves the martensite-type structure of α′-phase. No essential changes are observed in the structure of HAZ metal from the side of titanium and zirconium alloys. At the same time under heat treatment one can observe in the β-area a full recrystallization of the weld and base metals. There occurs partial homogenization of the solid solution and a decrease of microchemical heterogeneity as well as intensive growth of grains in BM and HAZ metal. Size of primary β-grains does not practically change in the weld metal. Retarded cooling down leads to formation of coarse large-needle structure of α-phase in the weld metal and BM typical for two-phase Zr–Ti alloys cooled down with low speed from β-area. Structure of BM (VT1-0) and HAZ metal is a large-laminar α-phase. However, irrespective of the fact that titanium and zirconium are in one group of the periodic system and are metals-analogs forming a continuous series of solid solutions, their weld metal has relatively low indices of plasticity and impact toughness. All this becomes even more pronounced in welding of zirconium alloys to high-strength (α + β)-Ti alloys. For joining such plate alloys (for example, E125 + VT3-1) the spot EBW is applied without filler metal using penetration of the spot by a repeated pass from the side of zirconium alloy so as to penetrate intermetallide interlayer for improvement of plastic properties of the welded joint.

Explosion welding has gained its application for producing zirconium–steel bimetal as well as for performing lap joint of the E125 alloy pipe with the pipe of stainless steel. In this case the presence of dispersion intermetallides in the contact zone does not deteriorate mechanical properties of the welded joint distinguished with its high thermal stability at the temperature 400 °C. Successful experiments on cold welding of zirconium and stainless steel specimens are carried out. Failure of such joints under their test for low-cycle fatigue proceeds by zirconium [8, 9, 19].

Technological processes of producing welded articles of E125 alloy are necessarily include postweld annealing. Annealing in vacuum or in inert gases of large-scale articles or their parts is related to certain difficulties – the absence of necessary equipment, considerable increase of costs and others. Zirconium is intensively correlating with active gases under air annealing. At the same time plasticity of the welded joint metal increases as a result of partial decomposition of martensite at the annealing temperature 470–480 °C for 2 h. Embrittling effect of the gases absorbed from the atmosphere is exposed poorly. A film of black color having a good adhesion with a base forms on the surface of zirconium as a result of such annealing.

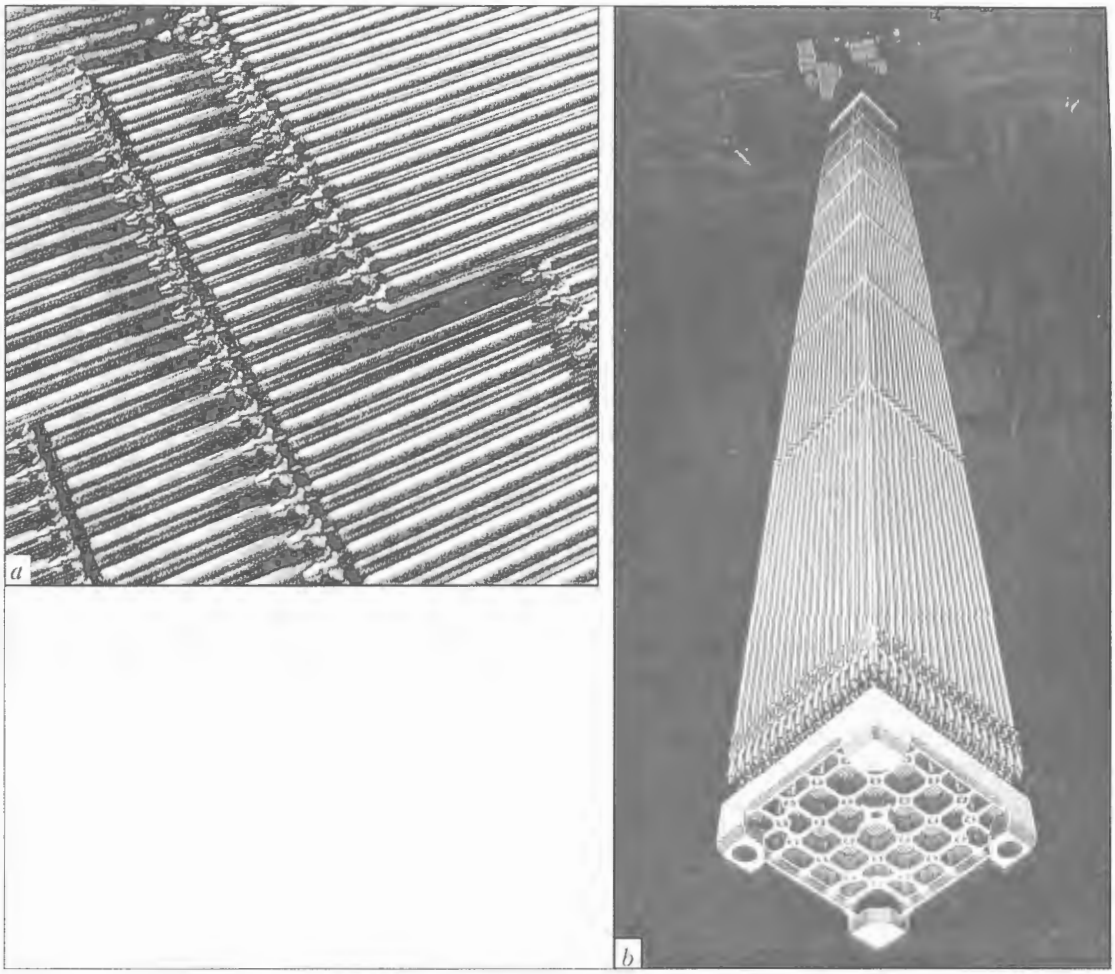

Figure 1. Fuel elements (*a*) and fuel assemblies (*b*) produced of the Framatom zirconium alloy M5

This film presents a solid solution of zirconium in zirconium dioxide with a small quantity of zirconium nitride. Such oxidation of the welded joints as a result of the air annealing increases their corrosion resistance and prevents hydrogen absorption. Annealing is not needed in welding of E100 and E110 alloys because in their initial state they have sufficient reserves of plasticity and impact toughness.

Alloys of Zr–Nb system and their welded joints have high corrosion resistance and are not exposed to corrosion cracking under stress in any highly corrosive technological media of the chemical industry. For increasing resistance of welded joints and structures of zirconium alloys to early failure in the corrosive media it is necessary to use rational structures and welding technologies [6–10, 15–21, 23, 27].

Ferrous metallurgy is the first consumer of metallic zirconium. Zirconium proves a good deoxidizer surpassing manganese and titanium. At the same time it decreases the content of gases and sulphur in steels. Nonferrous metallurgy also consumes big quantities of zirconium. Besides, it is used for alloying of titanium, aluminium, molybdenum and others increasing corrosion resistance and mechanical properties of alloys.

Nuclear power engineering is the main branch for applying zirconium and its alloys. Reactor installed on the American submarine «Nautilus» was the first large structure of zirconium. Eventually it turned out that it is more advantageous to use zirconium for production of fuel element bodies and fuel assemblies (Figure 1) than stationary parts of the active zone of the reactor.

Chemical industry becomes increasingly large consumer of parts of zirconium and its alloys. High corrosion resistance and relatively high melting temperature (1865 °C) create favorable conditions for wide application of zirconium. It has gained application in the textile industry for production of spinnerets in manufacturing of artificial fibers; for production of chemical equipment operating in conditions of increased temperatures and corrosive media (pumps, parts of hot stop valves, heat exchangers, filters, reactors, tanks, laboratory and medical equipment) as well as for production of acetic acid. A wider use of zirconium is restrained by its high cost. Lining of titanium equipment with panels of zirconium alloys is an alternative. Freely fitting lining of E125 alloy 2 mm thick was produced for protection of column (titanium alloy VT1-0 is the parent metal of the body) for depolarization of paraldehyde. The column is successfully operating in production conditions [8].

All parts of the transport-technological container (Figure 2) contacting with the corrosive liquid (four-chloride silicon or four-chloride germanium of extra pure) are produced from plate alloy E110 2 mm thick.

Figure 2. Welded transport-technological container of alloy E110 with 20 l capacity

Figure 3. Welded pipe heat-exchanger and heater of alloy E125

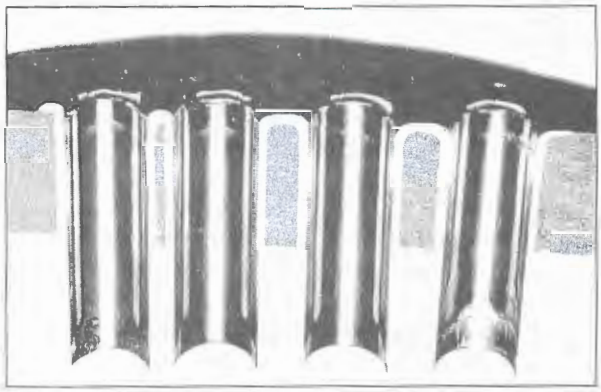

Figure 4. Macrosection of the welded joints of tube plate (VT1-0) with tubes (E125)

Both manual and automatic TIG welding were used for production of the container. Titanium of grade VT1-0 2 mm thick was used for producing auxiliary parts not contacting with corrosive medium. The parts were welded to the body of the transport-technological container through the inserts of E110. The performed tests showed that the quality of the transported media (admissible content of metallic and hydrogen containing impurities) does not practically differ from the initial quality after three months (guaranteed storage period). The use of the transport-technological containers produced of zirconium removes the problem of utilizing of the previously used one-time bottles of small capacity made of special glass or fluoroplastic [21].

Welded pipe heat exchanger and heater for heating pre-hydrolysis solution in production of TiO_2 (Figure 3) is a six-section pipe structure with the working surface area 36 m^2 (diameter is 3200 mm, height is 2650 mm). Supporting pipes 70 × 3.5 mm in diameter and pipes of registers 50 × 3 mm in diameter are produced of alloy E125. Manual TIG welding with filler of the alloy E110 was used [21]. Heat exchangers of the same type are successfully operating in titanium industry.

In production of the heat exchanger a tube plate of titanium alloy VT1-0 80 mm thick and tubes of zirconium alloy E125 were produced for degreasing the acetic acid (Figure 4). Tubes were jointed to tube plate by manual TIG welding without filler by flashing of the tube ends protruding over the plate surface by 2–2.5 mm. Examination of the heat exchanger after 15,000 h of operation confirms a possibility and perspectiveness of production of such apparatuses.

Due to high corrosion resistance zirconium gained application for production of different instruments for surgery. It is established that pure zirconium does not induce any reactions and changes in the muscle tissues, bones and brain of a human. It is used for production of hemostatic forceps, skull plates and even threads for application of seams in brain operations.

1. (2001) *Atlas on geology and minerals of Ukraine.* Ed. by L.S. Galetsky. Kiev: UITsTP Geos-XXI st.
2. (1967) *Refractory materials in machine-building.* Refer. book. Ed. by A.T. Tumanov, K.I. Portnoj. Moscow: Mashinostroenie.
3. Duglas, D. (1975) *Metals science of zirconium.* Moscow: Atomizdat.
4. Paton, B.E., Trigub, N.P., Kozlitin, D.A. et al. (1997) *Electron beam melting.* Kiev: Naukova Dumka.
5. (1966) *Metal-chemical properties of periodic system elements.* Ed. by I.I. Kornilov. Moscow: Nauka.
6. Tomashov, N.D., Chernova, G.P. (1986) *Theory of corrosion and corrosion-resistant structural alloys.* Moscow: Metallurgiya.
7. (1990) *Corrosion of structural materials.* Refer. book. Ed. by V.V. Batrakov. Moscow: Metallurgiya.
8. Blashchuk, V.E. (1999) Corrosion of zirconium alloy welding joints. In: *Welding and Surfacing Rev.* Vol. 11.
9. Tubielewicz, K., Blaszczuk, W., Melechov, R. (2001) *Technologiczne wlasciwosci cyrkonu.* Czestochowa: Politechnika Czestochowska.

10. Perekhozhev, V.I., Sinelnikov, L.P., Timokhin, A.N. et al. (2003) Uniform and «nodular» corrosion of zirconium alloy in operating conditions. *Metallovedenie i Term. Obrab. Metallov*, **10**, 26–31.
11. Grigorenko, G.M., Pomarin, Yu.M., Orlovsky, V.Yu. (2001) Kinetics of interaction of nitrogen with melted zirconium and titanium. *Problemy Spets. Elektrometallurgii*, **2**, 32–37.
12. Chernyaeva, G.P., Stukalov, A.I., Gritsyna, V.M. (1999) Behavior of oxygen in zirconium. In: *Proc. of Conf. on Problems of Zirconium and Hafnium in Nuclear Power* (Alushta, Ukraine, July 14–19, 1999).
13. Vlasov, N.M., Fedik, I.I. (2003) Hydrogen embrittlement of zirconium alloys. *Metallovedenie i Term. Obrab. Metallov*, **8**, 48–51.
14. Ivanova, S.V., Shikov, A.K., Bocharov, O.V. (2003) Hydrogenation of zirconium products during fabrication and service as a limiting factor of their service life in WWER and RBMK reactors. *Ibid.*, **8**, 40–47.
15. Soloviov, Yu.V., Bulatov, G.S., Gedgovd, K.N. (2000) Mechanical properties and stress corrosion cracking of zirconium alloys. *Materialovedenie*, **4**, 19–27.
16. Solonin, M.I., Reshetnikov, F.R., Ioltukhovsky, A.G. et al. (2001) New structural materials of active sections of nuclear power plants. *Fiz. i Khim. Obrab. Materialov*, **4**, 17–27.
17. Nikulina, A.V. (2003) Zirconium-niobium alloys for elements of active sections of pressurized water reactors. *Metallovedenie i Term. Obrab. Metallov*, **8**, 7–13.
18. Zelensky, V.F. (2003) On history of formation and development of nuclear materials science in Ukraine. In: *Progressive materials and technologies*. Vol. 1. Kiev: Akademperiodika.
19. Gurevich, S.M. (1990) *Reference book on welding of nonferrous metals*. Kiev: Naukova Dumka.
20. Asnis, E.A., Goncharov, A.B., Nerodenko, M.M. et al. (1995) Welding of refractory metals. In: *Welding and Surfacing Rev.* Vol. 5.
21. Blashchuk, V.E., Shelenkov, G.M., Troyanovsky, V.E. (1997) Welding of zirconium alloys E110 and E125. *Avtomatich. Svarka*, **12**, 31–34.
22. (1998) *AWS Welding Handbook*. Miami, Florida: AWS.
23. Plyshevsky, M.I., Rassoshkina, N.S., Semyonov, A.N. et al. (2001) Influence of shielding conditions in welding and quality of surface preparation on corrosion resistance of zirconium welded joints. *Svarochn. Proizvodstvo*, **1**, 45–48.
24. Vasilkov, V.I., Kislitsky, A.A., Onuchin, N.V. et al. (2002) On the causes for formation of defects in welds of E110 alloy made by electron beam welding and methods of controlling them. *The Paton Welding J.*, **5**, 36–38.
25. Babkin, L.T., Sukhov, K.K., Sannikov, D.V. et al. (1999) Sealing of fuel elements for nuclear reactors by flash-butt welding method. *Svarochn. Proizvodstvo*, **8**, 35–38.
26. Plyshevsky, M.I., Rassoshkina, N.S., Semyonov, A.N. et al. (2000) Friction welding of pipes of Zr–2.5Nb alloys. *Ibid.*, **1**, 9–12.
27. Blashchuk, V.E., Polyakov, S.G. (1997) Corrosion cracking of welded joints of zirconium alloy E125. *Avtomatich. Svarka*, **4**, 30–33.

TECHNOLOGICAL CAPABILITIES OF THE PROCESSES OF GAS-SHIELDED PULSED TWIN-ARC WELDING (REVIEW)

N.M. VOROPAJ, V.M. ILYUSHENKO and **V.A. MISHENKOV**
E.O. Paton Electric Welding Institute, NASU, Kiev, Ukraine

Pulsed twin-arc welding features separate feed of current pulses to electrically insulated consumable electrodes, the arcs of which form a common weld pool. This results in a relatively high (up to 30 kg/h) coefficient of electrode wire melting, high (up to 120 m/h) welding speed, and favourable butt and fillet weld formation. Prospects for further development of the tandem-arc welding processes are outlined.

Keywords: *twin-arc welding, current pulses, synergic control, shielding gases, power sources, welding modes, weld formation, welded joint properties*

Submerged multielectrode and multiarc welding are used to increase the efficiency of arc joining processes [1]. In the first welding process the electrodes are connected to one power source, and in the second process each of the electrodes is connected to a separate power source and the electrodes are electrically insulated from each other. Submerged multiarc welding is widely applied to produce longitudinal welds on pipes of a larger diameter [2–5]. To improve weld formation in submerged-arc welding at a higher speed the welding transformers are connected into a circuit ensuring arc current phase shift by 120° [4]. Attempts were made to achieve the stability of the twin-arc welding process due to protection of the arcs by CO_2 gas and their powering from one source [6, 7]. However, this welding process did not become widely accepted, in view of electromagnetic interaction between the arcs and intensive spattering of electrode metal.

In case of synergic control of the parameters of the modes of pulsed twin-arc welding for any electrode wire feed rate the amplitude and duration of current pulses and pauses, as well as base current values strictly correspond to the electrode melting rate [8]. This is accompanied by fine-drop transfer of electrode metal and its minimum spattering. Implementation of this process requires application of inverter power sources. Synergic control essentially reduces the time required for selection of optimum welding modes. It should be noted that the current pulse parameters are preprogrammed, allowing not only for the wire diameter and grade, but also shielding gas composition.

In this study features and technological capabilities of the processes of gas-shielded pulsed twin-arc welding are considered on the basis of generalized published data and results of the authors' own research.

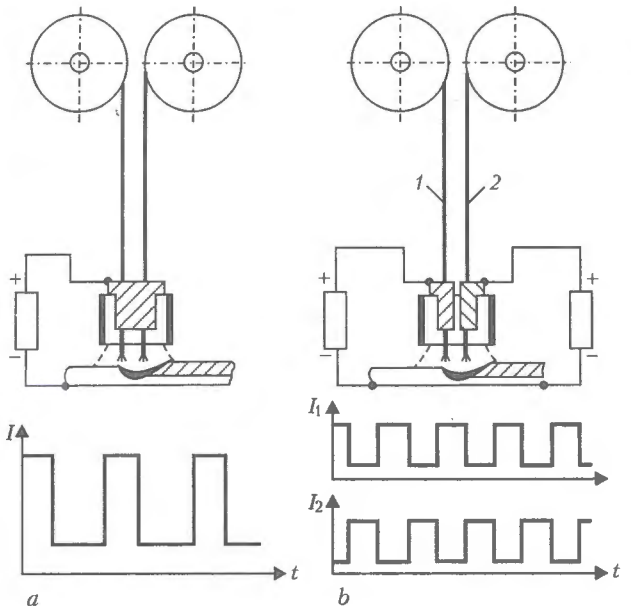

Figure 1. Schematic of pulsed processes of split-electrode (*a*) or twin-arc (*b*) welding: *1*, *2* — for designations see the text

Schematics of the processes of twin-electrode and twin-arc welding in inert and active gases and their mixtures are shown in Figure 1. In the first case (Figure 1, *a*) both the electrode wires are connected by a common current supply, and are powered from one source; and in the second case (Figure 1, *b*) electrode wires *1* and *2* have a separate current supply and are powered by two independent sources with a device for synchronizing their operation. Pulsed twin-arc processes developed over the recent years [9–15], are based on the application of all-purpose inverter-type power sources with microprocessor control of the current pulse parameters and electrode wire feed rate; the electrodes are mounted in a common gas-shielded nozzle.

In modern equipment for pulsed twin-arc welding a precision principle of ignition of both arcs is envisaged [9–14]. The current pulse is first applied to one electrode. The second arc is ignited later. If required, the welding process can start with two arcs running simultaneously. The same technological capabilities are also available at the end of welding. Welding parameters are continuously monitored and recorded starting from the moment of arc ignition and till the end of the process. The main equipment blocks are controlled by thirty or more programs. In twin-arc welding at 100 % duty cycle the inverter power sources provide up to 1000 A rated welding current. Electrode wire feed rate is up to 800 m/h.

In submerged twin-arc welding the electrode wire melting coefficient $K_{e.m}$ is equal to 20–23 kg/h at currents of 800 to 1000 A (Figure 2, region *1*) [15]. In the case of gas-shielded pulsed twin-arc welding it reaches 25 kg/h and more at 800 A currents (Figure 2, region *2*). Much smaller values of melting coefficients of solid and flux-cored wires are found in gas-shielded single-arc welding (Figure 2, regions *3* and *4*). For solid wire $K_{e.m}$ is equal to 10–15 kg/h at the currents

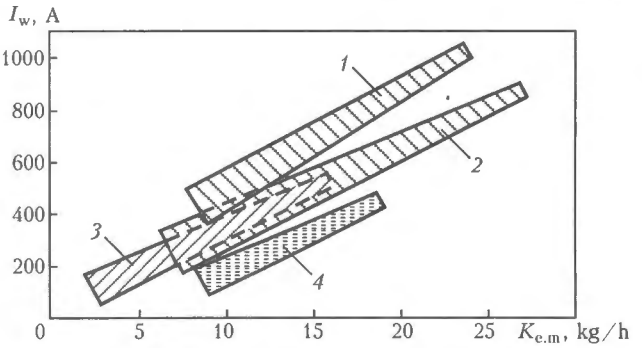

Figure 2. Dependencies of electrode wire melting coefficient on welding current: *1*, *2* — twin-arc welding using flux (*1*) and shielding gases (*2*); *3*, *4* — gas-shielded single-arc welding with solid and flux-cored wire, respectively

of 300–500 A. For flux-cored wires smaller welding current is required for the same value of $K_{e.m}$ [15].

The welds become narrower and base metal penetration becomes deeper due to longitudinal location of electrode wires (Figure 3, *a*) [14]. Opposite results were obtained in the case of a transverse location of electrode wires (Figure 3, *c*). At electrode wire location at an angle of 45° to the weld axis (Figure 3, *b*) welds of medium width and penetration depth are produced, and, in addition, probability of burn-through formation in the butt and overlap joints becomes lower.

Cloos Company (Germany) developed a torch for consumable-electrode twin-wire welding in inert and active gases [16]. Welding current is fed from computer-controlled GLC 853 source in the pulsed and continuous modes ($I_w \leq 1500$ and $I_w \leq 850$ A, respectively). Feed rate of both the wires is adjusted separately. Speed of welding 2 to 3 mm metal is up to 360 m/h. On thicker metal at melting efficiency of 24 kg/h a fillet weld with 8 mm leg can be made in one pass at 48 m/h speed.

System of KUKA Company (Germany) for robotic twin-electrode arc welding in active gas allows in-

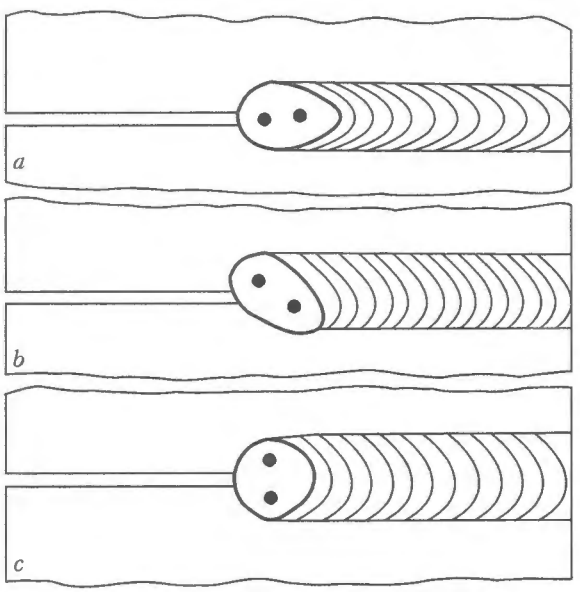

Figure 3. Schematic of electrode wire position in twin-arc welding: *a* — longitudinal, *b* — at 45° angle; *c* — transverse

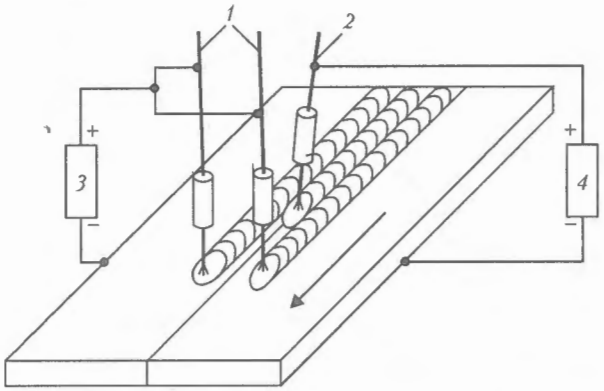

Figure 4. Schematic of a combined process of welding in Ar + CO_2 mixture with split (*1*) and inclined (*2*) electrodes with power supply from two sources (*3, 4*)

creasing the welding speed two times [17]. One of the used wires should have a larger diameter.

The authors [18] associate the effectiveness of consumable-electrode arc welding in inert or active gases with the use of two split electrode wires. Their simultaneous melting increases the efficiency of the welding process 2 times. This process, however, poses a number of serious problems. If two-arc welding with two separate current sources is used instead of two-electrode welding, metal spattering is reduced. In addition, weld appearance can be improved at a high welding speed. Two TPS 450 inverters are recommended as power sources (welding current is 900 A at 100 % duty cycle).

A system incorporating OI-126 power source was developed for pulsed gas-shielded consumable-electrode twin-arc welding. The system consists of a welding transformer, thyristorized power unit, control unit, panels for operating mode switching and current pulse distribution [19]. Electric circuit of the system allows performing a separate feed by the set program of one- and different-polarity current pulses to both the electrodes, and provides a smooth increase and lowering of welding current. Feeding of 1.2 to 2.0 mm dia. electrode wires is performed using separate drives. Compared to traditional technologies, the following advantages of the considered welding process were revealed: complete elimination of electromagnetic interaction of the arcs forming a common pool; narrowing of the heat-affected zone; sound formation of welds without technological backing; increase of cold resistance of welded joint metal on higher strength low-alloyed steels.

Technological features of consumable-electrode twin-arc welding of aluminium alloys, using two pulsed power sources TPS 2700 and TPS 450 of Fronius (Austria) are described in [20]. It is shown that at the same welding current on each of the electrodes twin-arc welding of aluminium alloys, compared to regular single-arc welding, enables increasing the metal penetration depth and decreasing the weld reinforcement height. In the author's opinion, twin-arc pulsed welding should be used to prevent burns-through of sheet metal in high-speed automated single-pass welding of butt and lock joints. This welding process is also acceptable for performance of tee and overlap joints, when large weld legs and deep metal penetration are required.

Pulsed twin-arc welding of aluminium alloys has the following technological features [20]: consumption of shielding gas (argon) of up to 15 l/min; electrode wire diameter of 1.2 mm; 8 to 10 mm distance between the wires; current pulse frequency of 45 to 200 Hz; their duration of 1 to 3 ms and amplitude of 380 to 520 A; wire feed rate of 780 m/h.

Wires of two different grades, namely Sv-AK5 and Sv-1201, are used simultaneously for welding and surfacing of cast aluminium alloys.

Gas-shielded thee-arc welding by one split vertical and one inclined electrode was performed with power supply from two separate power sources (Figure 4). It is rational to apply such a process in welding butt welds to reduce the penetration depth during the first layer deposition or in performance of surfacing operations. Minimum distance between the arcs determines the length and width of the weld pool, and the maximum distance determines the quality of weld formation and deposited metal. Two variants of three-arc welding are distinguished, namely into a common weld pool and into separate pools. In the latter case, the adjacent arc melts the already solidified layer, deposited with the previous arc.

To improve the economic indices in construction of the oil and gas pipelines under the North conditions, the Scientific-Technical Center of Welding of Cranfield University in Great Britain used gas-shielded consumable-electrode pulsed twin-arc welding [21]. As welding equipment for these purposes, the University specialists selected a system, developed by Fronius. It includes TPS-4000R power sources, wire feed devices VR1500 and special welding software. Welding sources are powered by a diesel-generator. Each welding unit is fitted with two torches with arcs, located consecutively at 70 mm distance from each other. Welding performed with two pairs of arcs allows producing circumferential welds at up to 20 m/h speed, in particular, in construction of the Alyaska pipeline. Application of a traditional technology of single-arc welding required 19 welding stations. Performance of twin-arc welding using Fronius equipment requires only four stations, thus providing a cost-saving of 150 mln USD.

The essence of the combined plasma-arc process suggested in [22], consists in that at connection of an additional arc, a redistribution of current from the consumable-electrode power source between the plasma and consumable electrode occurs, resulting in current increase in the consumable electrode, reduction of heat input into the base metal and more intensive melting of the electrode wire. In the presence of a pilot arc the stability of running of an intermediate arc between the plasmatron and the wire becomes higher. However, the above process is characterized by an unstable rate of electrode wire melting, greater metal spatter and unfavourable weld formation.

The process of spot plasma-arc welding with separate adjustment of item penetration and crater welding up does not have the above disadvantages [23]. It is established [24] that the optimum parameters of the welding mode (welding current, arc voltage, plasma-gas consumption, plasma and arc running time) should be preprogrammed, depending on the thickness of metal being welded, electrode wire diameter, shielding gas consumption and type. Sound overlap joints of metal up to 5 mm thick can be produced as a result of complete penetration of the upper sheet by the plasma and its subsequent fusion with the lower element due to the use of the consumable-electrode arc. Duration of alternating pulses of the plasma and arc current is equal to 3–12 s.

In Germany a specialized PSW-500 unit has been developed for spot plasma and arc welding without using filler wire [25]. The unit offers significant advantages, compared to equipment for resistance spot and laser welding, i.e. lower equipment cost and possibility of one-side access to the item being welded. Spot welds are produced by melting of the upper and lower elements of the overlap joint. The plasma arc melts the part by alternating current pulses. Special focusing of the arc allows reducing the HAZ width. The unit is suitable for welding carbon and alloyed steels, aluminium, copper and its alloys up to 2.5 mm thick. Welding can be performed manually, by automatic machines and robots. The robotic unit with the device for spot plasma welding is successfully used in batch-production of metal structures consisting of hollow bent and stamped elements [26].

PWI developed a combined process of twin-arc welding and surfacing, which envisages alternative and separate forming of the arcs on nonconsumable and consumable electrodes with formation of a common pool of molten metal [27]. The arc on the nonconsumable (tungsten) electrode is powered by current pulses of different polarity with prevailence of a straight polarity component. The role of the arc on the nonconsumable electrode is reduced to base metal penetration to the specified depth. Consumable electrode melting and cathode cleaning of the metal surface from oxide films proceed under the impact of reverse polarity current pulses. Technology of pulsed twin-arc surfacing of pistons from aluminium alloys of different alloying systems, applied in the automotive and tractor internal combustion engines, has been optimized [28]. Deposited metal alloying provides a significant increase of its wear resistance. Operating life of deposited pistons increases 2 to 2.5 times, compared to unstrengthened pistons.

A novel process of microplasma welding by different polarity current pulses was also proposed [29]. It consists in that voltage pulses positive relative to the item are applied to the plasmatron nozzle for cathode breaking up of oxide films on the metal being welded. In the intervals between them, negative pulses are applied to the tungsten electrode, resulting in the straight polarity plasma arc ignition between the electrode and the item. Plasma gas (argon) is fed into the circular gap between the tungsten electrode and nozzle; shielding gas (usually, helium) — into the gap between the plasma and shielding nozzle. This process is used in welding thin aluminium alloys. Technology of highly efficient wide-layer surfacing with several electrode wires and strips turned out to be efficient [30].

The above examples by far do not limit the technological capabilities and spheres of pulsed twin-arc welding application. In the future new developments are anticipated in the field of highly-efficient tandem-processes and means of their implementation.

CONCLUSIONS

1. Features of the processes of consumable-electrode pulsed twin-arc welding in the atmosphere of inert gases and gas mixtures are determined by independent and alternative powering of the arcs by current pulses of an adjustable amplitude, duration and frequency. A separate feed of electrode wires and the arc running in a common weld pool are envisaged at longitudinal, inclined or transverse position of the electrodes.

2. Processes of pulsed twin-arc welding are based on the use of inverter power sources with the synergic system of control of mode parameters and two-electrode torch. The latter enables smooth adjustment of the distance between the axes of current-conducting nozzles. Optimum modes of twin-arc welding are preprogrammed allowing for electrode wire grade and diameter, shielding gas flow rate and composition. Synergic control is currently implemented only for consumable-electrode pulsed-arc welding in inert gases or their mixtures without short-circuiting of the arc gap.

3. For the case of carbon and alloyed steels, the following technological advantages of pulsed twin-arc welding were revealed: greater depth of base metal penetration; narrower HAZ; improved weld formation at high speeds; increased mechanical properties of welded joints. A disadvantage of gas-shielded pulsed twin-arc welding is a higher emissivity of both the arcs, as well as a higher cost of welding equipment and considerable cost of its operation and repair.

1. (1974) *Technology of fusion electric welding of metals and alloys*. Ed. by B.E. Paton. Moscow: Mashinostroenie.
2. Mandelberg, S.L. (1965) Higher speed multiarc welding with transverse oscillation of the electrode. *Avtomatich. Svarka*, **2**, 8–13.
3. Mandelberg, S.L. (1966) Magnetic interaction of the arcs in twin-arc higher speed welding. *Ibid.*, **4**, 30–36.
4. Paton, B.E., Mandelberg, S.L., Sidorenko, B.G. (1971) Some peculiarities of weld formation in higher speed welding. *Ibid.*, **8**, 1–6.
5. Sidorenko, B.G., Mandelberg, S.L. (1988) Selection of optimum number of electrodes in multiarc higher speed welding. *Ibid.*, **2**, 53–55.
6. Mandelberg, S.L., Bogachek, Yu.L. (1968) Twin-arc CO_2 welding. *Ibid.*, **9**, 72–73.
7. Fajnberg, L.I., Rybakov, A.A., Mandelberg, S.L. (1975) Twin-arc CO_2 higher speed welding. *Ibid.*, **2**, 35–38.
8. Voropaj, N.M., Ilyushenko, V.M., Lankin, Yu.N. (1999) Specifics of pulse-arc welding with synergetic control of parameters (Review). *Ibid.*, **6**, 26–32.

9. (2003) TIME TWIN as an efficient welding method (2003) *Ibid.*, **4**, 39–42.
10. (1988) New technological process of «Fronius» Company. *Ibid.*, **2**, 69–70.
11. (1996) MIG/MAG – Hochleistungsschweissen mit Tandem Technik. *Schweiss. und Pruftechnik*, **9**, 150.
12. Hackl, H. (1997) TIME TWIN – Schneller MSG – Schweissen mit zwei Drahtelektroden. *Ibid.*, **5**, 71–73.
13. Ishchenko, A.Ya., Voropaj, N.M., Budnik, V.P. et al. (2000) Technological capabilities of the process of double-sided welding of aluminium alloys. *The Paton Welding J.*, **1**, 42–44.
14. Killing, R. (1997) Das MAG – Mehrdrahtschweissen. *Praktiker*, **6**, 243–245.
15. Andersson, I., Tolf, I., Hedegard, I. (2004) Tandem MIG-MAG Vaxez sig starkare. *Svetsen*, **2**, 7–11.
16. (1996) Soldadura MIG/MAG con doble hilo. *Met. y Elec.*, 60(**6**), 44–45.
17. (1996) KUKA two-wire MAG welding system doubles welding speeds. *Ind. Robot*, 23(**6**), 42.
18. (1997) Bessere Schweissqualitaet. *Stahlmarkt*, 47(**7**), 52.
19. Voropaj, N.M., Protsenko, P.P. (2000) Features of weld and HAZ formation in gas-shielded pulsed twin-arc welding in high-strength low-alloyed steels. *The Paton Welding J.*, **8**, 40–46.
20. Ishchenko, A.Ya., Mashin, V.S., Pashulya, M.P. (2005) Technological features of twin-arc consumable electrode pulsed welding of aluminium alloys. *The Paton Welding J.*, **1**, 10–14.
21. (2005) Automated pipeline welding. *Ibid.*, **1**, 46–49.
22. Zhaing, M., Jiang, M., Lu, W. (2004) Double electrod improve GMAW heat input control. *Welding J.*, **11**, 39–41
23. Voropaj, N.M. (2004) Specifics of arc spot shielded-gas we ding processes (Review). *The Paton Welding J.*, **7**, 28–33.
24. Voropaj, N.M., Ilyushenko, V.M., Mishenkov, V.A. (2004 Combined process of spot plasma-arc welding. *Svarshchik* **4**, 26, 27, 29.
25. (2003) Plasmapunktschweissen mit dem Plasma Spo Welder. *Schweissen und Schneiden*, **5**, 224–225.
26. (2004) Plasmapunktschweissen im Serieneinsatz. *Ibid.*, **12** 642–643.
27. Voropaj, N.M., Lesnykh, V.V., Mishenkov, V.A. (1996) Twin-arc surfacing of aluminium pistons by a combined non consumable and consumable electrode. *Avtomatich. Svarka*. **6**, 21–25.
28. Voropaj, N.M., Lesnykh, V.V., Mishenkov, V.A. (1994) Combined process of twin-arc consumable- and nonconsumable electrode welding and surfacing. *Ibid.*, **4**, 56–57.
29. Paton, B.E., Voropaj, N.M., Gvozdetsky, V.S. (2002) A system for mechanized microplasma welding of honeycomb aluminium metal structures. *The Paton Welding J.*, **3**, 32–36.
30. Ryabtsev, I.A. (2005) High-efficiency wide-layer surfacing using electrode wires and strips (Review). *Ibid.*, **6**, 31–35.

FEATURES OF ASSEMBLY AND MULTIPASS WELDING OF CIRCUMFERENTIAL BUTT JOINTS ON THICK-WALLED SHELLS

I.A. TARARYCHKIN
East-Ukrainian National University, Lugansk, Ukraine

Considered are the features of systematic deviations of groove geometry in case of errors of assembly for welding of circumferential butt joints on thick-walled shells. It is proposed to compensate for deviations observed around the butt perimeter by a programmed change of the electrode wire feed rate in multipass welding. Regularities of variation of the wire feed rate for different types of joints are established.

Keywords: *automatic welding, thick-walled shells, multipass weld, edge preparation, assembly errors, defects, mode parameters, groove filling algorithm*

In manufacture of chemical apparatuses, heat exchangers and steam generators there is a need to weld circumferential butt joints on thick-walled shells [1, 2]. In study [3] it is noted that in welding of large-sized thick-walled butt joints the quality of welded joints is due to the accuracy of joint assembly, and lack of algorithms and programs for groove filling is the main hindrance for automation of multipass welding of thick metal under the conditions of considerable variation of the accuracy of fit-up and geometrical parameters of the groove.

Accuracy of fit-up of circumferential butt joints is characterized by angle φ, formed by their longitudinal axes (Figure 1). Fit-up errors lead to a situation, when the groove section of a minimum area will be filled first of all in welding in the modes which do not change within one rotation of the shell, the opposite section being only partially filled. For instance, for a circumferential butt joint of a shell with 120 mm wall thickness (Figure 2) the fit-up tolerance range is equal to 3 mm. If there is no gap in one of the sections, and it is equal to 3 mm in the opposite section, variation of groove geometry around the butt perimeter will result in that after complete filling of the section with a zero gap, the level of groove filling in the opposite section will be 104.5 mm. If the height of an individual layer is about 4 mm, filling the remaining part of the groove will require deposition of four more layers. Multiple interruption and restarting of the welding process in this case can be accompanied by formation of process defects in the weld.

Thus, provision of a groove filling level constant around the butt joint perimeter, despite the fit-up errors, is a mandatory condition for producing sound circumferential welded joints.

A constant level of metal layer in the groove can be ensured in the case, if variation of the deposition area of individual beads around the circumferential butt perimeter compensates the observed change of

Table 1. Admissible value of the characteristics of groove geometry for butt joints of different types

Joint type	δ, *mm*	a_{max}, *mm*	a_{min}, *mm*	*Tolerance range for gap in the butt, mm*	α/2, *deg*
C19, C20	20–30	6.5	3.5	3	25 ± 3
C34	40–60	2	0	2	10 ± 1
C35	40–50	2	0	2	10 ± 2
C36	Up to 60	3	1	2	13 ± 2
C37	Up to 60	2	0	2	13 ± 2

the cross-sectional area of the layer. This kind of schematic of the groove filling will further on be regarded as a compensation schematic, and its implementation requires establishing the main regularities of formation of systematic deviations from groove geometry, arising in assembly and welding of circumferential welds.

The purpose of this study is analysis of the features of formation of systematic deviations from the groove geometry, due to errors of fit-up of circumferential butts on thick-walled shells, and development of an algorithm of their compensation in automatic multipass arc welding.

Position of the current cross-section of the groove during welding can be characterized by angle θ, if we take the section for which the assembly gap in the butt is minimum as the point of origin (θ = 0). Then the position with the maximum groove area is defined as θ = π.

Rotation of a shell assembled for welding, will be accompanied not only by a systematic variation of the assembly gap in the butt from a_{min} to a_{max} for sections θ = 0 and θ = π, but also by a change of groove angle in the range from α − φ to α + φ (see Figure 1). Table 1 gives the data on tolerance ranges for assembly gaps and groove angles for one-sided welded joints, in keeping with the requirements of GOST 8713–79. For the range of values of shell inner diameter d = = 0.5–2.0 m the admissible values of angle φ are given in Table 2. The largest value of angle φ/2 facing one edge is equal to 0.17°, which is characteristic for joints of types C19, C20, and turns out to be negligibly small, compared to the tolerance range for angle α/2 = 25 ± 3° (see Table 1).

Thus, variation of groove angle around the butt perimeter as a result of fit-up errors can be neglected further on, and data given in Figure 3 can be used as a design schematic, describing the features of variation of groove geometry at its filling by layers of a constant height. Variation of the area of an individual layer around the groove perimeter can be evaluated by considering two opposite sections, namely θ = 0 and θ = π (Figure 3). If the height of each layer remains constant (h = const), for k-th layer the ratio of maximum area F_k^+ to minimum F_k^- has the form of

$$W_k = \frac{F_k^+}{F_k^-} = \frac{a_{max} + h(2k-1)\,\mathrm{tg}\,\frac{\alpha}{2}}{a_{min} + h(2k-1)\,\mathrm{tg}\,\frac{\alpha}{2}}.$$

Table 2. Admissible values of angle φ (deg) for butt joints of various types

Joint type	*d, m*		
	0.5	*1.0*	*2.0*
C19, C20	0.34	0.17	0.09
C34, C35, C36, C37	0.23	0.11	0.06

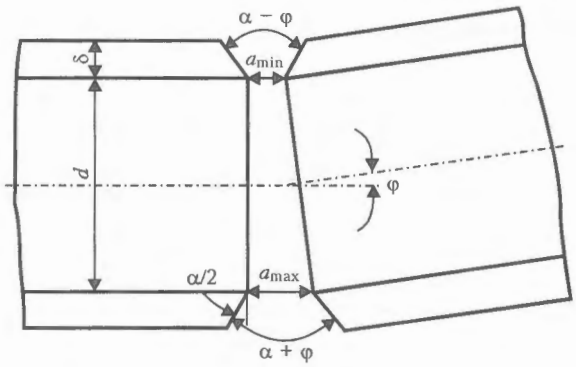

Figure 1. Schematic of fit-up of a circumferential butt joint of a shell

As is seen from Table 3, for joints of C19, C20 type W_k reaches the largest value in the first layer (W_1 = 1.57). This means that process equipment for welding of such a butt joint should enable increase of the deposition area by not less than 60 %.

Calculation procedure shown in Figure 4 can be used to demonstrate that the size of the gap in the butt joint varies by a harmonic law at shell revolution:

$$a(\theta) = a_{min} + 0.5(a_{max} - a_{min})(1 - \cos\theta).$$

$W_k(\theta)$ dependence for different groove shapes allows establishing the law of variation of the area of individual bead deposition at sequential filling of a circular groove by a multipass weld. For grooves given in Figure 3, this ratio has the form of

$$W_k(\theta) = 1 + \frac{0.5(a_{max} - a_{min})\,(1 - \cos\theta)}{a_{min} + h(2k-1)\,\mathrm{tg}\,\frac{\alpha}{2}}.$$

The dependence shows how many times the area of deposition of an individual bead in k-th layer should be increased at shell rotation through angle θ, compared to initial position, for which the assembly gap in the butt is minimum.

Let us consider a joint of C19 type at shell wall thickness δ = 28 mm. Assuming the number of depos-

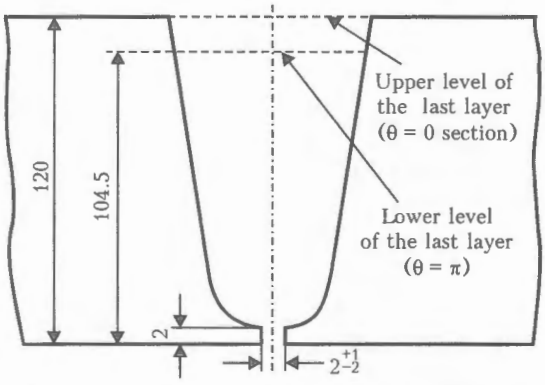

Figure 2. Schematic of formation of a layer level non-uniform along the groove height as a result of fit-up errors

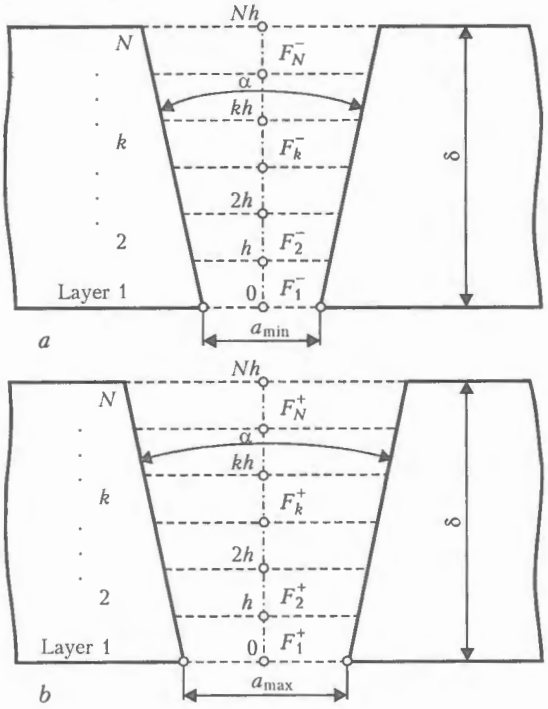

Figure 3. Design schematic for determination of the ratio of layer area in different groove cross-sections: *a* — θ = 0 section; *b* — θ = π

ited layers $N = 6$, the height of individual layer $h = 4.42$ mm (see Table 3). As is seen from Figure 5, the deposition area of individual beads should be varied to the greatest extent in welding of the first layer. As the groove is filled (with increase of k values), the difference in the deposition areas for opposite sections θ = 0 and θ = π decreases, and $W_k(\pi)$ value drops from 1.54 for $k = 1$ to 1.12 for $k = 6$. Considering the root face and the need to fill the gap with filler metal, value $W_1(\pi) = 1.62$ (for C19 joint) and 1.60 (for C20) (Figure 5, *b*).

In analysis of the combined shape of the groove, the lower and upper parts should be regarded separately. If the lower part is filled using two layers, the dependence has the form of

$$W_k(\theta) = 1 + \frac{0.5(a_{max} - a_{min})(1 - \cos\theta)}{a_{min} + \Omega_k}.$$

Ω_1 and Ω_2 values (Figure 6) depend only on the shape of the groove lower part. When filling the groove upper part Ω_k values ($k = 3, 4, \ldots, N$) should

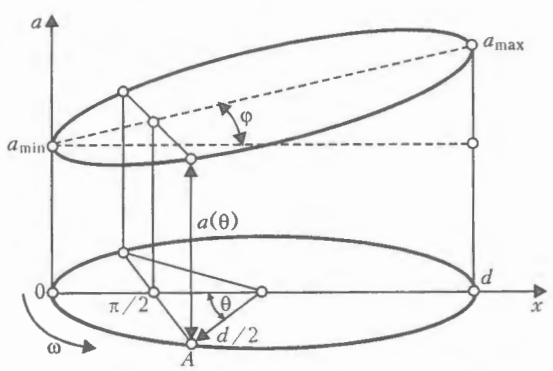

Figure 4. Design schematic for determination of the current gap in the butt $a(\theta)$ at rotation of shells assembled for welding through angle θ from the initial position

Table 3. Design values of W_k for butt joints with a V-shaped groove for C19 and C20 types

Layer number k	*N = 7, h = 3.79 mm*	*N = 6, h = 4.42 mm*	*N = 5, h = 5.3 mm*
1	1.57	1.54	1.50
2	1.34	1.31	1.28
3	1.24	1.22	1.19
4	1.19	1.17	1.14
5	1.16	1.14	1.12
6	1.13	1.12	–
7	1.11	–	–

Note. $a_{min} = 3.5$ mm; $a_{max} = 6.5$ mm; δ = 28 mm.

be assumed in keeping with the data of Table 4. It should be noted that $W_k(\theta)$ parameter varies by a harmonic law for any groove shape and layer number k. Thus, if as a result of control operations $a_{min} = 0.2$ mm and $a_{max} = 1.8$ mm values were established for a circumferential butt of a 48 mm thick shell, assembled for welding (C35 joint), then for $k = 1$ and 2 $W_k(\theta)$ parameter has the form of

$$W_1(\theta) = 1 + 0.12(1 - \cos\theta),$$
$$W_2(\theta) = 1 + 0.05(1 - \cos\theta),$$

and for $k = 3, 4, \ldots, N$

$$W_k(\theta) = 1 + \frac{0.8(1 - \cos\theta)}{16 + 0.18h(2k - 5)}.$$

As is seen from Figure 7, irrespective of groove shape, the most significant correction of mode parame-

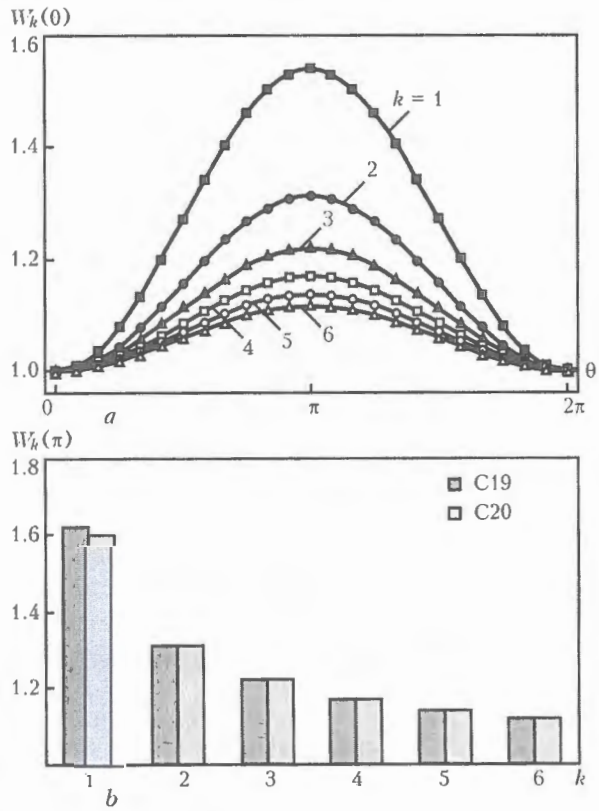

Figure 5. Design values $W_k(\theta)$ for joints of C19 type (*a*) and $W_k(\pi)$ dependencies on layer number k for admissible values of the gap in the butt $a_{max} = 6.5$ mm and $a_{min} = 3.5$ mm (*b*)

Table 4. Ω_k values for the upper part of a combined groove for different types of the joints

Joint type	δ, *mm*	Ω_k (k = 3, 4, ..., N), *mm*
C36, C37	≤ 60	$16 + 0.23h(2k - 5)$
C34	≤ 40	$11.7 + 0.21h(2k - 5)$
	40–60	$15.8 + 0.18h(2k - 5)$
C35	≤ 40	$11.7 + 0.21h(2k - 5)$
	40–60	$15.8 + 0.18h(2k - 5)$

ters around the groove perimeter is required in welding the first layer. In this case the greatest variation of the first layer bead deposition area is characteristic for step-like groove (~ 80 %), and the least — for U-shaped groove (~ 30 %).

Change of the bead deposition area during groove filling is possible as a result of a simultaneous or separate variation of welding speed v_w and electrode wire feed rate v_f. The bead deposition area f and welding mode parameters are connected by the following dependence [3]:

$$f = \frac{\pi d_e^2}{4} \frac{v_f}{v_w} (1 - \psi_L),$$

where d_e is the electrode wire diameter; ψ_L is the coefficient of electrode metal losses.

As in circumferential butt welding the angular speed of the shell rotation remains constant (ω = = const), gradual vertical displacement of the torch from layer to layer is accompanied by an increase of welding speed. In welding of a shell of 1 m diameter

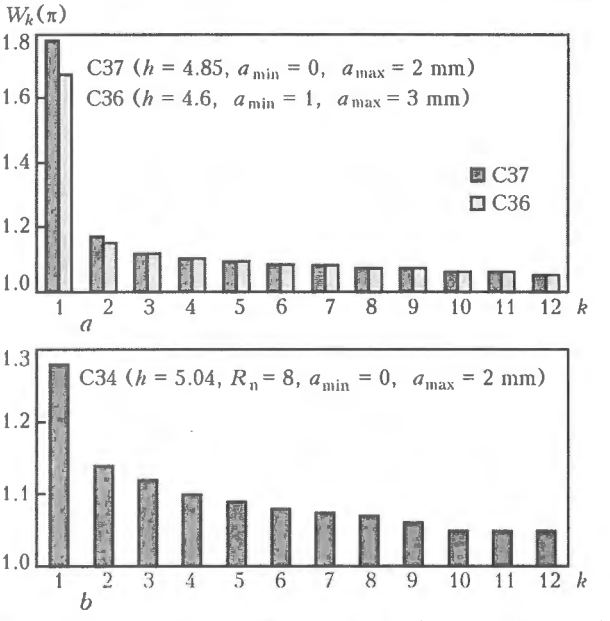

Figure 7. $W_k(\pi)$ dependence on layer number (N = 12, δ = 58 mm) for step-like (*a*) and U-shaped (*b*) groove

and 100 mm wall thickness, the welding speed will rise by approximately 12 % at transition from the first to the last layer. Therefore, the law of electrode wire feed variation should be related not only to variation of groove geometry within one layer, but also to the observed systematic variation of the welding speed at transition from layer to layer.

Welding speed during performance of the first layer of the circumferential weld $v_1 = 0.5\omega d$, and that of k-th layer

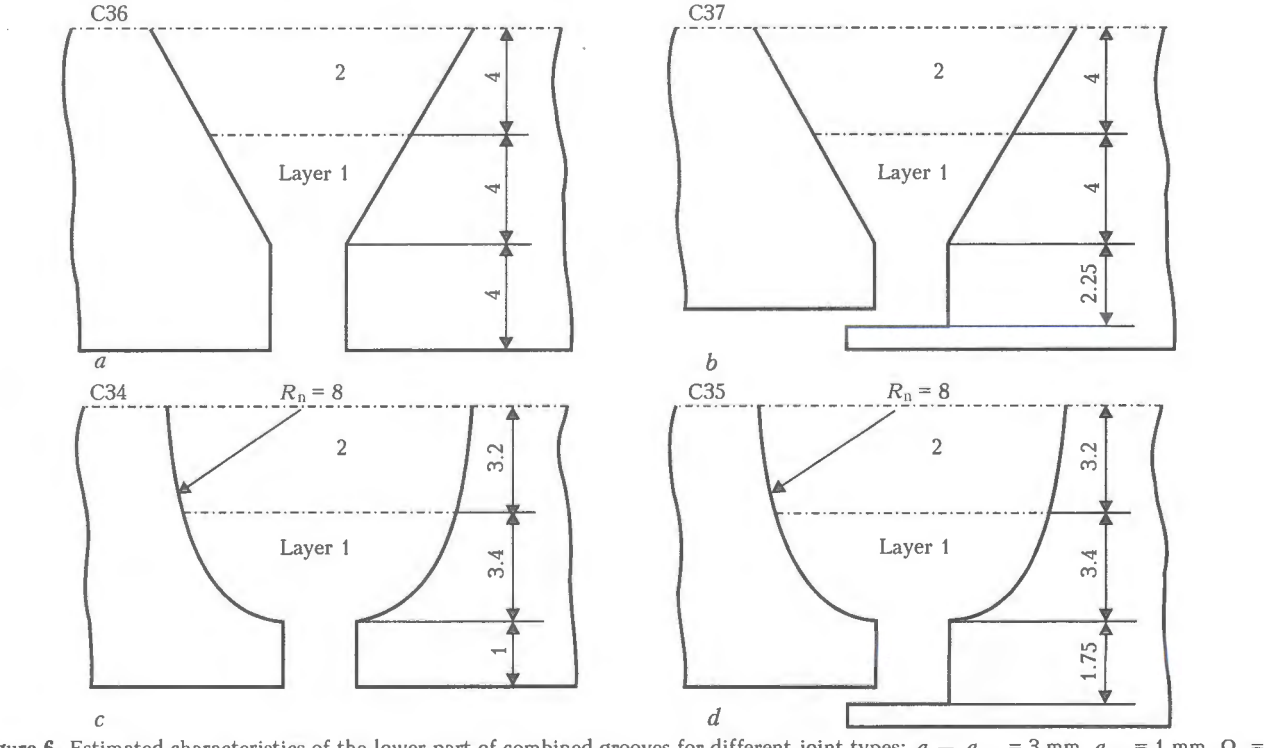

Figure 6. Estimated characteristics of the lower part of combined grooves for different joint types: *a* — a_{max} = 3 mm, a_{min} = 1 mm, Ω_1 = = 2 mm, Ω_2 = 12 mm, $W_1(\pi)$ = 1.67, $W_2(\pi)$ = 1.15; *b* — a_{max} = 2, a_{min} = 0, Ω_1 = 2.56, Ω_2 = 12, $W_1(\pi)$ = 1.78, $W_2(\pi)$ = 1.17; *c* — a_{max} = 2, a_{min} = 0, Ω_1 = 7.27, Ω_2 = 14.7, $W_1(\pi)$ = 1.28, $W_2(\pi)$ = 1.14; *d* — a_{max} = 2, a_{min} = 0, Ω_1 = 6.21, Ω_2 = 14.7, $W_1(\pi)$ = 1.32, $W_2(\pi)$ = 1.14

Table 5. Calculated values of Λ_k coefficient for shells of 0.5 and 2 m diameter with different thickness of the wall

Layer number k	*C19, C20* $N = 6$, $\delta = 28$ mm, $h = 4.42$ mm		*C36* $N = 12$, $\delta = 58$ mm, $h = 4.6$ mm		*C37* $N = 12$, $\delta = 58$ mm, $h = 4.85$ mm		*C34* $N = 12$, $\delta = 58$ mm, $h = 5.04$ mm	
	d, mm							
	0.5	*2.0*	*0.5*	*2.0*	*0.5*	*2.0*	*0.5*	*2.0*
1	1	1	1	1	1	1	1	1
2	1.04	1.01	1.05	1.01	1.04	1.01	1.03	1.01
3	1.06	1.02	1.07	1.02	1.06	1.01	1.05	1.01
4	1.08	1.02	1.09	1.02	1.08	1.02	1.07	1.02
5	1.10	1.02	1.10	1.03	1.10	1.02	1.09	1.02
6	1.11	1.03	1.12	1.03	1.11	1.03	1.11	1.03
7	–	–	1.14	1.04	1.14	1.03	1.13	1.03
8	–	–	1.16	1.04	1.15	1.04	1.15	1.04
9	–	–	1.18	1.04	1.17	1.04	1.17	1.04
10	–	–	1.20	1.05	1.19	1.05	1.19	1.05
11	–	–	1.21	1.05	1.21	1.05	1.21	1.05
12	–	–	1.23	1.06	1.23	1.06	1.23	1.06

$$v_k = \omega[0.5d + \delta - h(N - k)] \ (k = 2, 3, \ldots, N)$$

or

$$v_k = v_1 \Lambda_k,$$

where

$$\Lambda_k = 1 + \frac{\delta - h(N - k)}{0.5d}.$$

Accordingly, we assume $\Lambda_1 = 1$ for $k = 1$.

Λ_1 coefficient shows how many times will the welding speed increase during deposition of k-th layer compared to the first layer, if all the layers have height h in the upper part. As is seen from Table 5, increase of welding speed can be more than 20 % in some cases.

Area of the bead deposited in the k-th layer is

$$f_k = \frac{\pi d_e^2}{4}(1 - \psi_L)\frac{v_f}{v_1 \Lambda_k}.$$

Law of variation of electrode wire feed rate during filling of the groove has the following form:

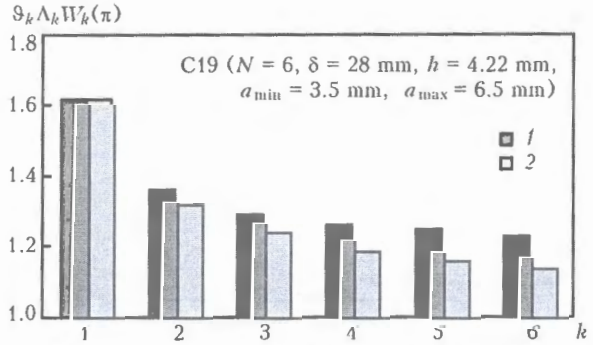

Figure 8. Dependence of $\vartheta_k \Delta_k W_k(\pi)$ product on layer number k for shells of 0.5 (*1*) and 2 (*2*) m diameter

$$v_f(k, \theta) = \frac{4 f_1 v_1}{\pi d_e^2 (1 - \psi_L)} \vartheta_k \Lambda_k W_k(\theta),$$

where f_1 is the bead deposition area in the initial section of the first layer; $\vartheta_k = f_k / f_1$ is the characteristic of the initial section of the groove that shows how many times the area of the bead deposited in the k-th layer is greater than that deposited in the first layer.

Thus, in multipass welding of circumferential butt joints on thick-walled shells the optimum strategy consists in filling the groove by layers of a constant height with mode parameters variable within each layer by a harmonic law.

$\vartheta_k \Lambda_k W_k(\pi)$ product shows how many times the electrode wire feed rate should be increased in a section with maximum assembly gap $\theta = \pi$ during deposition of the k-th layer, compared to the initial section of the first layer ($\theta = 0$, $k = 1$).

Figure 8 gives the calculation dependencies of $\vartheta_k \Lambda_k W_k(\pi)$ product on layer number k for shells of 0.5 and 2 m diameter with one-sided V-shaped groove, filled by layers of a constant height, while all the beads in the initial section have a constant deposition area ($\vartheta_k = 1$). Assumed values of maximum and minimum gap in the butt correspond to the limit admissible values for a joint of C19 type (see Table 1).

As increase of welding speed for a shell of 28 mm thickness does not exceed 11 % (Table 6), and all the beads in the initial section have the same area, the established law of wire feed variation allows to mostly compensate the observed variation of the cross-sectional area of an individual layer around the groove perimeter. However, the schematic of bead layout accepted for this case, has a number of significant disadvantages related to the complexity of ensuring the welded joint quality. The variant of groove filling when the cross-sectional area of individual beads f_k

Table 6. Calculated values of multipass welding parameters (joint of C37 type, v_i = 6 mm/s, d_e = 3 mm, $(1 - \psi_L) = 0.98$, d = = 0.5 m, N = 12, δ = 58 mm, h = 4.85 mm, a_{min} = 0.6 mm, a_{max} = 1.8 mm)

Layer number k	*Bead number in k-th layer* S_k	*Bead area in the k-th layer of initial section* f_k, mm^2	$\frac{4f_1 v_1 \vartheta_k \Lambda_k}{\pi d_e^2 (1 - \psi_L)}$, *mm/s*	*Law of variation of electrode wire feed rate* $v_f(k, \theta)$, *mm/s*	*Maximum wire feed rate in k-th layer* $v_f(k, \pi)$, *mm/s*
1	1	19.75	17.10	20.35 – 3.25 cos θ	23.60
2	2	25.20	22.74	23.88 – 1.14 cos θ	25.02
3	3	28.60	26.33	27.23 – 0.9 cos θ	28.13
4	3	32.20	30.09	30.99 – 0.9 cos θ	31.89
5	3	35.90	34.20	35.12 – 0.92 cos θ	36.04
6	4	29.60	28.56	29.27 – 0.71 cos θ	30.00
7	4	32.30	31.81	32.51 – 0.7 cos θ	33.21
8	4	35.00	34.88	35.61 – 0.73 cos θ	36.34
9	5	30.17	30.61	31.19 – 0.58 cos θ	31.77
10	5	32.33	33.35	33.95 – 0.6 cos θ	34.55
11	5	34.50	36.25	36.87 – 0.62 cos θ	37.49
12	6	30.60	32.66	33.18 – 0.52 cos θ	33.70

remains unchanged for the initial section only within one layer, should be considered to be preferable.

Figure 9, *a* gives the dependence of $\vartheta_k \Lambda_k W_k(\pi)$ product on layer number k for shells of 0.5 and 2 m diameter with layer thickness δ = 58 mm. Schematic of bead layout corresponds to the data in Figure 9, *b*, where S_k is the number of beads in the k-th layer with deposition area $f_k = F_k/S_k$. Here f_k = const is assumed for the initial section within an individual layer. It is seen that the accepted schematic of groove filling is related to the need to increase the electrode wire feed rate during groove filling more than 3 times.

The problem of selection of the optimum groove filling schematic does not have an unambiguous solution [3]. Therefore, depending on specific conditions of fit-up, the groove may be filled using different schematics. The required range of electrode wire feed rate variation should be ensured by the available process equipment. For instance, if after fit-up of 0.5 m dia. shell, a_{min} = 0.6 mm and a_{max} = 1.8 mm values of the gap in the butt were established by the results of control operations for C37 joint, they are regarded to be admissible in keeping with GOST 8713–79 (see Table 1).

The welding process should be started having mounted the shell in a position, in which the arc is ignited in the initial section with a minimum gap θ = = 0. Calculation results and recommended schematic of groove filling for this case are given in Table 6, which also gives the algorithm which should be used to vary the electrode wire feed rate in welding. In addition, the maximum and minimum rate of electrode wire feed ($v_{f\,min}$ = 17.1, $v_{f\,max}$ = 37.49 mm/s) can be specified for the accepted schematic of groove filling, thus specifying the requirements to the used welding equipment.

Thus, proceeding from the compensation approach, the proposed design dependencies allow solving the problem of ensuring the quality of circumferential welds on thick-walled shells by a preliminary selection of the bead layout schematic and programmed change of the welding mode parameters in multipass welding.

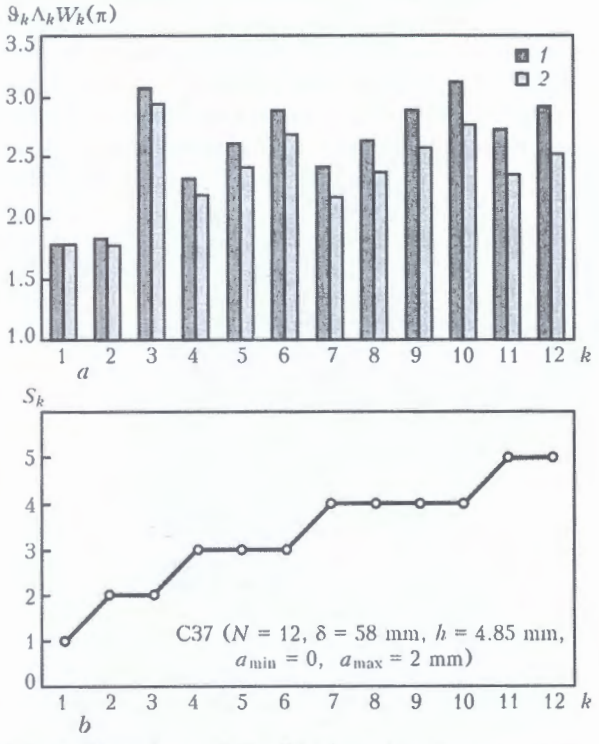

Figure 9. Dependence of $\vartheta_k \Delta_k W_k(\pi)$ product on layer number k for shells of diameter of 0.5 (*1*) and 2 (*2*) m (*a*), and respective S_k–k diagram describing the schematic of groove filling (*b*)

1. Pankov, V.V., Chernyshev, G.G., Kozlov, N.E. (1987) Mathematical model of optimization of multipass submerged-arc welding of power unit housing equipment. *Svarochn. Proizvodstvo*, 7, 34–37.
2. Kurkin, S.A., Khovov, V.M., Rybachuk, A.M. (1989) *Technology, mechanization and automation of welded structure fabrication*. Atlas. Moscow: Mashinostroenie.
3. Berezovsky, B.M. (2003) *Mathematical models of arc welding*. Vol. 2: Mathematical modeling and optimization of formating different type welds. Chelyabinsk: YuUrGU.

LIGHT-BEAM WELDING AND BRAZING (REVIEW)

A.M. ZHADKEVICH
E.O. Paton Electric Welding Institute, NASU, Kiev, Ukraine

Retrospective analysis of development of the light-beam heating method is given. The leading role of Russian scientists in formation of this area is highlighted. It is noted that the light-beam heating method can be applied for welding and brazing of various materials, as well as for heat treatment of parts. Advantages of welding using the light beam are given in comparison with those of arc welding.

Keywords: *light beam, light-beam heating, welding, brazing, heat treatment*

Light-beam technologies are increasingly applied in the industry, particularly for melting and joining of metals, and in the last years for producing materials with nanostructures. This work features retrospective review of the development of technologies and application of light beam in the processes of welding and brazing [1]. The K.E. Tsialkovsky Moscow Aviation Technological Institute (MATI) plays a leading role in development of this direction. As early as in 1967–1968 G.D. Nikoforov and M.I. Oparin initiated studies on evaluation of a possibility and efficiency of using focused energy of a light beam of incoherent light sources for technological purposes (welding, brazing and heat treatment) [2, 3]. Electron beam and laser welding was used to study a possibility for development of energy sources (light-beam modules) and optimization of their technological application. The mentioned authors published in the last years a number of works [4–7] devoted to optimization of the parameters of the process and technological application of light-beam heating.

The first unit for welding and brazing by radiant energy USPLE-1-MATI was designed in 1968 under the leadership of M.I. Oparin and then produced in Production Association «Elektromekhanika» (Rzhev, Russia). The unit consisted of arc xenon lamp of 3–10 kW power (produced at the Moscow electric lamp plant), which was used as a source of light of the ellipsoidal glass aluminized reflector, counter reflector and two-element quartz lens for additional focusing of the luminous radiation [2, 4, 5].

The Student Design Bureau created at the chair headed by M.I. Oparin dealt with the problems of designing technological tools, studying of power parameters of the light beam and carrying out experiments on welding and brazing of different structural materials. Special emphasis was made on development of different variants of technological units [4, 6, 8].

In 1970 the MATI researcher S.A. Fyodorov in cooperation with the «Elektromekhanika» developed an experimental unit USPLE-7-MATI with seven optic focusing systems and arc xenon lamps of 0.5 and 1 kW power for creation of complex heating charts and simulation of different heat processes. In 1976 a small-scale unit «Foton-1» for brazing of wiring joints was developed.

The performed studies showed that the light beam is a promising concentrated source of heat and has a number of advantages as compared to conventional ones: a possibility to heat materials irrespective of their electrical and magnetic properties; noncontact way of energy supply to the article directly or through optically transparent media and shells, which allows heating in the controlled gas medium and in vacuum; a possibility to achieve high values of energy density ($1 \cdot 10^3$–$1 \cdot 10^4$ W/cm^2) by relatively simple means (in electric arc and laser the same values achieve $1 \cdot 10^5$ and $1 \cdot 10^8$ W/cm^2, respectively) and heating spots of the required form and size; high controllability of the energy input into the article; cheapness of the equipment in comparison with laser; inconsiderable mechanical actions on the heated object; a possibility to mechanize and optimize the technological process by simple means. A radiation spectrum of the light beam (0.2–2.4 μm) is in the same range as ruby (λ = = 0.69 μm) and neodymium (λ = 1.06 μm) lasers. This radiation is more effective than infrared for heating of metals since its short-wave part of the spectrum is better absorbed by the metals. Light beam combines a locality nature of the laser heating with a possibility to carry out a group brazing like in infrared heating [4, 9].

Working parameters of the heat source (effective power, efficiency, heat input, heating temperature) depend on optical and thermal-physical properties of the heated materials, for example, absorption coefficient and item geometry [3]; absorption coefficient of the materials may vary with the temperature increase (e.g. it changes in heating of copper but does not change in heating of aluminium) [10] essentially affecting in the long run heat and power characteristics. Therefore, to control the process of heating with the light beam it is necessary to use all factors together providing the required character of temperature distribution in the article.

The accumulated results allowed in 1970–1980 switching from the development of laboratory variants

of the units to creation of commercial equipment specimens for solution of specific technological problems. Active participation of the MATI research workers contributed into the development of a series of production technological units (UPSL-1, USS-1, «Svet» and others) and initiation of the work on specialized short-focus glass aluminized reflectors and arc xenon lamps with small interelectrode gap allowing the efficiency of the used focusing optical systems to be increased. The developed procedures and means for alignment of optical systems, equipment for study and control of power parameters of the conditions, devices for determination of the absorbing ability of the materials, different technological tools, means for protection and monitoring of the object under treatment are developed. Technological peculiarities of the welding and brazing processes, technical regulations establishing rules for execution of technological forms and records are elaborated. The MATI welding chair became a leader in the development of light-beam technologies. The R&D results were reflected in the theses of M.I. Oparin (1971) and S.A. Fyodorov (1976) and generalized in the manual [4].

Eventually the MATI works in the sphere of light-beam technologies were further developed. Publications on brazing with high-temperature soldering iron with quartz halogen filament lamp, brazing of elements of radio electronic equipment on the mechanized units, submerged arc welding of aluminum alloys with radiant energy in vacuum and others were issued.

In the early 1980s the light-beam equipment developed towards increasing output power parameters of the light beam. The use of specialized metallic reflectors produced on the CNC machine tools and transfer to the pulse mode of power supply to the lamps permitted increasing density of the radiant flow up to 12 kW/cm^2.

Special focusing combined spherical-ellipsoidal optical systems for brazing and heat treatment, which allow transforming the radiant flow from normally distributed to the circular one and even into the flow split into two or more beams.

Computer programs for calculation of geometrical parameters of the reflectors for specific biological tasks were created. This allows implementing in practice a module principle in development of light-beam equipment. Modules of the radiant heating with xenon lamps of 0.12–10 kW power were used in different technological units. Designed works were accomplished in 1991 by producing together with the «Elektromekhanika» of a serial version of the multipurpose unit USTSL-1 with program control.

The theses of V.S. Mamaev (1985), N.S. Pronin, V.A. Frolov (1990), N.A. Korobko (1992) contain and systematize scientific results, clarify the areas of the most effective application of the light beam and classify technological processes of the light-beam heat treatment of the materials by three groups [3, 11, 12].

The first group includes the processes of welding of metallic plate body and shell-type structures 0.1–2.0 mm thick of carbon and alloyed steels, titanium, nickel and aluminium alloys and sealing of the bodies of electric vacuum tools in different controlled gas atmosphere, welding ceramics and plastics. The second group includes the processes of soldering of microelements on the printed circuit board, connectors, hookup wires with lugs in radio electronics and the processes of brazing of units of waveguide transmission lines, electric contacts of power electric equipment, winding of stators in electric engines. The third group covers the processes of local heat treatment of welded joints, heat dressing and hardening of articles.

Figure 1. Set of light-beam equipment for welding robotic complex

Technological aspects of light-beam welding and brazing of different materials are reflected in numerous publications [13–36]. They allow concluding that the focused light beam may weld thin-plate structures with the wall thickness 0.1–2.5 mm of low-carbon and high-alloyed steels, aluminium, nickel and titanium alloys [14, 16, 21, 22], thermoplastics and glassceramics and to reweld defects and seal the body parts. This list of problems may be solved, for example, by a set of light-beam equipment in the composition of robotic complex (Figure 1). So, in welding of titanium alloys VT5-1, OT4-2 and VT20 1.5–2.5 mm thick the power of the beam was 1.1–1.2 kW per 1 mm of the material thickness with welding speed 9–10 m/h. It is established that even with local shielding of the welding zone the light beam allows producing welds with higher strength and resistance to cyclic loads and decreased porosity of the weld metal as compared to the arc welding. In welding of low-carbon steels there is no need to apply additional shielding of the joint zone.

Wide ranges of regulation of power parameters (density of beam flow in the focal spot may vary from 0 to 2200 W/cm^2) as well as the shape and size of

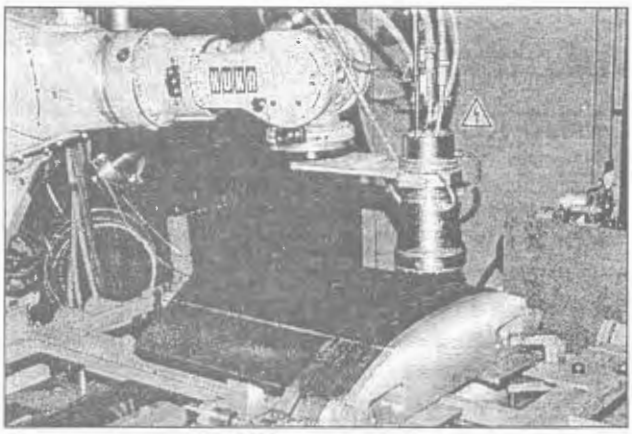

Figure 2. Light-beam equipment for welding and brazing

heat spot make it possible to apply light-beam heating in brazing [18, 20, 27, 35]. The process of such brazing is characterized by the following peculiarities: local heating of the sites for joints to be brazed with a wide temperature gradient, a possibility to apply practically any brazing filler metals starting from tin-lead solders to refractory filler alloys on the base of nickel and titanium [25, 27, 30, 32–34]; lowering of the probability of formation of brittle intermetallide interlayers in connection with a short period of heating. Ideal purity of the heating process in brazing in the controlled gas atmosphere and vacuum provides a high quality of joints.

The MATI light-beam equipment and technology were introduced at different enterprises in Russia: Radiopribor (Vladivostok), PPPO (Perm), KEMZ (Kovylkino), Volna, NITI (Saratov), the Lepse KEMPO (Vyatka), Teploobmennik and GAZ (N. Novgorod), RPKB (Ramenskoe, Moscow region), Zenit (Zelenograd, Moscow region), IOVNIIEM (Istra, Moscow region), Dzerzhinets, VNIIRT, Prozhektor and others.

In 1980s the MATI research workers V.S. Kudryavtsev (1984), V.F. Savichev (1988), V.B. Redchits (1989) and others along with introduction of the equipment and technology successfully defended their theses at the chair of the Institute. Technical solutions and technological developments proposed by the research workers of the chair were protected by more than 60 inventor's certificates while the results of the study were published in more than 120 scientific works [19–24, 27–32]. Doctor's thesis of V.A. Frolov (1998) generalizes the works in light-beam welding.

Development of the light-beam heating outside the territory of the former Soviet Union (Japan, FRG, USA and others) was initiated later for solution of specific technological problems. The studies performed abroad did not produce new scientific results even though they were based on the modern more advanced approach. M. Takagi and T. Yamaji (Japan) created a light-beam installation for soldering employed in electronics. This unit is based on radiation of the xenon lamp with a flexible optical cable, which naturally considerably expands technological possibilities of the process. It is successfully competes in the market with the laser heating units for similar purposes [37]. The Czech company SVAR spol s.r.o. with participation of a number of Russian organizations (NIIavtoprom, NPF, MGM and others) created a universal complex of light-beam equipment for welding and brazing (Figure 2) consisting of light-beam radiator, power source, service unit and a unit of autonomous water cooling. This complex may be, for example, used in the automobile industry.

CONCLUSIONS

1. Research workers of the MATI welding chair established advantages of heating with light beam as against other widespread methods of heating: a possibility of heat treatment of materials irrespective of their electrical and magnetic properties; probability of achieving high energy densities ($1 \cdot 10^3$–$1 \cdot 10^4$ W/cm^2) by relatively simple means; noncontact way of energy supply to the article directly and through optical transparent shells in any controlled gas atmosphere and in vacuum; inconsiderable mechanical action of the object being heated; high regulation ability and controllability of the heat input. Such combination of the properties of optical heat source opens wide perspectives for its application for welding and brazing.

2. Focused beam of arc xenon lamps may be used for welding of thin-walled structures (thickness is 0.1–2.5 mm) of low-carbon and high-alloyed steels (for example 08Yu, St10, 12Kh18N10T, 30KhGSA, high-manganese steels of Fe–Mn–Al–C system with 30 % Mn) as well as alluminium (AMg3), nickel and titanium alloys (OT4, VT5-1, VT20, OT4-2), thermoplastics and glassceramics. In this case welding of low-active materials (low-carbon steels, copper alloys) is carried out directly in the air, which simplifies the technological process.

3. Brazing of metals with light beam of arc xenon lamps may be carried out by moving and immovable heat sources; there is an intensive heat activation of the surface in the heating spot, which creates favorable conditions for wettability and spread of the brazing filler metal. Discovery of new possibilities of the light beam of the arc xenon lamps in welding technologies is very promising.

4. Depending on the specific technological tasks it is possible to use both solders and refractory brazing filler alloys. Light-beam brazing is applicable in vacuum, in the atmosphere of shielding gases and in the air using the relevant fluxes.

1. Belyanchikov, L.N. (2004) Light-beam technologies as a prospective developing trend of special electrometallurgy. *Elektrometallurgiya*, **10**, 21–26; **11**, 24–29.
2. Nikiforov, G.D., Dyachenko, V.V., Oparin, M.I. et al. (1969) Application of focused light energy of high-power xenon lamps for welding and brazing of metals. *Svarochn. Proizvodstvo*, **9**, 1–3.
3. Nikiforov, G.D., Oparin, M.I., Fyodorov, S.A. (1974) Application of light heating for welding, brazing and heat treatment. *Ibid.*, **12**, 19–21.

4. Nikiforov, G.D., Oparin, M.I., Fyodorov, S.A. (1979) *Light-beam welding and brazing*. Moscow: Mashinostroenie.
5. Fyodorov, S.A., Ovchinnikov, V.V. (1983) Weld formation control in light-beam welding. *Svarochn. Proizvodstvo*, **9**, 33–35.
6. Oparin, M.I., Nikiforov, G.D., Mamaev, V.S. (1982) Extension of power capacities of machines for light-beam welding in pulse supply of arc xenon lamps. *Ibid.*, **7**, 13–14.
7. Oparin, M.I., Frolov, V.A., Pronin, N.S. (1989) New in field of light-beam welding by arc xenon lamps. In: *Increase of quality and efficiency of welding production in Moscow enterprises*. Moscow: MDNTP.
8. Frolov, V.A. (1998) Engineering and design specifics of development of welded structures using the light-beam welding. *Svarochn. Proizvodstvo*, **3**, 16–20.
9. Frolov, V.A., Mamaev, V.S., Pronin, N.S. et al. (1993) Application of light-beam energy for technological purposes. *Ibid.*, **4**, 12–14.
10. (1974) *Technology of fusion electric welding of metals and alloys*. Ed. by B.E. Paton. Moscow: Mashinostroenie.
11. Frolov, V.A., Pronin, N.S., Fyodorov, S.A. et al. (2003) Design and development of light-beam welding, brazing and heat treatment technologies. *Svarochn. Proizvodstvo*, **11**, 19–21.
12. Frolov, V.A., Pronin, N.S., Fyodorov, S.A. et al. (2003) Design and development of light-beam welding, brazing and heat treatment technologies. *Tekhnologiya Mashinostroeniya*, **5**, 28–29.
13. Fyodorov, S.A., Ovchinnikov, V.V. (1993) Local heat treatment of aluminium alloy welded joints by light-beam heat sources. *Ibid.*, **1**, 6–7.
14. Ovchinnikov, V.V., Fyodorov, S.A. (1989) Mechanical properties of sheet titanium alloy welded joints made by arc and light-beam welding. *Ibid.*, **8**, 14–15.
15. Fyodorov, S.A., Ovchinnikov, V.V. (1986) Influence of difference in metal pool surface tension on formation of weld during light-beam welding of sheet materials. *Ibid.*, **11**, 33–35.
16. Frolov, V.A., Mamaev, V.S., Pronin, N.S. et al. (1993) Light-beam welding of sheet titanium alloys. *Ibid.*, **1**, 4–6.
17. Frolov, V.A., Mamaev, V.S., Redchits, V.V. et al. (1993) Improvement of operational reliability in light-beam welding. In: *Abstr. of Sci.-Techn. Conf. of the CIS Countries on Production and Reliability of Welded Joints* (Kaliningrad, Jan. 26–28, 1993). Moscow.
18. Frolov, V.A., Mamaev, V.S., Pronin, N.S. et al. (1993) Application of light beam in motor car construction. *Ibid.*
19. Nikiforov, G.D., Pronin, N.S., Fyodorov, S.A. (1973) Peculiarities of formation of pool without backing in light-beam welding of sheet materials. *Svarochn. Proizvodstvo*, **8**, 1–3.
20. Nikiforov, G.D., Oparin, N.S., Fyodorov, S.A. (1978) Energy and operational specifics of light-beam welding and brazing of metals. In: *Increase of quality and efficiency of welding production*. Moscow: MDNTP.
21. Fyodorov, S.A., Ovchinnikov, V.V. (1984) Peculiarities of corrosion-resistant steel welded joints made by light beam in nitrogen-oxygen mixtures. *Svarochn. Proizvodstvo*, **8**, 23–24.
22. Oparin, M.I., Frolov, V.A., Svobodov, A.N. et al. (1990) Light-beam welding of high-manganese steels. *Ibid.*, **8**, 2–3.
23. Ovchinnikov, V.V., Fyodorov, S.A. (1990) Light-beam welding by arc xenon lamps of joints of stud–flange type. *Ibid.*, **5**, 23–24.
24. Nikiforov, G.D., Fyodorov, S.A., Ovchinnikov, V.V. (1982) Shielded-nitrogen light-beam welding of low-carbon and corrosion-resistant steels. *Ibid.*, **10**, 9–11.
25. Ovchinnikov, V.V., Fyodorov, S.A. (1989) Sealing of products by arc xenon lamp light beam. *Ibid.*, **2**, 3–4.
26. Oparin, M.I., Mamaev, V.S., Frolov, V.A. et al. (1991) Operational specifics of light-beam welding of copper electrical installation wires. *Ibid.*, **6**, 3–4.
27. Zernov, I.A., Belov, L.A., Bulbutenko, V.S. (1986) Selection of parameters of radiation local brazing of tubular heat exchangers. In: *Transact. on Progressive Methods in Brazing*. Kiev: PWI.
28. Ovchinnikov, V.V., Fyodorov, S.A. (1991) Light-beam brazing by arc xenon lamps of capillary tubes with reinforcement. *Svarochn. Proizvodstvo*, **4**, 4.
29. Fyodorov, S.A., Grinin, V.V., Ovchinnikov, V.V. et al. (1986) Light-beam brazing by arc xenon lamps of spring contacts. *Ibid.*, **3**, 2–3.
30. Ovchinnikov, V.V., Fyodorov, S.A. (1991) Light-beam brazing by arc xenon lamps of filter elements. *Ibid.*, **11**, 28–29.
31. Oparin, M.I., Korobko, N.A., Pronin, N.S. (1991) Light energy brazing of integrated circuits on cards. In: *New energy and material saving technologies of brazing in national economy*. Smolensk.
32. Mironov, L.G., Ravaev, G.P., Petukhov, V.F. (1981) Experience of application of focused light energy of arc xenon lamps in brazing of products. In: *Transact. on New Developments in Field of Brazing*. Kiev: PWI.
33. Oparin, M.I., Mamaev, V.S., Pronin, N.S. et al. (1988) Peculiarities of heating by light beam of arc xenon lamps in brazing of assemblies of copper and its alloys. In: *Technological thermophysics*. Sect. 3: Thermophysics of welding and brazing processes. Toliatti.
34. Oparin, M.I., Korobko, N.A., Pronin, N.S. et al. (1991) Application of energy of space-transformed light beam for brazing. In: *New energy and material saving technologies of brazing in national economy*. Smolensk.
35. Alekseev, G.M., Butov, V.N. (1999) Equipment for light-beam welding and brazing of thin-walled structures. *Svarochn. Proizvodstvo*, **9**, 33–35.
36. Pigarev, K.V., Volkov, S.S. (2000) Study of energy parameters of light-beam small-sized emitter without lamps. *Ibid.*, **3**, 54–56.
37. Takagi, M., Yamaji, T. (1995) New soldering process using light beam technology. *Soldering and Surface Mount Technology*, **20**, 13–18.

APPLICATION OF COMBINED ELECTROMAGNETIC ACTIONS FOR IMPROVING THE QUALITY OF WELDS IN WELDING WITH NON-CONSUMABLE ELECTRODE

R.N. RYZHOV
National Technical University of Ukraine «Kiev Polytechnic Institute», Kiev, Ukraine

Experiments were the basis to conduct comparative analysis of the effectiveness of application of an electromagnetic impact with a pulsed axial and combined magnetic field to control the parameters of weld formation and solidification.

Keywords: *arc welding, non-consumable electrode, electromagnetic action, magnetic field, combined electromagnetic action, weld formation, macrostructure*

Efficiency of welding technologies with external pulse actions is to a great extent determined by a comprehensive improvement of the weld quality indices. In welding with electromagnetic actions (EMA) in the case of applying axial controlling magnetic field (CMF) it is possible to control hydrodynamics of the weld pool with the aim of both degassing and considerable improvement of the parameters of the weld crystallization [1]. However, transformation of the arc geometry into a cone-like shape accompanied by the arc dissipation as the heating source, which is typical for such action results in 20–30 % decrease of the penetration depth. Decrease of the penetration depth in non-consumable electrode welding characterized with a tough regulation of the parameters of the welding process is unacceptable.

One of the ways to preserve the set penetration depth in welding with EMA is the use of reverse pulsating magnetic fields with regulation of time intervals between CMF pulses during which the arcing is in the natural state [2]. However, in this case to preserve EMA efficiency for solidification of the weld pool it is necessary to increase both CMF in the pulse, which requires increasing of mass and size parameters of electric magnets and can decrease arcing stability, and duration of the CMF reverse interval, which may be accompanied by a deterioration of the weld formation parameters.

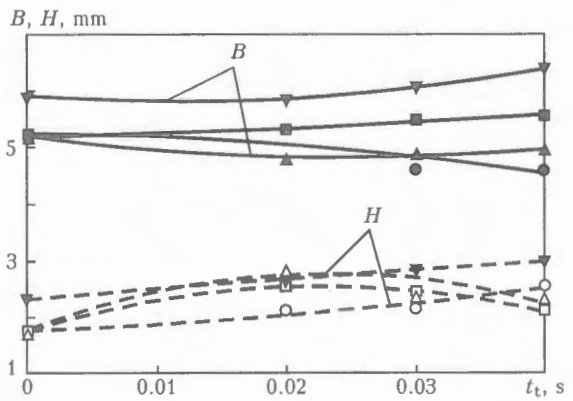

Figure 1. Dependence of width B (*solid curves*) and depth H (*dashed*) of the welds on time of the action of transverse CMF in welding with combined EMA (I_w = 100 A, v_w = 10 m/h): ● and ○ – pulsating axial CMF; ■, □ and ▲, △ – combined EMA under force action for time t_t directed downward and upward, respectively; ▼ – the same at I_w = 130 A, v_w = 13 m/h

Another way to solve the problem is to apply the transverse CMF creating volume electrodynamic forces in the direction perpendicular to the pool surface. Such EMA allow both decrease and increase the penetration depth relative to the initial one [3].

Proceeding from the fact that the use of axial CMF is more appropriate for control of the crystallization parameters while transverse CMF – for control of the weld formation parameters the aim of this work is to determine the efficiency of using the combined EMA for a comprehensive improvement of the parameters of the weld joint quality.

Plates of stainless steel 12Kh18N10T 6 mm thick were penetrated in the course of the experiments under the following conditions: I_w = 100 A, U_a = 10 V, v_w = = 10 m/h as in the work [3]. Axial and transverse CMF in the welding zone were generated by a special torch with a six-pole electromagnetic system [4] by superposition of magnetic fields of its separate electromagnets [3]. Amplitudes and durations of the pulse sequences of currents through the coils of electromagnetic system were preset by means of microprocessor device of the EMA control [5].

Combined EMA was created by an alternating generation of axial (during time t_a) and transverse (during time t_t) CMF in the welding zone. The period of t_c = = $t_a + t_t$ action was changed within the range of 0.05–0.10 s by regulation of t_t within 0–0.05 s with unchanged t_a = 0.05 s optimal for the given experimental conditions [3]. The next period differed from the previous one only by the polarity of the axial CMF, which allowed achieving reverse moving of the melt along the side surfaces of the pool. Induction of both implemented CMF types was equal to 15 mT proceeding from the achieved in [3] maximal changes in the parameters of the weld formation under EMA with a separate use of axial and transverse magnetic fields. Combined EMA with force downward and upward actions on the melt were separately studied in the

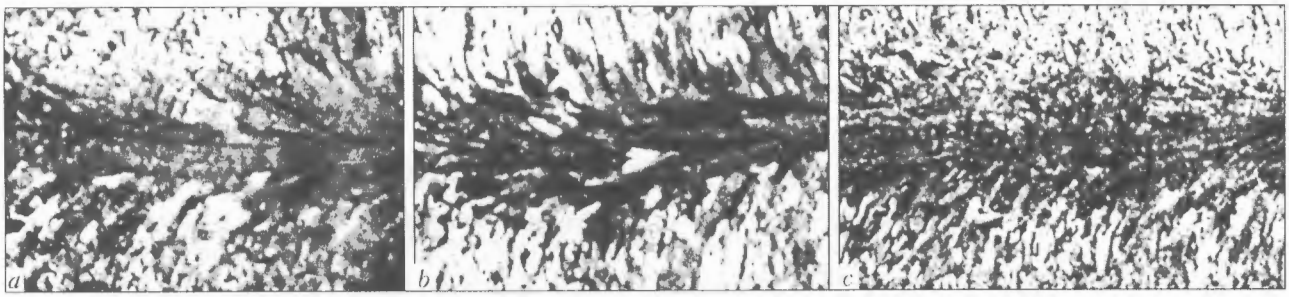

Figure 2. Macrostructures of welds under pulsating axial CMF (*a*) and combined EMA under force action for time t_t directed downward (*b*) and upward (*c*)

experiment. In implementing EMA with pulsating axial magnetic fields [2] induction of both types of the used CMF was equal to zero during t_t.

It is experimentally established (Figure 1) that the use of combined EMA irrespective of the polarity of transverse CMF and, thus, a direction (upward or downward) of the force action on the melt allows increasing the penetration depth H by 60–65 % at t_t = = 0.02–0.03 s. This action may be explained by press back the melt from the arc, which results in an increase of its penetration ability. The further growth of t_t is accompanied by some decrease of H. It is explained by the fact that after the melt achieves the tail area of the pool its reverse jet directed to the center is formed. For confirmation of this action the experiments were carried out when I_w and v_w were increased by 30 %, which with unchanged value of the heat input allowed increasing the length of the tail part of the pool. In these conditions the H decrease was not observed even at t_t = 0.04 s (see Figure 1). In implementation of EMA with pulsating axial CMF the t_t increase is accompanied with monotonous H growth, which, however, is not so significant as at the combined EMA.

In welding with combined EME increase of the weld width was observed only when force action at t_t was directed vertically downward (see Figure 1). When direction of the force action is changed for the opposite the parameter B decreases with increase of t_t. Similar results were obtained in welding with pulsating axial CMF.

These experimental dependences may be explained as follows. At the beginning of the t_t period when axial CMF during the time t_a has already formed the melt flow moving along one of the side edges of the pool, the force action in the vertical direction is created. In case it is directed downward the flow of the melt repulsed from the bottom moves toward the tail area of the pool already along two side edges, thus decreasing a thickness of the melted interlayer under the arc, which resulted in the increased penetration depth. Simultaneously with this and similar to the action of the axial CMF movement of flows along side edges of the pool causes their «wash-out», which leads to an increase of the weld width. In case when for the time t_t the force action is directed upward the melt press back from the arc does not move along side edges of the pool but creates near the melting front an excessive volume, which during the next period t_a is transferred to the tail area. In this case the width of the welds decreases similar to the action of the pulsating axial CMF when with increase of t_t this parameter of formation approaches the initial values.

Difference of the hydrodynamics of the processes in the pool with EMA manifests itself in the macrostructures of the welds. At EMA with pulsating axial CMF at t_t = 0.02–0.04 s one observed the structures of the welds inconsiderably differing from the initial (Figure 2, *a*). Combined EMA under which for time t_t the force action is directed downward is characterized with constant, not pulse movement of the overheated melt from the head to the tail part of the pool. This leads to a decrease of the cooling rate of the central part of the weld. As a result a coarse transcrystallite structure forms at $t_t > 0.03$ s (Figure 2, *b*). The finest grain structure was observed at combined EMA under which at t_t the force action is directed upward (Figure 2, *c*). It is noteworthy that in the process of revealing a structure the microsections produced of the specimens of the given series were poorly etched, which testifies to a decrease of a level of chemical microheterogeneity. This action is characterized by the fact that the volumes of the melt increased as against conventional EMA are transferred by impulses for the time t_a towards the tail part of the pool. In all probability this is accompanied not only by periodical stops with preset frequency of the solidification front but also by partial fusion of already formed crystallites, which is explained by a considerable refining of the microstructure.

CONCLUSIONS

1. In welding with combined EMA maximal simultaneous improvement of the parameters of formation and solidification of the welds is achieved in the case when at $t_t \geq 0.02$ s the force action on the melt of the pool created by transverse CMF directed upward.

2. Application of the combined EMA allows completely compensating a decrease of the penetration depth without decrease of the efficiency of the action on the solidification processes, typical for welding with electromagnetic stirring.

1. Chernysh, V.P., Kuznetsov, V.D., Briskman, A.N. et al. (1983) *Electromagnetic stirring welding*. Kiev: Tekhnika.
2. Malinkin, I.V., Popovsky, V.Yu., Syrovatka, V.V. et al. (1971) Preservation of penetration depth in electromagnetic stirring of weld pool. *Avtomatich. Svarka*, **8**, 46–48.
3. Ryzhov, R.N., Kuznetsov, V.D., Malyshev, A.V. (2004) Application of six-pole electromagnetic system for control of weld formation parameters in non-consumable electrode welding. *The Paton Welding J.*, **2**, 41–44.
4. Ryzhov, R.M., Malyshev, O.V. *Welding torch with external electromagnetic actions*. Pat. 42252A Ukraine. Int. Cl. B 23 K 9/08. Publ. 15.10.2001.
5. Titov, A.A., Malyshev, O.V., Ryzhov, R.M. *Non-consumable electrode welding method using the external combined control magnetic fields and device for its realization*. Pat. 50430 Ukraine. Int. Cl. B 23 K 9/08. Publ. 15.10.2002.

IMPROVEMENT OF THE TECHNOLOGY OF HEAT TREATMENT OF COATED WELDING ELECTRODES

M.F. GNATENKO
OJSC «VELMA», Kiev, Ukraine

The paper deals with the equipment and technology development trends for optimizing the heat treatment of quality electrodes aimed at improvement of drying properties of the coating.

Keywords: *welding consumables, coated electrodes, drying properties of the coating, directions of improvement*

Electrode heat treatment is an energy-consuming process (more than 80 % of the overall volume of energy consumption). This is the final and very «tricky» production stage. An incorrect heat treatment mode can significantly influence the quality of electrodes, swelling, cracking and deterioration of the coating quality.

Proceeding from the features of electrode heat treatment technology, the methods for its improvement can be divided into two interrelated groups.

The first equipment group includes: selection of furnace design, kind of heating, method and means of heat application, i.e. all that is related to the heat carrier, moisture removal, control of the heat treatment processes, etc.

The second technological group is related to electrode coating properties, namely its drying properties, degree of moisture cohesiveness, coating structure resistance to moisture removal, nature of variation of the ductile-mechanical properties of the coating at heating, thermal-shrinkage properties, etc.

As regards the equipment with which the furnaces are fitted, there are two types of electrode productions, namely highly efficient conveyor and small-sized small-batch productions, including those manufacturing special electrodes.

For enterprises with a small (up to 10 tons per shift) production volume chamber furnaces with electric (heater, heating element) or gas heating should be regarded as optimum. In these furnaces the electrodes are laid on frames or beds (at less than 2 % humidity), and heat treatment is performed after their dry-curing. It is necessary to ensure an intensive blowing of each electrode by the heat-carrier (best of all along its length) for a fast and uniform heating and removal of moisture from the electrode coating. In this case it is very important to completely eliminate the idle flows of the heat carrier. Furnace design should envisage airways of an adjustable cross-section for fresh air supply and removal of moist air.

Heating rate is mainly determined just by the initial moisture in the electrode coating, i.e. after dry-curing. At the humidity below 4 % the rate of electrode heating practically does not have any limits, as its coating is already quite strong and heat setting processes are mostly over, so that swelling and cracking are eliminated.

Maximum temperature and time of soaking should be matched so as to achieve the required degree of dehydration of the electrode coating at maximum temperature. This minimizes the coating softening and reduces energy consumption. Technological properties of the electrode coating have a significant role here.

Electrode cooling stage is very important. Abrupt cooling due to a difference in the coefficients of linear expansion of the rod and electrode coating after heat treatment may lead to cracking. Therefore, at the temperature of 100–120 °C the electrode cooling rate should be low and uniform along its length. If cooling is performed in the furnace, the productivity of the latter is markedly reduced. It is rational to move the electrodes out of the furnace under a thermo-cap, where the cooling rate is low, while the furnace is still used for its purpose. The heat from the thermo-cap can be used for dry-cure.

For the case of conveyor production, analysis of the electrode heat treatment process demonstrated that the following most promising types can be selected from the available conveyor-type furnaces:

- gas conveyor furnace (design of «Teploproekt» Institute) which is not simple in design, but efficient in terms of heat treatment rate, low-inertia, of a small weight. It should be improved to provide air regeneration for electrode cooling at the furnace outlet. Gas combustion chambers should be also simplified;
- conveyor furnace of OKB type with radiation heating (VNIIETO design). It has a more complex structure, but is very readily mechanized, and is highly efficient. The electrodes are subjected to uniform heat treatment; load-carrying elements are heated once — at the stage of furnace heating. Small heat losses occur on the reloading device and they should be minimized. Transportation of as-molded electrodes in the first passage, as well as design of electrode reloading de-

vices between passages should be optimized. In the upper two passages heating elements are not required, just moisture withdrawal is needed. The baking stage should envisage the mechanism of electrode turning;

• tunnel furnace with electric or gas heating (two tunnels — for dry-cure and heat treatment). It provides the capability of laying the electrodes on frames and frame stacking. In terms of design it is difficult to mechanize electrode loading on the frames, or their unloading in it. Its load-carrying elements have a large mass. Effectiveness of the heat treatment process is increased, when shields and heat carrier regeneration are used.

Of the three considered furnace models, the most promising one is the gas furnace design of «Teploproekt» Institute.

Based on the conducted analysis of operation of various furnace types and results of their industrial testing, we have designed a simple cost-effective reliable furnace for application both in the conveyor and in small-sized productions. This is a gas (alternatively electric) conveyor furnace, having load-carrying elements of a small weight, a simple design, with mechanized loading and unloading of electrodes. In 1 to 1.5 years the furnace will be embodied in the metal.

As regards the technological group of developments concerning improvement of drying properties of welding electrode coating, three methods to improve the drying properties of electrode coatings by optimizing the following elements should be considered:

• granulometric composition of the components (increase of grain packing density and decrease of shrinkage, cracking, and coating swelling; lowering of the component surface activity and suppression of their interaction with liquid glass; coating reinforcement or making a frame);

• composition and characteristics of liquid glass (selection of viscosity (density), module, and type, which determine the structure and properties of liquid glass film and energy of moisture cohesion with the material; decrease of liquid glass activity relative to the charge components and swelling suppression);

• kind and content of practicizer (providing the required degree of mass structuring; slowing down of the process of mass softening in heating; active impact on liquid glass for conversion of as much as possible of chemically bound moisture into free moisture).

In each of the above improvement areas we have developed specific directions of improving the drying properties of electrode coating. They enable increasing the rate of moisture removal from the coating and lowering the temperature of electrode baking, thus eliminating the dents, sticking, swelling, cracks in the coating, and providing the required degree of its dehydration.

Combination of optimum furnace design and heat treatment modes will provide a high quality of the latter at minimum production costs.

RECONDITIONING ARC HARD-FACIN GOF WORN OUT TRAM RAILS

Technology and flux-cored wires of the austenitic (PP-AN202) and ferritic (PP-AN203) grades were developed for reconditioning hard-facing of tram rails made from steels M-75 and M-76 containing up to 0.82 % carbon. The technology requires no preheating or dismantling of rails from the track.

Hard-facing is performed by depositing horizontal beads. The quantity of the beads (from 5 to 15) depends upon the extent of wear. The first beads are deposited with self-shielding flux-cored ferritic wire PP-AN203, and the subsequent beads E with flux-cored wire PP-AN202 by the submerged arc method using flux AN-26P. This provides good bead formation, excellent detachability of the slag crust and absence of cracks and pores.

Deposited metal of all the layers (except for the first one) has tough austenitic structure with hardness *HRC* 22–25. Cold working increases its hardness to *HRC* 50–52, thus resulting in a substantial increase in wear resistance of the rails treated.

To realise this technology, the Research Centre DUGA-2 of the E.O. Paton Electric Welding Institute designed and manufactured hard-facing device UD-654. It has the form of a self-propelled carriage moving over the rails to be treated at a working and travel speed. Actuating mechanisms, control panel, as well as a reserve amount of wire and flux are located on the carriage. The welding circuit is powered from diesel generator. Not to prevent tram traffic, hard-facing should be performed during the night time in dry weather at a temperature not below +10 °C. The costs of reconditioning hard-facing are approximately 3 times lower than those of replacement of worn out rails by the new ones.

Application. Hard-facing of worn out rails without dismantling them from the track.

Proposals for co-operation. Application of the technology and equipment for hard-facing of tram rails at a customer's.

Contacts: Dr. Ryabtsev I.A.
Tel./fax: (38044) 287 63 57; E-mail: ryabtsev@paton.kiev.ua

THESIS FOR A DOCTOR'S DEGREE

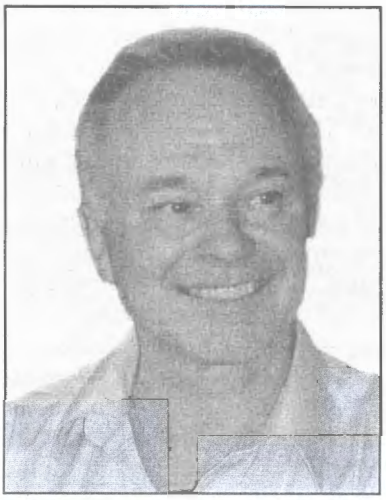

E.O. Paton Electric Welding Institute, NASU, Kiev, Ukraine

Yu.M. Kuskov (PWI) defended on the 18th of May 2005 his thesis for a Doctor of Technical Sciences degree on subject «Electroslag Process and Technology for Cladding in Current-Conducting Mould Using Discrete Consumables».

The thesis is dedicated to introduction of a fundamentally new direction in the field of electroslag cladding of cylindrical parts, forming rolls in particular, based on the modern concepts of production of high-quality metal, which is provided by a purposeful control of thermal-physical and solidification processes. This control can be achieved, for example, owing to treatment of the deposited metal with highly reactive refining slags, inoculating effect on the solidifying metal melt by a discrete filler in the form of grit, electromagnetic effect on the process of phase transition of metal from a liquid to solid state, and creation of conditions for accelerated cooling of the formed metal pool.

The most significant results obtained by the author of the thesis are as follows.

• Conditions for a stable occurrence of the electroslag process in a current-conducting mould was studied. The electroslag cladding process was found to take place in two stages. At the initial stage, it is necessary to apply the alternating or direct current of straight polarity by feeding a not less than 45–55 V voltage to the slag pool. The second stage is characterised by the established process with an operating voltage that constitutes 50–70 % of the initial one. The total current grows with decrease in the ratio of diameters of the current-conducting and forming mould sections to thickness of the deposited layer. Stability of the process and quality of the deposition are provided by distributing the electric current to the metal pool that is not less than 25 % of that fed to a billet.

• Kinetics of transfer of a discrete filler to the layer of a rotating slag and character of formation of the deposited layer were investigated. As established, the rate of transfer of particles through the slag is 5–10 times lower than the calculated one, which is caused by freezing of the slag onto the particle surfaces. This excludes formation of defects in the deposited metal. As the speed of rotation of the slag pool is increased to more than 150 rpm, the process of transfer of the particles changes, and the time of their dwelling in the slag increases. This leads to broadening of grain composition of a filler used for cladding.

• It was established that wear-resistance of deposited chromium cast iron could be increased by a factor of 1.2–1.3 through increasing grain composition of the particles from 1.6–2.5 to 2.5–3.5 mm, and by 40–50 % with an almost 3 times increase in mass content of the filler fed to the slag pool. This is caused by a change in structure of the cast iron, and a more than 2 times decrease in size of chromium carbide in particular. Compared with cladding using a non-compact filler, grain size of the deposited metal of the type of high-speed steel R6M5 is decreased approximately 3 times.

• New design of a water-cooled non-consumable electrode, having the form of a sectional current-conducting mould, was developed. This makes it possible to exclude a rigid relationship between the rate of feeding of a material to be remelted, and shape and size of the metal pool. As established, the electrode should consist of three sections. Diameter of the current-conducting section should be 5–30 % larger than diameters of the other sections, as this provides a 30 % decrease in heat loads on its walls, and approximately 1.4 times extension in service life. The intermediate and forming sections require no special protection of their working surfaces from electric erosion. To fully eliminate the electric erosion phenomena, the intermediate section should be made from refractory non-conducting materials of the type of boron carbonitride.

Results of theoretical and experimental studies of the electroslag process by feeding a discrete filler to the slag pool and using a new design of the device to implement the process were used as a basis for the development of a new high-productivity technological method for reconditioning and hardening of forming rolls. The efficiency of application of the method was verified in electroslag cladding of rolls intended for different mills with a barrel diameter of 400 to 1000 mm, which was implemented using installations OB1960, OB2217 and EShP-10VG.

ADVANCE BOOK INFORMATION

FORTHCOMING BOOK INFORMATION

Vladimir I. Makhnenko, Viktor E. Pochynok. STRENGTH CALCULATION OF WELDED JOINTS WITH CRACK-LIKE IMPERFECTIONS.
Approx. 300 pp., 165×235 mm, hardback. November 2005. US$ 90

In this manuscript, the idea of the fitness-for-purpose concept is used to improve strength calculations of welded joints with crack-like imperfections caused by structural or technological factors. These include welded joints with fillet, spot, slot and butt welds having sharp fissures brought by geometry of the elements welded and limited sizes of the weld sections. Such joints are widely encountered in modern general-purpose welded structures used in civil building, shipbuilding, automobile industries, etc.

The welded joints just mentioned do not usually cause problems for structures of relatively ductile materials with small-to-medium thicknesses of component sections, and operating under predominantly static loading. However, the use of new structural materials, especially high-strength steels and aluminum alloys, etc., large cross sections of structural elements, and loading with alternate loads, requires a certain caution to be taken. Nonetheless, the technological advantages that these joints produce attract an interest in their use, of course, when it does not cause any harm to the structure safety and its residual service life.

Performing strength calculations based on the fitness-for-purpose criterion for the joints encountered in general-purpose structures, allows ensuring the requirements concerning the service life-time. However, there is a difficulty of implementing such calculations in wide engineering practice. As shown by the authors, a successful implementation of the mentioned concept for general-purpose welded joints and for wide range of users is possible only when it is based on the use of corresponding computer systems with friendly user interface, which do not require a user to have a special knowledge in fracture mechanics, deformation mechanics, numerical methods, etc. Such systems are to be portable and efficient, i.e. calculations of appropriate section sizes or verification of strength of specific joints should be done promptly. In turn, it requires development of numerical procedures and creation of specialized databases that simplify and accelerate calculations.

Viktor Ya. Kononenko. TECHNOLOGIES OF UNDERWATER WET WELDING AND CUTTING.
Approx. 140 pp., 140×200 mm, softback. December 2005. US$ 40

The book deals with the features of arcing, metal transfer and joint formation in consumable-electrode wet underwater welding. Principles of development of coated electrodes and self-shielded flux-cored wires for underwater welding and cutting are established. Characteristics of welding consumables and mechanical properties of weld metal are given. Some types of joints, procedure of preparation and fit-up for welding, possible defects of the joints and methods to prevent their formation are described.

Information on characteristic damage to the underwater metal structures is generalized, and technological solutions are given, which have been implemented during restoration of their performance, using wet processes of underwater welding and cutting. The book gives the characteristics of the equipment for implementation of underwater arc welding process.

The main processes of thermal underwater cutting are presented, and characteristics of consumable materials and equipment for its implementation are described. Examples of work performance using underwater cutting are given.

The book is designed for scientific and engineering-technical personnel, qualified welders-divers involved in design, fabrication and repair of underwater constructions.

The book is written by a specialist, who is developing electrode materials and technologies and has a vast experience of practical work under the water.

ADVANCE BOOK INFORMATION

TITANIUM: Titanium and its alloys. Technologies. Equipment. Production. Electrometallurgy. Welding

Approx. 180 pp., 200×290 mm, softback. December 2005. US$ 50

The collection presents papers on electrometallurgy and welding of titanium and its alloys published between 2002 and 2005 in «Advances in Electrometallurgy» and «The Paton Welding Journal» journals. The authors of the papers are scientists and specialists in the field of titanium and its production, known in Ukraine and abroad. The collection is designed for a broad range of readers dealing with the problems of production, processing and use of titanium.

ORDER RORM

Please return to:

International Association «Welding»,
11, Bozhenko str., Kiev, 03680, Ukraine
Tel.: (38044) 287 6757, 287 6049, 529 2623
Fax: (38044) 287 4677
E-mail: journal@paton.kiev.ua; tomik@mac.relc.com

Please send me:

❑ Vladimir I. Makhnenko, Viktor E. Pochynok «Strength Calculation of Welded Joints with Crack-Like Imperfections». US$ 90, postage included

❑ Viktor Ya. Kononenko «Technologies of Underwater Wet Welding and Cutting». US$ 40, postage included

❑ «Titanium». Collection of Scientific Paper. US$ 50, postage included

How to Pay and Payment Details

❑ By bank transfer (or mail a cheque) into our account
№ 2600801283433
UKREXIMBANK, Kiev, Ukraine
S.W.I.F.T.: EXBSUAUX
CORR. ACC. #04-094-227
Bankers Trust Company,
New York, U.S.A.
S.W.I.F.T.: BKTR US 33

❑ Please Invoice

❑ Your Details
Name _____

Organization _____

Address _____

Signed _____ Date _____